MICROCOPY RESOLUTION TEST CHART

NATIONAL BUREAU OF STANDARDS-1963-A

ARO 23223.26EL

②

PHASE-LOCKED SEMICONDUCTOR QUANTUM
WELL LASER ARRAYS

Elias Towe

Technical Report 526

March 1987

Massachusetts Institute of Technology
Research Laboratory of Electronics
Cambridge, Massachusetts 02139

DTIC
ELECTE
S
SEP 2 8 1987
D
E

87 9 9 245

AD-A185 155

REPORT DOCUMENTATION PAGE

1a. REPORT SECURITY CLASSIFICATION	1b. RESTRICTIVE MARKINGS
Unclassified	

2a. SECURITY CLASSIFICATION AUTHORITY	3. DISTRIBUTION/AVAILABILITY OF REPORT
	Approved for public release; distribution unlimited
2b. DECLASSIFICATION/DOWNGRADING SCHEDULE	

4. PERFORMING ORGANIZATION REPORT NUMBER(S)	5. MONITORING ORGANIZATION REPORT NUMBER(S)
	ARO 23223.26-EL

6a. NAME OF PERFORMING ORGANIZATION	6b. OFFICE SYMBOL (If applicable)	7a. NAME OF MONITORING ORGANIZATION
Research Laboratory of Electronics Massachusetts Institute of Technology		

6c. ADDRESS (City, State and ZIP Code)	7b. ADDRESS (City, State and ZIP Code)
77 Massachusetts Avenue Cambridge, MA 02139	

8a. NAME OF FUNDING/SPONSORING ORGANIZATION	8b. OFFICE SYMBOL (If applicable)	9. PROCUREMENT INSTRUMENT IDENTIFICATION NUMBER
U.S. Army Research Center		DAAL 03-86-K-0002

8c. ADDRESS (City, State and ZIP Code)	10. SOURCE OF FUNDING NOS.			
	PROGRAM ELEMENT NO.	PROJECT NO.	TASK NO.	WORK UNIT NO.
P. O. Box 12211 Research Triangle Park North Carolina 27709		P-23223-EL		

11. TITLE (Include Security Classification) Phase-Locked Semiconductor Quantum Well Laser Arrays

12. PERSONAL AUTHOR(S) Elias Towe

13a. TYPE OF REPORT	13b. TIME COVERED	14. DATE OF REPORT (Yr., Mo., Day)	15. PAGE COUNT
Technical Report 526	FROM _____ TO _____	March 1987	191

16. SUPPLEMENTARY NOTATION
This report is based on the PhD Thesis of the author.

17.	COSATI CODES		18. SUBJECT TERMS (Continue on reverse if necessary and identify by block number)
FIELD	GROUP	SUB. GR.	

19. ABSTRACT (Continue on reverse if necessary and identify by block number)
see next page

20. DISTRIBUTION/AVAILABILITY OF ABSTRACT	21. ABSTRACT SECURITY CLASSIFICATION
UNCLASSIFIED/UNLIMITED ☒ SAME AS RPT. ☐ OTIC USERS ☐	Unclassified

22a. NAME OF RESPONSIBLE INDIVIDUAL	22b. TELEPHONE NUMBER (Include Area Code)	22c. OFFICE SYMBOL
Kyra M. Hall RLE Contract Reports	(617) 253-2569	

DD FORM 1473, 83 APR   EDITION OF 1 JAN 73 IS OBSOLETE.

19. ABSTRACT

This dissertation presents the experimental study of quantum well heterostructures in the III-V compound semiconductor system of (Al,Ga)As/GaAs. This study was conducted with a view to applying these structures in heterostructure lasers; specifically, phase-locked laser arrays. Broad area lasers fabricated from the quantum well microstructures exhibited threshold current densities as low as 200 Amp/cm².

The major contribution of this work is a new monolithic laser array structure which achieves phase-locking through coupling by diffraction in a central mode-mixing region where the light is unguided. The propagating eigen-modes are index-guided on either side of the mode-mixing region in parallel-element ridge waveguides. The new array displays narrow, single-lobe far-field patterns. The narrowest far-field pattern observed is 2° wide.

An analytic model which explains the characteristics of the observed far-field patterns is presented. This model is developed from a premise with experimental basis.

Accession For

NTIS GRA&I

DTIC TAB ☐

Unannounced ☐

Justification

By

Distribution/

Availability Codes

Dist	Avail and/or Special
A-1	

DTIC COPY INSPECTED 6

PHASE-LOCKED SEMICONDUCTOR QUANTUM WELL LASER ARRAYS

Elias Towe

Technical Report 526

March 1987

Massachusetts Institute of Technology

Research Laboratory of Electronics

Cambridge, Massachusetts 02139

PHASE-LOCKED SEMICONDUCTOR QUANTUM WELL LASER ARRAYS

by

Elias Towe

S.B., Massachusetts Institute of Technology (1981)
S.M., Massachusetts Institute of Technology (1981)

Submitted in Partial Fulfillment of the Requirements
For the Degree of

DOCTOR OF PHILOSOPHY

at the

MASSACHUSETTS INSTITUTE OF TECHNOLOGY
December, 1986

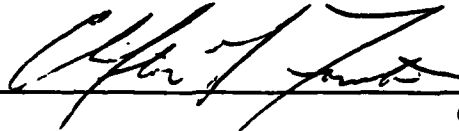Signature of Author _____
Department of Electrical Engineering and Computer Science
December, 1986

Certified by _____
Clifton G. Fonstad, Jr.
Thesis Supervisor

Accepted by _____
Arthur C. Smith
Chairman, Departmental Committee on Graduate Students

Phase-Locked Semiconductor Quantum Well Laser Arrays

by
Elias Towe
Submitted to the Department of Electrical Engineering and Computer
Science
on December 17, 1986 in partial fulfillment of the requirements
for the degree of Doctor of Philosophy

Abstract

This dissertation presents the experimental study of quantum well heterostructures in the III-V compound semiconductor system of (Al,Ga)As/GaAs. This study was conducted with a view to applying these structures in heterostructure lasers; specifically, phase-locked laser arrays. Broad area lasers fabricated from the quantum well microstructures exhibited threshold current densities as low as 200 Amp/cm^2.

The major contribution of this work is a new monolithic laser array structure which achieves phase-locking through coupling by diffraction in a central mode-mixing region where the light is unguided. The propagating eigen-modes are index-guided on either side of the mode-mixing region in parallel-element ridge waveguides. The new array displays narrow, single-lobe far-field patterns. The narrowest far-field pattern observed is 2° wide.

An analytic model which explains the characteristics of the observed far-field patterns is presented. This model is developed from a premise with experimental basis.

Thesis Supervisor: Dr. Clifton G. Fonstad,Jr.
Title: Professor of Electrical Engineering

Acknowledgements

I have been fortunate during both my undergraduate and graduate school years at MIT to have been associated with some outstanding individuals. These individuals, collectively, have contributed much to my education and learning.

I am deeply grateful to Prof. Clifton G. Fonstad for guidance and support during the course of this work. My thesis readers, Prof. Shaoul Ezekiel and Prof. Robert Rediker, have provided useful and constructive criticisms of the work and the thesis manuscript.

It is my pleasure to express thanks to Dr. Alfred Y. Cho at Bell Laboratories in Murray Hill, N. Jersey for the opportunity to work in his laboratory in 1984 as a pre-doctoral assistant and to Dr. Gregory H. Olsen at Epitaxx Inc. in Princeton, N. Jersey for encouragement.

I am grateful to my academic counselor, Prof. Jin Au Kong for his timely moral support and sense of humor throughout my graduate school career. Conversations with him were always enlightening and enjoyable. Prof. Mildred Dresselhaus and Prof. Stephen Senturia provided words of wisdom and encouragement from time to time.

I am grateful to the staff of the Microelectronics Laboratory for their maintenance of the various pieces of equipment needed for this research. The following people deserve mention in this respect: Joe Walsh, Russell Macdonell, Gary Ditmer, Bob Radway, Tom Wester and Paul Maciel. I would also like to thank the members of my research group for a congenial atmosphere and Wai Lee for keeping our evaporator in working order. My thanks also go to Dr. Tom Windhorn, Prof. James Fujimoto and Mr. Steve Yang for their generosity in providing me with equipment that I needed for some of the measurements. Their friendship and technical advice was very much appreciated.

I thank my friends: Prof. Steve Kim, Steve Jens, Darwin Chang, Ning Chan (in Singapore), Dr. James Harrison, Cyrus Bamji, Chon-Mein Wong (at RPI), Gerald Wong (at Bell Labs.), Dr. Michael Stix, Keitaro Wada, Harry chou, Jean-Jacques Hajjar and Bill Song for many enjoyable hours.

My deepest gratitude goes to the members of my family on two continents: the Towes of Kajo-Kōji, Sudan (formerly of Kampala, Uganda) and the Beans of Concord, Massachusetts. I dedicate this thesis to my family for their unconditional love and support.

Concord, Massachusetts   Elias D. Towe
Cambridge, Massachusetts
December, 1986

Dedication

To my family:
the Towes and the Beans,
for their unconditional love and support
and in memory of my mother, Asenetta.

Contents

List of Figures

8

Chapter 1

Introduction

1.1 Overview and Objectives

The need for extremely compact light emitters capable of delivering high optical power in narrow, collimated beams has, in recent years, generated a lot of research interest worldwide in developing such emitters. These devices would find potential applications in optical recording, intersatellite communications, medicine and solid-state laser pumping.

One of the approaches that has received a lot of attention over the years in making these high power devices involves fabricating parallel-element laser arrays on a monolithic semiconductor. The laser elements are made sufficiently close to one another so that the evanescent waves propagating between them cause the elements to interact, thus leading to mutual coupling. The devices are said to be phase-locked if the coupling causes them to operate as a single, coherent source. Typically, however, the far-field emission patterns of these devices have been characterized by dual lobes which sometimes degenerate into complex, multi-lobed patterns [1,2].

In the evanescent wave coupling scheme just described, there is no definite control of how much electromagnetic energy can be coupled from one

11

laser guide to another. This lack of control is so severe that the phase relationship of a wave coupled from one guide to its nearest neighbor cannot be determined *a priori*. As will be discussed later, the phase relationship between nearest-neighbor-elements of the array is the key ingredient in a phase-locked, single-lobed operation of these devices.

The objective of this thesis was to develop a technique, possibly in a new device geometry, where control of the phase relationship of the coupled waves could be established and predetermined. Concomitant with this goal was a need for a systematic study of the semiconductor heterostructures out of which the devices would be fabricated. It was proposed at the inception of the project that the devices would be fabricated out of quantum well heterostructures.

1.2   A Historical Perspective

During the late 1970's, there evolved a need for III-V semiconductor lasers capable of emitting light powers in the range of 20 to 70 mW. The first generation of these high power devices were the so-called large optical cavity (LOC) lasers [3,4]. For the most part, they were operated in a pulsed mode. These devices, though capable of meeting the needs of the time, were still limited in how much ultimate power they could deliver. This is because the highest optical power any semiconductor laser can deliver is limited by the catastrophic mirror damage.

Another class of high power lasers were the facet coated lasers. The outputs of ordinary laser diodes were increased by appropriately coating one facet of the device with anti-reflection coatings. The improvements gained by this method are not very significant in view of the difficulties involved in the deposition of these coatings.

The precursors of the monolithic laser arrays were the discrete arrays. In these devices, a series of individual diode lasers are laid side-to-side and electrically connected in series. The devices were separated from one another by a few millimeters. Optical peak powers in excess of 4 W were achieved from the discrete arrays of this kind [5].

The devices just described satisfied the need for high power. They did not, however, meet the requirement for narrow, collimated beams. Beam forming optics still had to be used to collimate the optical outputs of these devices. This meant that the range of applicability was limited.

The principles of the solution of the problem of obtaining beams with narrow spatial extent in semiconductor lasers are intimately linked to the physics of diffraction in narrow apertures.

The overall size of the ordinary semiconductor laser dictates the spatial extent of the beam emanating from it. In order to circumvent this physical restriction, methods have to be found to increase the lateral effective aperture from which most of the radiation is emitted. It was with this motivation that linear monolithic arrays were developed. If the individual array elements are phase-locked, narrower beams could be achieved. This follows directly from the physics of diffraction. The first evanescently-coupled linear arrays were studied by Ripper and Paoli [6]. These early studies established mutual interaction amongst the elements of the array. The possibilities of phase-locking and beam-stearing were demonstrated at Xerox PARC by Scifres *et al.* [7]. For the majority of the evanescently-coupled devices reported, operation in a narrow, single-lobe has been more of an exception than the rule [8]. This is mainly because there is a lack of control of the phase relationship required for a collective coherence of the array elements. The implementation of a deliberate control mechanism for this phase relationship is crucial for the operation of the devices as a single

coherent source. The exploration and discussion of a method of controlling this relationship are the subject of this thesis.

1.3 Scope of the Thesis

The foregoing sections provided the necessary background and historical perspective of the subject of this work.

In this section, we outline the major topics covered in the sequel. Chapter 2 discusses quantum well heterostructures. The basic physics of these structures is outlined. The optical characterization techniques used are discussed and some of the results are illustrated. In Chapter 3, the consequences of incorporating the quantum well structures in the active cavities of lasers are discussed. A theoretical discussion of the optical gain in quantum well lasers is given. The threshold current densities of quantum well laser devices are calculated based on a strict k-conservation model and compared to experimental results. A brief discussion of the gain broadening mechanisms for these lasers is also given in this chapter. In Chapter 4, the elements of phase-locking in monolithic laser structures are covered. The principles of optical wave guiding in these lasers are discussed. This chapter also introduces the major contribution of this thesis— a new structure for achieving phase-locking in monolithic laser arrays. This structure, the mixed-mode phase-locked (M^2PL) laser array, is a member of a class of diffraction-coupled laser arrays. The quantative condition for in-phase locking is established and the principle of operation of the M^2PL laser array is discussed. In Chapter 5, the experimental results of this work are presented and discussed. An analytic model which explains the characteristics of the observed far-field patterns is presented in this chapter. This model is developed from a premise with experimental basis. Chapter 6 summa-

rizes the work presented in this thesis and gives a discussion of possible future directions based on it. This thesis has two appendices. Appendix A gives a derivation of the confinement factor used in Chapter 3. Appendix B is a technological appendix. The details of the use of a molecular beam epitaxy system are given here. The necessary crystal growth details are also discussed. The second half of this appendix gives a discussion of the processing steps used in the fabrication of the laser devices. No claim is made to the optimality of any of the steps or techniques discussed here. These techniques and steps, however, are the ones found most suitable for the facilities available for this kind of work at MIT.

Finally, the chapters in this thesis are written to be self-contained. The necessary background needed in order to follow the presentation is developed in the course of each discussion.

Chapter 2

Fundamentals of Quantum Wells

As a prelude to discussing quantum wells and their applications in lasers, we first give a simple overview of what is meant by an electronic quantum well in practice.

In the textbook case, an electronic carrier is said to be confined within an energy well when it is in a region of space with low potential energy surrounded by walls of infinitely high potential energy. In this chapter, we will concern ourselves with practical quantum wells. The demonstration and achievement of these type of wells is intimately linked with the science and technology of crystal growth. In recent years, crystal growth techniques [9] and processing methods have advanced to such a state that it is now routinely possible to obtain ultra-thin and pure solid films that exhibit quantum size effects (QSE). Quantum size effects become operative in solid layers when the film or surface depth dimension is comparable to the de Broglie wavelength ($\lambda = h/p \sim L_w$) of the electronic particle or to its mean free path in the layer. These effects also lead to changes in some very basic physical quantities of the semiconductor. Such quantities as the

16

Bohr radius and the Rydberg constant acquire new values in structures containing quantum wells. In the III-V semiconductor compounds, the Bohr radius then ranges from 10 to 500 Å with the corresponding effective Rydberg constants ranging from 100 meV to 1 meV.

When quantum size effects occur, they produce changes in the macroscopic properties of the layer, film or surface. And it is these changes, particularly in the optical and electrical properties of the solid, that are taken advantage of in the design of semiconductor lasers.

2.1 Heterostructure Quantum Wells

The formation of a heterostructure quantum well involves the epitaxial growth of two semiconductor crystals with approximately the same lattice parameter but different band gap energies. In Fig. 2.1, we show the (Al, Ga)As and GaAs semiconductor heterostructure system. The GaAs material, which has a smaller band gap than the (Al,Ga)As, is sandwiched between two layers of the (Al,Ga)As material to form the quantum well. The crystal growth details will be discussed in Appendix B.

The distribution of electronic carriers in a semiconductor with a quantum well is markedly different from that in the bulk crystal. The physical nature of the quantum well imposes a quasi two-dimensional behavior on the carriers. The energies, for example, that each carrier may have are discretized in a prescribed manner. The prescription of the allowed energy levels is governed by quantum mechanics. In a quantum well, such as the one formed in the (Al,Ga)As/GaAs crystal system, we may determine the particular energies that are permitted for occupation by the carriers by solving the Schrödinger wave equation. The Hamiltonian (in the single particle approximation) that is used in this calculation is assumed to be

separable in the cartesian coordinate system. Therefore, for the quantum wells shown in Fig. 2.2, the relavant component of the Hamiltonian would be the y-component which is normal to the epitaxial layer. The lateral component would give rise to the usual, unconfined Bloch carrier states.

We write down the Schrödinger equation to be solved for the problem in Fig. 2.2 as

$$-\frac{\hbar^2}{2m_e}\left[\frac{\partial^2}{\partial y^2} + \Delta E_c(y)\right]\Phi_{cn}(y) = E_{cn}\Phi_{cn}(y) \qquad (2.1)$$

where $\Delta E_c(y)$ is the static crystal potential energy with a zero of energy at the conduction band edge. The E_{cn} are the eigen-energies and the $\Phi_{cn}(y)$ are the associated eigen-functions. The carrier effective mass, m_e, is to be distinguished in the GaAs and the (Al,Ga)As regions as m_{ew} and m_{eb}, respectively. This equation is written for the conduction band quantum well. An analogous equation can be written down for the valence band quantum well. In the valence band, however, the usual degeneracy of the bands for most III-V semiconductors at the Brillouin zone center, is lifted for quantum well structures. It is therefore necessary to take into account both the light and the heavy holes. This will be explained in detail in a later section.

For the two regions of Fig. 2.2, Eq. 2.1 can be split into two auxilliary parts; for region 2,

$$\frac{d^2\Phi_{cn}(y)}{dy_2} - \kappa^2\Phi_{cn}(y) = 0 \qquad (2.2)$$

with the relevant solutions being

$$\Phi_{cn}(y) = Ae^{\kappa y} \qquad y < -L_w \qquad (2.3)$$

Epi-layers　　　　　　Energy Band Structure

(Al, Ga)As

GaAs

(Al, Ga)As

$E_g(Al,Ga)As$

$E_g(GaAs)$

E_v　　　　　　　E_c
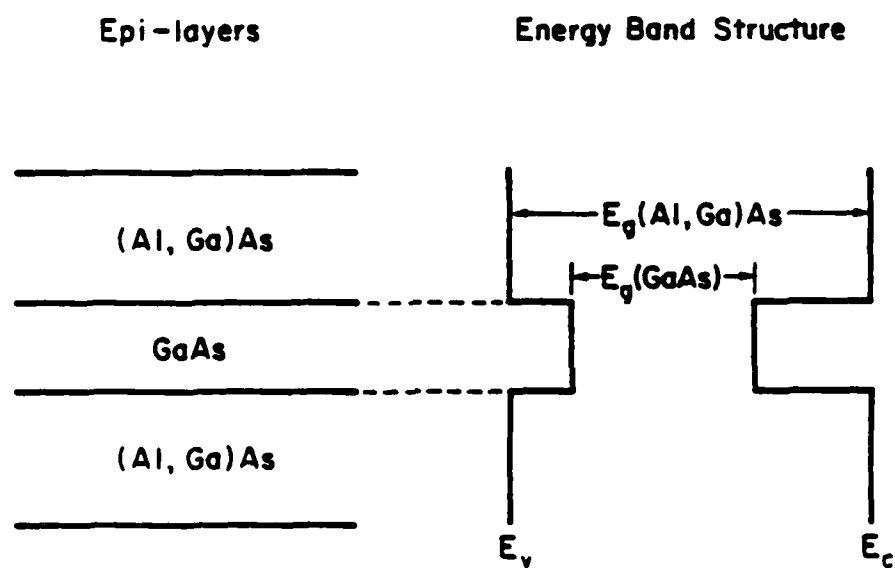
Figure 2.1: The configuration of a GaAs single quantum well sandwiched between two (Al,Ga)As confining layers.

$$\Phi_{cn}(y) = De^{-\kappa y} \qquad y > L_w \qquad (2.4)$$

$$\kappa = \frac{\sqrt{2m_{eb}(\Delta E_c - E_{cn})}}{\hbar} \qquad (2.5)$$

A and D are arbitrary constants of integration. In region 1, the Schrödinger equation is

$$\frac{d^2\Phi_{cn}(y)}{dy^2} + k^2\Phi_{cn}(y) = 0 \qquad (2.6)$$

and the solutions take the form

$$\Phi_{cn}(y) = B\cos ky + C\sin ky \qquad |y| \leq L_w \qquad (2.7)$$

$$k = \frac{\sqrt{2m_{ew}E_{cn}}}{\hbar} \qquad (2.8)$$

The quantities B and C are the arbitrary constants of this integration . By requiring that the eigen-functions of Eqs. (2.3), (2.4) and (2.7) and their first derivatives be continous at the hetero-interfaces, i.e. at $y = \pm L_w$, we obtain the system of equations

$$\begin{pmatrix} -e^{-\kappa L_w} & \cos kL_w & -\sin kL_w & 0 \\ -\kappa e^{-\kappa L_w} & k\sin L_w & k\cos kL_w & 0 \\ 0 & \cos kL_w & \sin kL_w & -e^{-\kappa L_w} \\ 0 & -k\sin kL_w & k\cos L_w & \kappa e^{-\kappa L_w} \end{pmatrix} \begin{pmatrix} A \\ B \\ C \\ D \end{pmatrix} = 0 \qquad (2.9)$$

From this system of equations, we derive the eigen value conditions that

$$k\tan kL_w = \kappa \qquad A + D \neq 0, \ B \neq 0 \qquad (2.10)$$
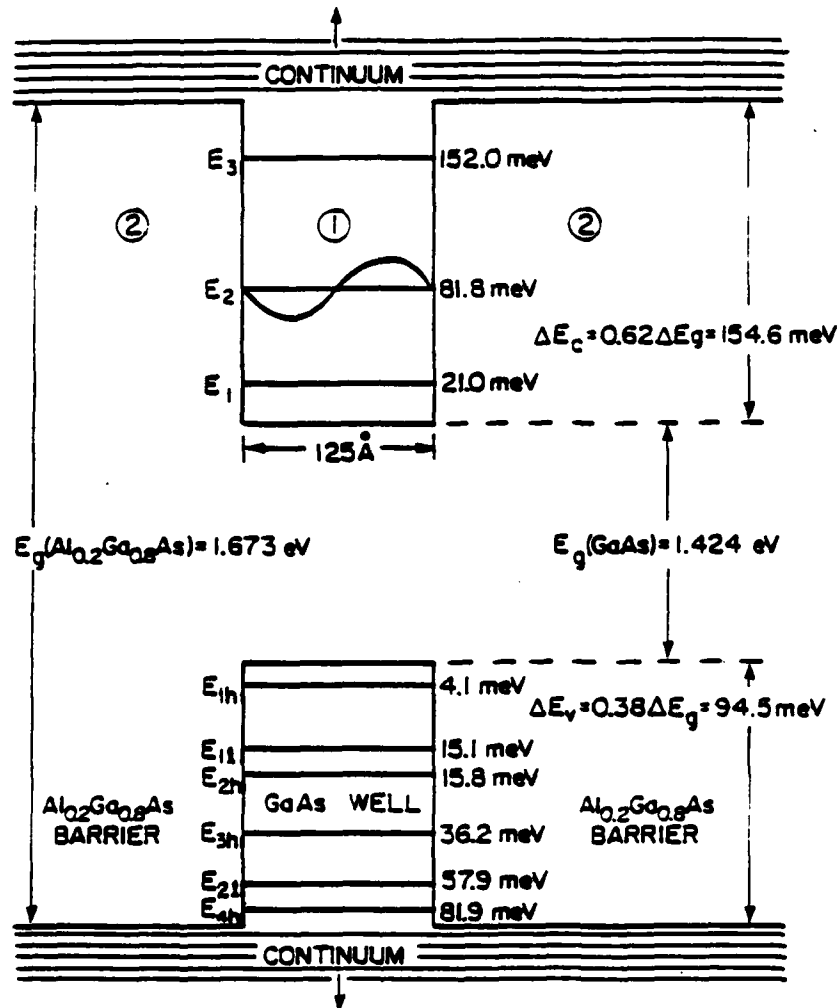
Figure 2.2: The schematic energy band diagram of a single GaAs quantum well in both the conduction and valence bands.

$$k \cot k L_w = -\kappa \qquad A - D \neq 0, \ C \neq 0 \qquad (2.11)$$

These conditions cannot be satisfied simultaneously. Therefore, if at one time Eq. (2.10) is true, it can be shown that the corresponding eigen-state is

$$\Phi_{cn}(y) = (B \cos k L_w)e^{\kappa(y+L_w)} \qquad y < -L_w \qquad (2.12)$$

$$\Phi_{cn}(y) = B \cos ky \qquad |y| \leq L_w \qquad (2.13)$$

$$\Phi_{cn}(y) = (B \cos k L_w)e^{-\kappa(y-L_w)} \qquad y > L_w \qquad (2.14)$$

This state is said to have *even parity*. On the other hand, when Eq. (2.11) is valid and Eq. (2.10) is not, the correct eigen-state is given by

$$\Phi_{cn}(y) = (-C \sin k L_w)e^{\kappa(y+L_w)} \qquad y < -L_w \qquad (2.15)$$

$$\Phi_{cn}(y) = C \sin ky \qquad |y| < L_w \qquad (2.16)$$

$$\Phi_{cn}(y) = (C \sin k L_w)e^{-\kappa(y-L_w)} \qquad y > L_w \qquad (2.17)$$

This state has *odd parity*.

Since the eigen-states of Eqs. (2.12- 2.14) and Eqs. (2.15- 2.17) represent bound electron states in the well, the arbitrary constants B and C can be determined by imposing a normalization condition such that

$$\int_{-\infty}^{\infty} |\Phi_{cn}(y)|^2 dy = 1 \qquad (2.18)$$

The eigen-energies, E_{cn}, for the bound states in the quantum well are determined from Eq. (2.10) for n even and from Eq. (2.11) for n odd. From the definition of κ in Eq. (2.5) and k in Eq. (2.8) and the eigen-value of Eq. (2.10) and Eq. (2.11), we can write a single eigen-value equation implicitly for the system as

$$\sqrt{\frac{m_{eb}}{m_{ew}}\left[\frac{V_o - E_n}{E_n}\right]} = \left\{ \begin{array}{l} \tan \sqrt{(m_{ew}L_w^2 E_n)/(2\hbar^2)} \\ -\cot \sqrt{(m_{ew}L_w^2 E_n)/(2\hbar^2)} \end{array} \right. \tag{2.19}$$

where $V_o(= \Delta E_c)$ is the well depth, L_w is the well width, E_n is the n-th eigen-energy, m_{ew} and m_{eb} are the electron effective masses in the well and in the barrier, respectively. Eq. (2.19) can be transformed into dimensionless form by writing

$$\begin{array}{rcl} \rho^2 & = & (m_{eb}L_w^2 V_o)/2\hbar^2 \\ \xi^2 & = & (m_{ew}L^2 E_n)/2\hbar^2 \end{array} \tag{2.20}$$

With this transformation, Eq. (2.19) becomes

$$\sqrt{\rho^2 - \frac{m_{eb}}{m_{ew}}\xi^2} = \left\{ \begin{array}{l} \xi \tan \xi \\ -\xi \cot \xi \end{array} \right. \tag{2.21}$$

Eq. (2.21) is now in a form that can be solved graphically. If we plot the left hand side of Eq. (2.21) as a function of ξ and the right hand side also as a function of ξ, the intersections specify values of ξ which are solutions to Eq. (2.21). By use of Eq. (2.20), we can then determine the eigen-energies, E_n.

For a typical quantum well width of $L_w = 125$ Å, we have plotted the solutions of Eq. (2.21) for the even eigen-states of a confined electron in a conduction band quantum well. These solutions are shown in Fig. 2.3. The electronic band parameters used are listed in Table 2.1. The complete set of eigen-energies for the $Al_{0.2}Ga_{0.8}As/GaAs/Al_{0.2}Ga_{0.8}As$ single well structure

with a width of 125 Å is shown on Fig. 2.2.

Table 2.1: Electronic Band Parameters

$m_e(x) = (0.067 + 0.083x)m_o$ $\quad$ $m_{lh}(x) = (0.087 + 0.063x)m_o$

$m_{hh}(x) = (0.450 + 0.140x)m_o$ $\quad$ $m_o = 9.109 \times 10^{-31}$ kg

$E_g(x) = 1.424 + 1.247x$ eV $\quad$ $\Delta E_g = E_g(x) - E_g(0)$ eV

$\Delta E_c = 0.62 \Delta E_g$ $\quad$ $\Delta E_v = 0.38 \Delta E_g$

$V_o = \Delta E_c(\Delta E_v)$ $\quad$ $L_w = 125$ Å

$x = 0.2$

2.2 Multiple Quantum Wells and Superlattices

The major difference between a multiple quantum well system and a super-lattice is the relative magnitude of the barrier layer thickness L_b, and its relationship to the wave function penetration depth L_p, into the barrier. In multiple quantum wells, the barrier thickness L_b, is much bigger than the wave function penetration depth L_p (i.e. $L_b >> L_p$). Therefore, the wave functions of adjacent wells do not overlap, and the physical properties of the multiple quantum well system are those of an independent set of wells. Most of the physics of these systems can therefore be studied in a single quantum well and is not restricted to the multiple quantum well systems. As a practical matter though, the signal-to-noise ratio is much better in

CONFINED ELECTRON STATES
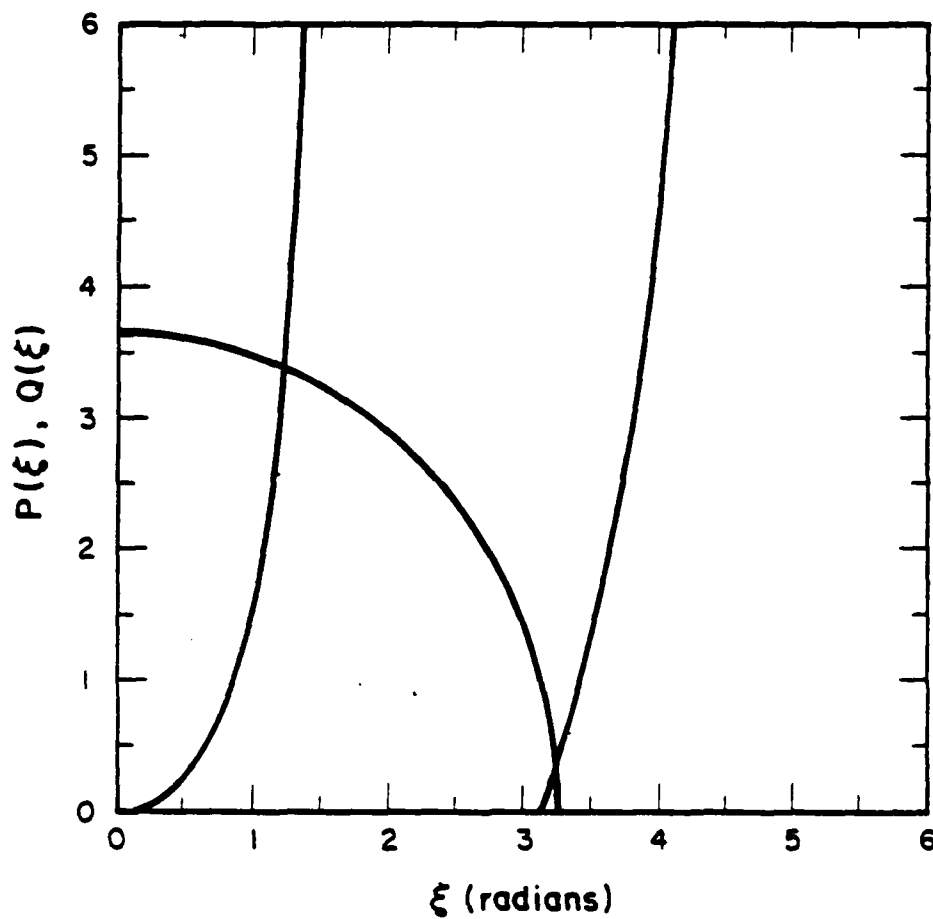
Figure 2.3: A graphical solution of the eigen value energy equation for the even states in a single quantum well.

multiple quantum well systems for any given experiment on these struc-
tures. This is one of the main reasons for working with multiple quantum
well structures rather than a single quantum well structure.

In superlattices, which in principle, are any set of infinite, periodic lay-
ers, the barrier thickness L_b, is much less than the wave function penetra-
tion depth L_p; this means that the wave functions of adjacent wells interact
and the confined particles are delocalized. The physical properties of these
structures therefore depend on the super periodicity superimposed on top
of the lattice periodicity. The energy distribution of the delocalized carriers
in the superlattice takes on a new form. The discrete energy distribution
characteristic of isolated quantum well structures changes into mini-bands
separated by mini-gaps. We illustrate in Fig. 2.4, the periodic form of the
potential energy a particle would see in the vertical direction of epitaxial
growth (y-direction) for a superlattice. We have only shown the conduction
band energy profile. This is the Kronig-Penney potential energy profile.

The Hamiltonian for a carrier in this type of potential, in the single
particle approximation, is

$$\left.\begin{array}{rcl} H & = & p^2/2m_e + \Delta E_c(y) \\ \Delta E_c(y) & = & \Delta E_c(y + a) \end{array}\right\} \qquad (2.22)$$

The parameters have their usual meanings, a, however, is the period of the
superlattice. The eigen-functions of such a Hamiltonian come in product
form and they are a consequence of Bloch's theorem [12]. These eigen-
functions are written as

$$\Phi_{cn}(y) = e^{-jky}u(y) \qquad (2.23)$$

The conditions that the eigen-functions Φ_{cn} satisfy are very similar to those
satisfied by the eigen-functions of the single quantum well discussed earlier.
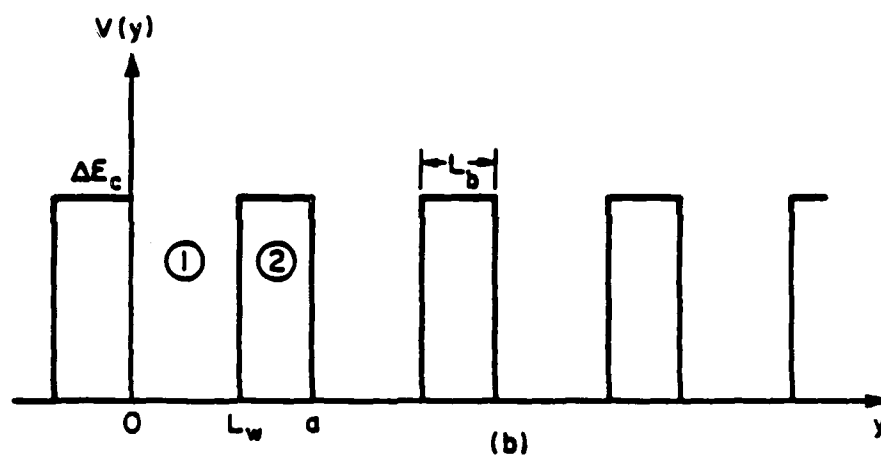
Figure 2.4: The periodic potential energy profile seen by a particle in the conduction band of a superlattice structure.

$\Phi_{cn}(y)$ and its derivative must be continous and periodic. In region 1 of the well domain of the potential,

$$\left.\begin{array}{rcl} \Phi_{cn}(y) & = & Ae^{jk_1y} + Be^{-jk_1y} \\ k_1 & = & \sqrt{(2m_{cw}E_{cn})}/\hbar \end{array}\right\} \qquad 0 \le y \le L_w \qquad (2.24)$$

In region 2 of the barrier,

$$\left.\begin{array}{rcl} \Phi_{cn}(y) & = & Ce^{jk_2y} + De^{-jk_2y} \\ k_2 & = & \sqrt{2m_{cb}(\Delta E_c - E_{cn})}/\hbar \end{array}\right\} \qquad L_w \le y \le L_w + L_b = a$$

$$(2.25)$$

The continuity conditions mentioned earlier can be applied to Eq. (2.24) and Eq. (2.25). In an exactly analogous way to Eq. (2.9) we can derive the 4×4 coefficient matrix that represents these continuity conditions. The vanishing of the determinant of this matrix gives the eigen-value equation which is also the dispersion relation (a bit of algebra is involved in deriving this result). This relation is

$$\cos ka = \frac{k_2^2 - k_1^2}{2k_1k_2} \sin k_1 L_w \sinh k_2 L_b + \cos k_1 L_w \cosh k_2 L_b \qquad (2.26)$$

with the parameters k_1 and k_2 given as in Eq. (2.24) and Eq. (2.25) respectively. Eq. (2.26) can be solved graphically to determine the allowed eigen-energies for the superlattice structure. By separately plotting the left hand side and the right hand side of Eq. (2.26) on the same graph, we determine from the intersections, the allowed eigen-energies. The wavevector k has real values when $-1 \le \cos ka \le 1$ and it is in this range of k values that the eigen values of E_{cn} are defined.

We illustrate in Fig. 2.5, a computer generated solution of Eq. (2.26). In the solution of this equation, for values of $E_{cn} > \Delta E_c$, the hyperbolic

sine and cosine functions revert back to normal trignometric sine and cosine functions. In Fig. 2.5, we have also shown the allowed and forbidden energy bands characteristic of a superlattice structure. This particular superlattice is composed of quantum wells exactly the same size as the single quantum well treated earlier. The barrier thicknesses, however, are only $L_b = L_w/15$. We have therefore used the same electronic band parameters in Table 2.1. From the graphical solution, we extract the information that the eigen-energies occur in four discrete ranges given by

$$
\begin{aligned}
0.06 &\leq E_{c1}/\Delta E_c \leq 0.2 \\
0.33 &\leq E_{c2}/\Delta E_c \leq 0.82 \\
0.94 &\leq E_{c3}/\Delta E_c \leq 1.84 \\
1.93 &\leq E_{c4}/\Delta E_c \leq 3.27
\end{aligned}
\tag{2.27}
$$

These mini-bands are shown in Fig. 2.6. The energy levels of a single quantum well are also shown alongside the superlattice mini-bands. For the same well size, the mini-bands of the superlattice lie in the ranges that correspond to the discrete energy levels of the single quantum well. We note, however, that a new feature absent in the single well energy spectrum appears in the superlattice energy quantization. Whereas the energy spectrum of a single well outside the potential well is characterized by a continuum of states, that outside the periodic potential of the superlattice is still discretized into mini-bands. Resonances due to the mini-bands outside the periodic wells have recently been observed [13].

We have just quantitatively discussed the main differences between a superlattice and a multiple quantum well system. The properties of a superlattice are primarily due to particle delocalization which leads to the creation of allowed and forbidden energy mini-bands. This feature is true for both the conduction and valence bands. Because of the degeneracy of the valence band, however, the effect is a little bit more complicated.

ENERGY SPECTRUM OF A SUPERLATTICE
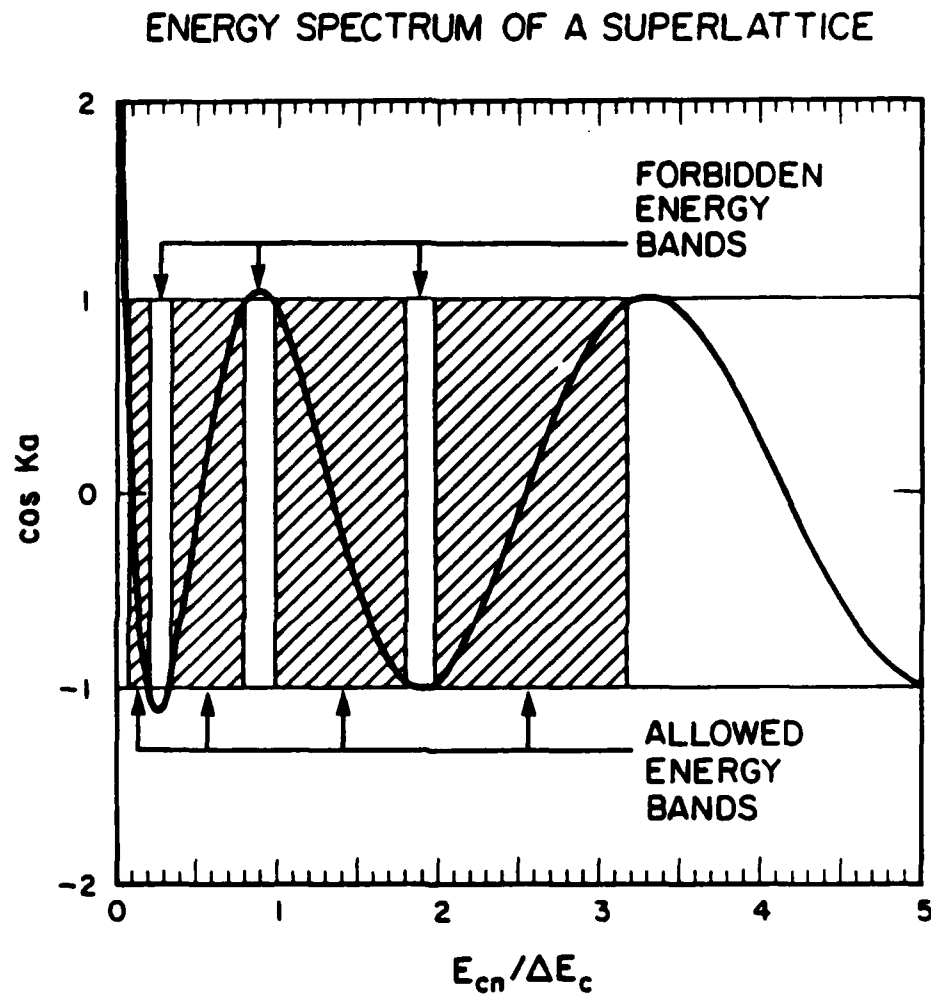
Figure 2.5: The energy spectrum of a superlattice.
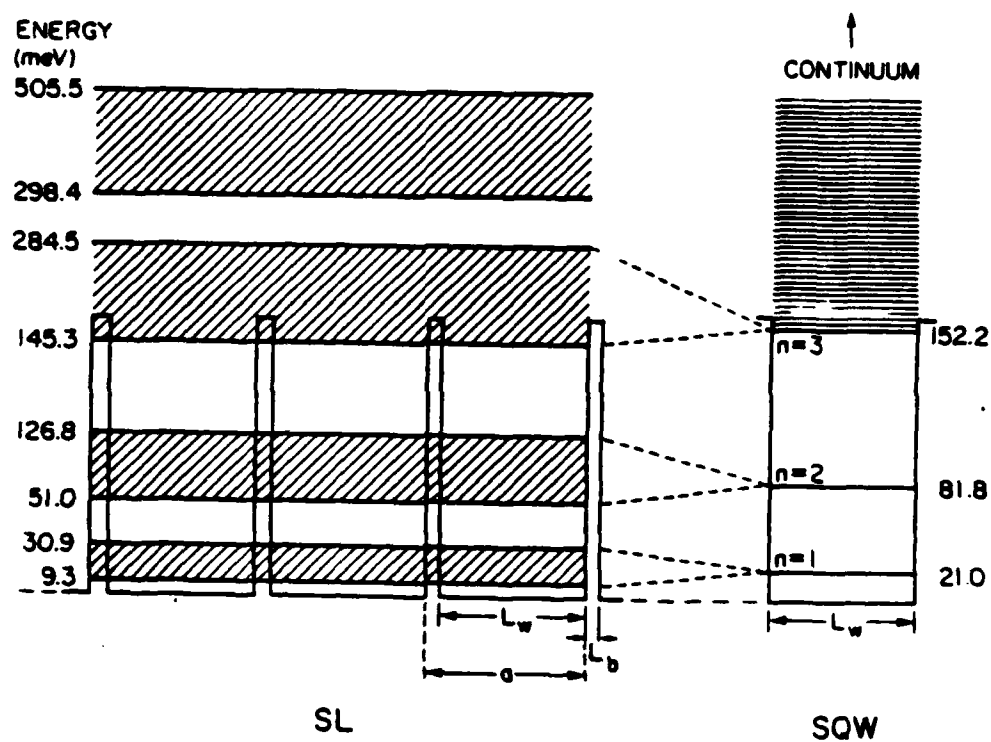
Figure 2.6: The energy band diagram of a superlattice alongside that of a single quantum well structure. The energies in the superlattice split into minibands with forbidden minizones between the allowed sub-bands.

In bulk III-V compounds, the valence bands consist of the two degenerate levels which are due to the $J = 3/2$ momentum multiplet at the center of the Brillouin zone. The spin-orbit interaction of the electrons results into a split-off band for $J = 1/2$. Using $k.p$ perturbation theory, Dresselhaus [10] showed that the energy expression expected for the $J = 3/2$ multiplet is

$$E_v(k) = Ak^2 \pm \left[B^2 k^4 + C^2 \left(k_x^2 k_y^2 + k_y^2 k_z^2 + k_z^2 k_x^2 \right) \right]^{1/2} \qquad (2.28)$$

which is a fluted ellipsoidal energy surface. The x, y and z refer to the crystallographic directions. Since for the GaAs wafers we use, the quantum wells are parallel to the (100) crystallographic direction, Eq. (2.28) becomes

$$E_v(k) = (A \pm B)k^2 \qquad (2.29)$$

In the Luttinger Hamiltonian [11] description of the energy dispersion relation, the parameters A and B in Eq. (2.29) have been related to the Luttinger parameters γ_1 and γ_2 through the relationship $A \pm B = (\gamma_1 \pm 2\gamma_2)/m_o$ where m_o is the free electron mass [14]. This relationship defines two different masses for the degenerate bands. Because the two masses are different, the effects of confinement in the y-direction for each one of them are different. At the zone center, the degeneracy is lifted and the result is a creation of two distinct valence band eigen-states for each allowed qauntum number.

2.3 Density of States for Quantum Well Structures

In bulk III-V compound semiconductors where the energy dispersion relations are approximately parabolic near the Brillouin zone center, the joint

density of occupiable electronic states can be shown to be given by [15]

$$D_{vc}(E) = \frac{2}{8\pi^3} \int \int \frac{dS}{\nabla_k(E_c - E_v)} \Big|_{E_c - E_v = E} = \frac{1}{2\pi^2} \left(\frac{2m_h m_e}{m_h + m_e} \cdot \frac{1}{\hbar^2} \right)^{3/2} \sqrt{E - E_g}$$

(2.30)

In quantum wells, the carriers are constrained to move in the plane parallel to the layers. If y is the direction of confinement, then motion is only possible in the $x - z$ plane. The joint density of states in this case is given by

$$D_{vc}(E) = \frac{2}{4\pi^2} \int \frac{dl}{\nabla_{k_{||}}(E_c - E_v)} \Big|_{E_c - E_v = E}$$

(2.31)

The operator $\nabla_{k_{||}}$ is the directional second derivative of the energy difference-function parallel to the epi-layers. This joint density of states as given here is per unit range of energy per unit area. For a quantum well of width L_w, the joint density of states per unit range of energy per unit volume can be expressed as

$$D_{vc}(E) = \left(\frac{m_h m_e}{m_h + m_e} \right) \frac{1}{\pi \hbar^2 L_w} \sum_n u_{-1}(E - \Delta E_n)$$

(2.32)

where $u_{-1}(E - \Delta E_n)$ is the unit step function and $\Delta E_n = E_{cn} - E_{vn}$ is the energy difference between two allowed conduction and valence band states.

We note that the confinement of carriers in the quantum well structure produces a distinctly different density of states function from what is usual in a bulk crystal. The major differences stem from the energy independence of the two-dimensional density of states for a given energy range. Also, the two-dimensional density of states has a step-like functional dependence. The differences lead to markedly contrasting observable optical properties. In the next section, we discuss our experimental observations of some of these properties.

2.4 Experimental Characterization of Quantum Wells

The basic tools we used to characterize the quantum well structures in this study were: high resolution scanning electron microscopy (SEM), absorption measurements and photoluminescence. Each one of these tools contributes a unique piece of information to the overall program of study. We cover some of the experimental details in what follows.

2.4.1 Scanning Electron Microscopy

Because of the extremely small (sub-micron) dimensions involved in the quantum well structures, techniques such as optical microscopy of the cleaved and chemically stained epi-layers, cannot be of any use. In some cases even the resolution of the SEM is not good enough. In these cases, transmission electron microscopy (TEM) must then be used. The high resolution SEM photo-micrographs are useful for examining the hetero-interfaces of the structures. They are also useful for determining the thicknesses of the grown hetero-layers.

In Fig. 2.7, we show an SEM photo-micrograph of a superlattice buffer layer grown on top of a GaAs buffer. From this photograph, it is possible to resolve and follow the evolution of a defect structure originating from the substrate. Notice how the defect structure smoothes out with each additional superlattice layer grown. This kind of information can only be obtained by use of the SEM. In the next photo-micrograph, Fig. 2.8, we show a full single quantum well (SQW) laser structure. A higher resolution photomicrograph of the SQW is shown in Fig. 2.9. It is evident from this picture that the hetero-interfaces at the SQW are not very smooth. Also, there are variations in the well thickness across the wafer. These variations

manifest themselves in the photoluminescence spectra.

2.4.2 Optical Absorption Measurements

Optical absorption measurements are generally performed to determine the energy thresholds that correspond to the electronic transitions between the highest nearly filled band and the lowest nearly empty band. In general, absorption is very small for photon energies below the band edge and it increases rapidly for values above the band gap.

The simplest and most direct way of observing the fundamental absorption edge is to determine the absorption from transmission measurements. This is the method we use.

Absorption, as the name suggests, involves the promotion of electronic carriers from low energy states to high energy states by the absorption of some energy from incident photons. The process is quantum mechanical in nature and its full quantitative description involves electromagnetic field-quantization theory [16]. We discuss here, however, the semi-qualitative arguments that explain our experimental results. From the definition just given, for photon absorption between two discrete states, the absorption coefficient is given by

$$\alpha(E) = B_{12}(f_1 - f_2)(n_{eff}/c) \tag{2.33}$$

where f_1 and f_2 are the Fermi occupation probabilities for the low and high energy states, (c/n_{eff}) is the photon velocity in the material as modified by the index of refraction n_{eff}. B_{12} is a constant of proportionality; in fact it is the Einstein B-coefficient which is the probability that the transition can occur. This transition probability can be calculated by use of Fermi's "Golden Rule". The rule involves the calculation of the interaction Hamil-

n-GaAs/AlGaAs SLB (50% Al)
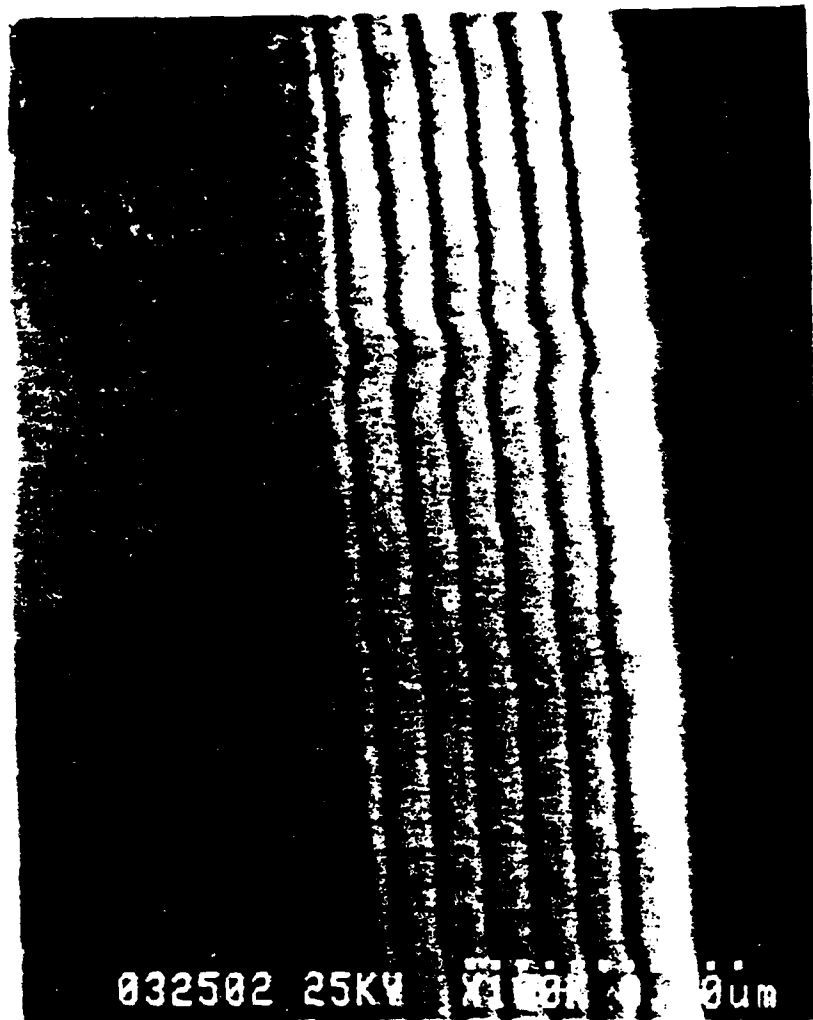
Figure 2.7: An SEM photomicrograph of a superlattice.

n-GaAs Buffer Layer

n-GaAS/AlGaAs SLB Layer
(50% Al)

n-AlGaAs Cladding Layer
(50% Al)

AlGaAs Waveguide Layer
(graded)

GaAs SQW Layer

AlGaAs Waveguide Layer
(graded)

(undoped)
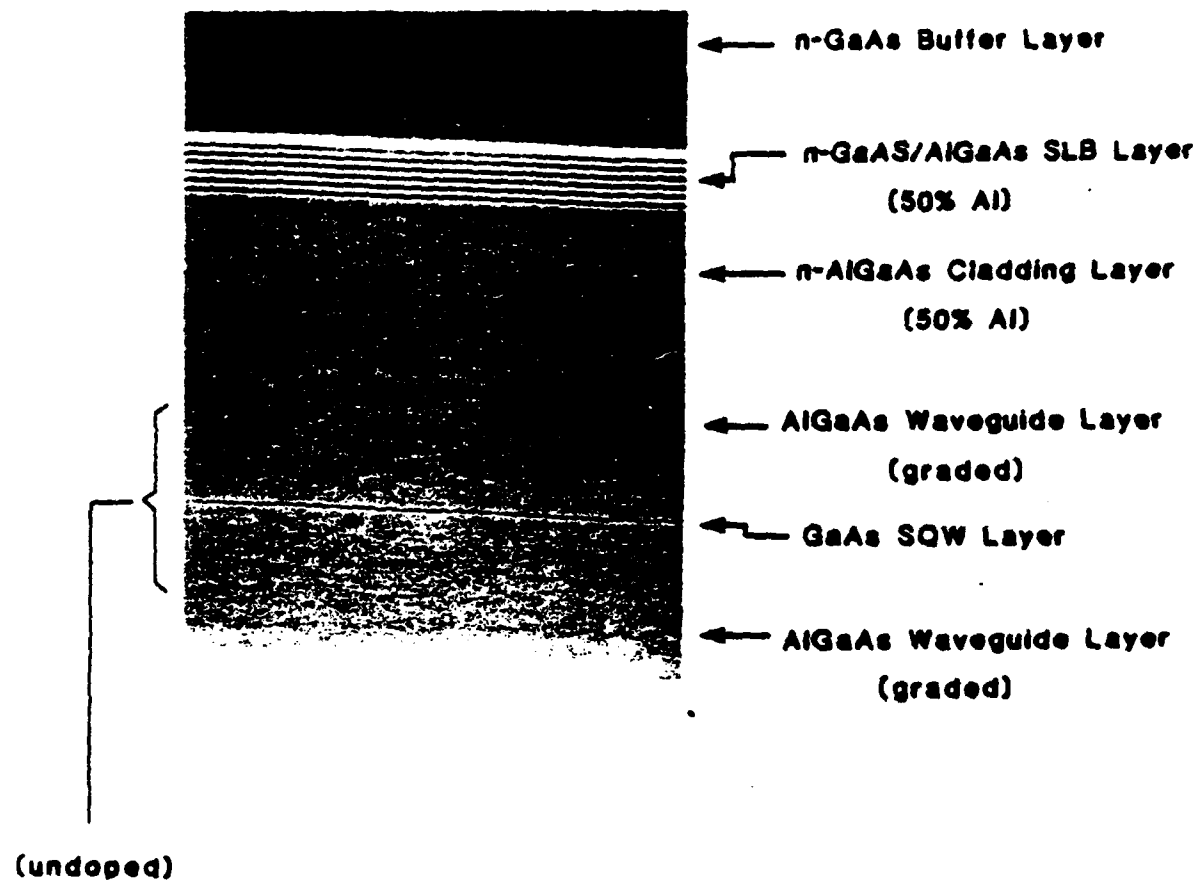
Figure 2.8: An SEM photomicrograph of a single (Al,Ga)As/-GaAs/(Al,Ga)As quantum well laser structure.
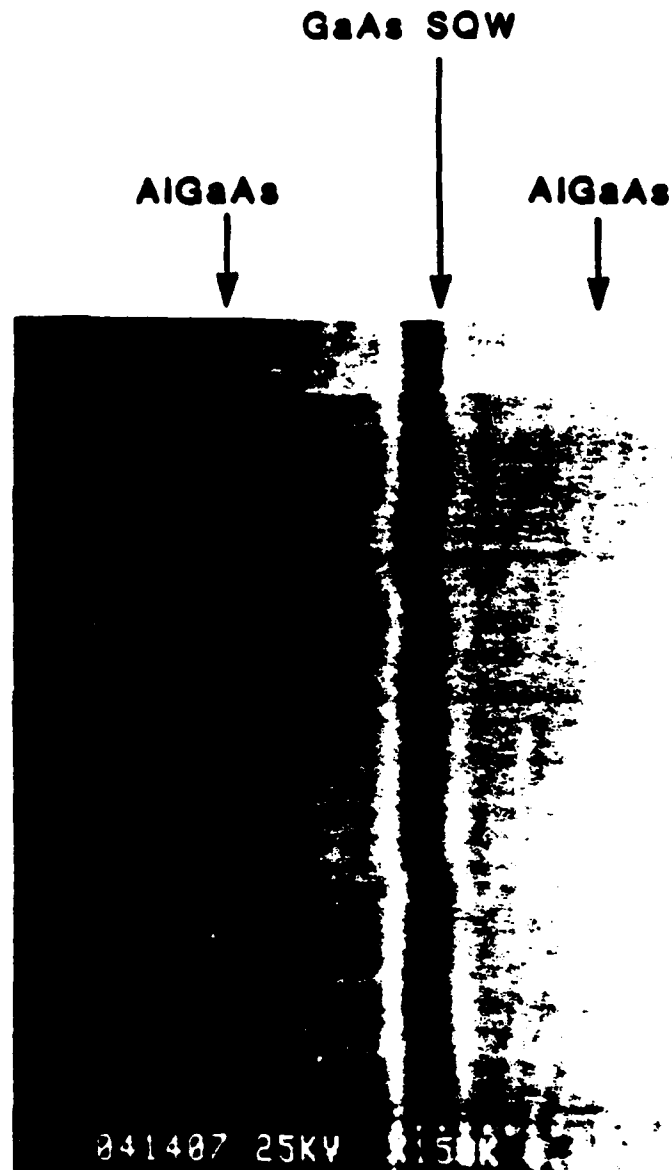
Figure 2.9: A high resolution SEM photomicrograph of the active region of a SQW laser structure.

tonian by solving Schrödinger's equation with a perturbation harmonic in time [17]. Since this result is well documented in the literature, we shall not derive it here. For bulk semiconducotrs, the transition probability is usually given as [18]

$$B_{12} = \frac{\pi e^2 \hbar}{m_e^2 \epsilon_o n_{eff}^2(E)} |M|^2 \qquad (2.34)$$

where $|M|$ is the momentum matrix element. The other symbols have their usual meanings. The matrix element M is defined as

$$M = \langle \Psi_2^*(r) | \vec{p} | \Psi_1(r) \rangle \qquad (2.35)$$

$\Psi_1^*(r)$ and $\Psi_2(r)$ are the particle wave functions for the low and high energy states. The momentum $\vec{p}$ is utilized in its quantum mechanical operator form. For quantum well structures, we have to modify the functions $\Psi_1^*(r)$ and $\Psi_2(r)$ to include the effects of the two-dimensional confinement. We do this by writing, for example,

$$\Psi_1^*(r) = \Phi_{vn}^*(y) u^*(r) \qquad (2.36)$$

where Φ_{vn}^* is the envelope function that describes carrier confinement in the direction of epitaxial growth. These class of functions was described in Section 2.1. The function $u^*(r)$ is the regular Bloch function.

In the absorption process, when more that two energy states are involved, we must include the density of those other occupiable states. The density of these states was derived earlier for quantum well structures. From Eq. (2.32) and Eq.(2.33), the absorption coefficient is given by

$$\alpha(E) = \int_{-\infty}^{\infty} B_{12}(f_1 - f_2) \left[\frac{m_h m_e}{m_h + m_e} \right] \frac{1}{\pi \hbar^2 L_w} \sum_n u_{-1}(E - \Delta E_n)(n_{eff}/c) dE \qquad (2.37)$$

with B_{12} given as in Eq. (2.34).

The step-like nature of the density of states derived earlier and used in Eq. (2.37) should give the absorption spectrum a similar dependence.

Experimentally, the samples used consist of either a single quantum well or a set of multiple quantum wells sandwiched between two layers of cladding material, each about 1.5 μm thick. Fig. 2.10 shows the structure and composition of a typical wafer used in this experiment. Since the structures are grown on GaAs substrates, these and the other buffer layers must be removed before the absorption measurement is performed. The wafer is glued, with substrate side up, on an optically flat sapphire window. This is done with an epoxy resin whose index of refraction is matched to the sapphire window. Care must be taken during the process to avoid any stress on the wafer. The wafer is then mechanically and chemically polished down to approximately 3 μm. In order to avoid Fabry-Perot etalon reflections during the measurement, the top surface of the wafer is made slightly rough.

The experimental set-up is shown in Fig. 2.11. It is, for the most part, self-explanatory. The optical absorption is measured by registering the transmitted light and comparing it with that obtained from a bare sapphire window of the same thickness placed in the path of the light. The light transmitted is analyzed by a spectrometer and stored in an optical multi-channel analyzer (OMA). The OMA makes comparison of the stored signals in non-real time easy and straight forward. Fig. 2.12 shows the room temperature absorption measurement for a single quantum well sample. Similar results are obtained for multiple quantum well structures. The step-like nature of the absorption is fairly evident. The steps in the absorption spectrum correspond to absorption due to the different quantized energy levels. This type of absorption is consistent with the concept of two-dimensional carrier confinement and the quantization of the energy in the

1.5 μm $\quad$ $Al_{0.5}Ga_{0.5}As$

MQW's $\quad$ $GaAs/Al_{0.2}Ga_{0.8}As$
$125\text{Å}/200\text{Å}$

1.5 μm $\quad$ $Al_{0.5}Ga_{0.5}As$
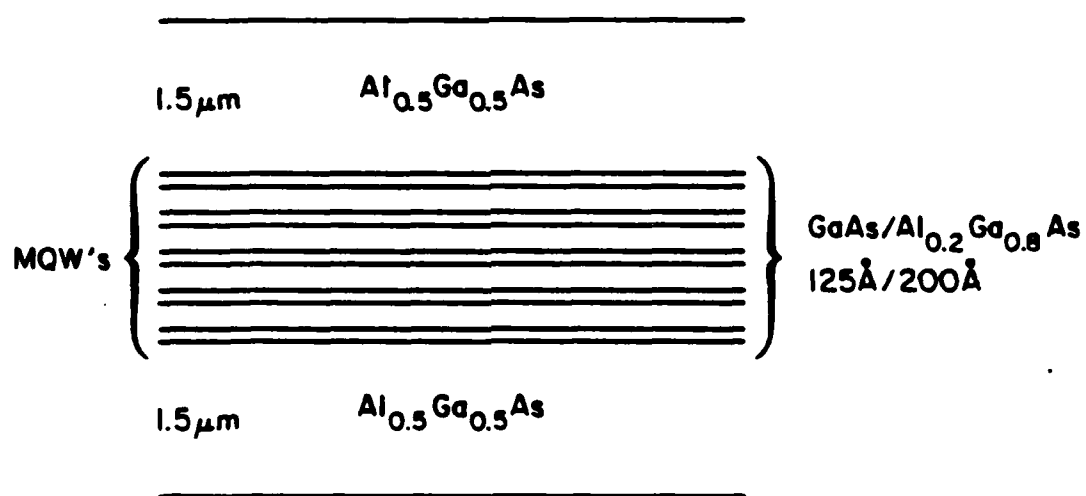
Figure 2.10: The structural composition of a typical sample used in the absorption and photoluminescence studies.

direction of confinement. Results similar to these have been obtained in the InAs-GaSb material system for cryogenic sample temperatures [19]. And more relavant to the material system used here, similar results have been reported for the (Al,Ga)As/GaAs system [20,21]. Recently, exitonic effects have also been observed in room temperature experiments in addition to the step-like nature of the absorption [22].

2.4.3   Photoluminescence

The most common, rapid and straight forward method of assessing the optical quality of direct gap semiconducotrs is photoluminescence. This method is especially useful when the epitaxial layers are intended for use in photonic devices. The technique of photoluminescence involves the optical radiation emitted by an irradiated semiconductor (irradiated usually with a coherent laser light).

The major processes that take place in this excitation include:

- creation of electron-hole pairs by the absorbed light,

- radiative recombination of the electron-hole pairs and

- escape of this recombination radiation from the sample.

There are two types of electronic transitions that lead to radiative recombination in an optically irradiated sample. The first type of transition involves what is known as *intrinsic transitions*. These are transitions involving the recombination of an electron from the conduction band with a hole in the valence band. The second type of radiative recombination involves the recombination of say an electron trapped at an impurity site just below the conduction band with a hole in the valence band. An analogous recombination can also occur between an electron returning from the
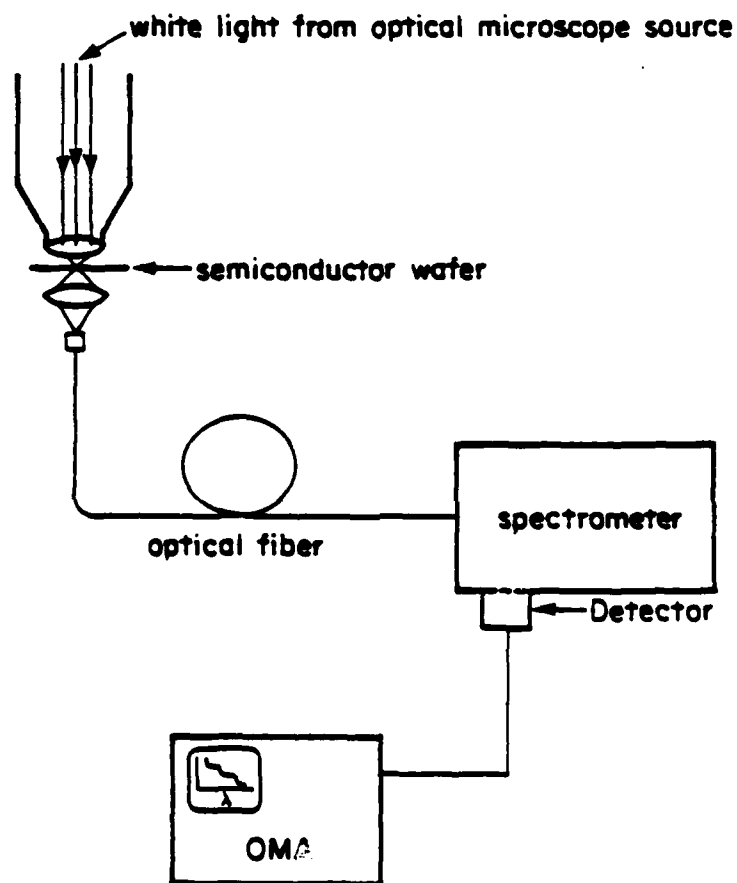
Figure 2.11: A schematic diagram of the absorption measurement set-up.
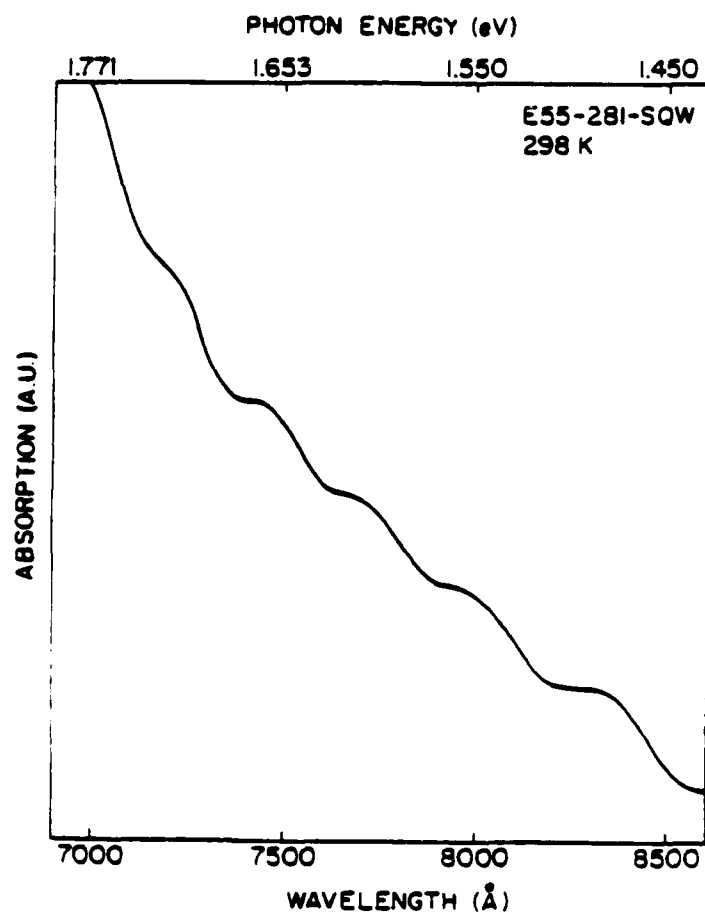
Figure 2.12: A room temperature spectrum of the absorption of a quantum well structure.

conduction band with a shallow impurity site just above the valence band. These types of transitions are known as *extrinsic transitions*

The character of the transitions involved in quantum well structures is a little different from those that occur in bulk crystals. In quantum wells, the transitions occur between selection rule-allowed states. For the schematic energy band diagram shown in Fig. 2.13, the selection rule is $\Delta n = 0$ for the quantum wells. What is meant by this rule is the fact that transitions are only allowed between states in the conduction and valence band with the same quantum number. This figure also shows the contrasting way in which transitions in the bulk material occur.

A typical photoluminescence experimental set-up is shown in Fig. 2.14. The samples are mounted with vacuum grease on a copper mounting block. The excitation source is a cw Helium-Neon (6238 Å) laser with an output of 15 mW. This power intensity is reduced somewhat on the sample surface depending on the chopper frequency. Generally, less than about 10 mW actually hits the sample. The beam is focused to a spot size of less than a square millimeter on the sample. The photoluminescent light is analyzed by a 0.5 meter scanning spectrometer. The resulting signal is then processed with a lock-in amplifier synchronized to the chopper frequency. Emission intensity and spectral spread are recorded on a chart recorder.

In order to minimize the self-absorption of the radiative recombination light from the quantum well(s) (see Fig. 2.10), the thickness of the top cladding layer of the sample is etched down so that the quantum well(s) is (are) only 1000 Å from the surface. In Fig. 2.15, we show the room temperature photoluminescence spectrum of a bulk GaAs layer and that of a multiple quantum well structure with a superlattice buffer layer incorporated. The reasons for the superlattice buffer are explained in Appendix B. Notice that the emission peak of the multiple quantum well structure
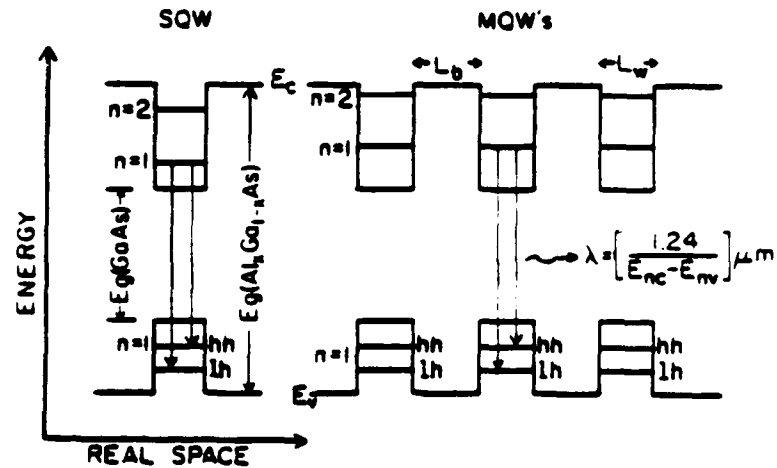
(a) SQW and MQW's Optical Transitions
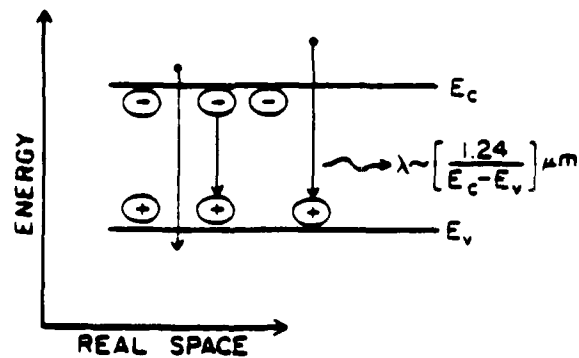
(b) Bulk $Al_x Ga_{1-x} As$ Optical Transitions

Figure 2.13: The band diagram of a single and a multiple quantum well system showing the allowed transitions. Also shown in (b) are the transitions in a bulk crystal.
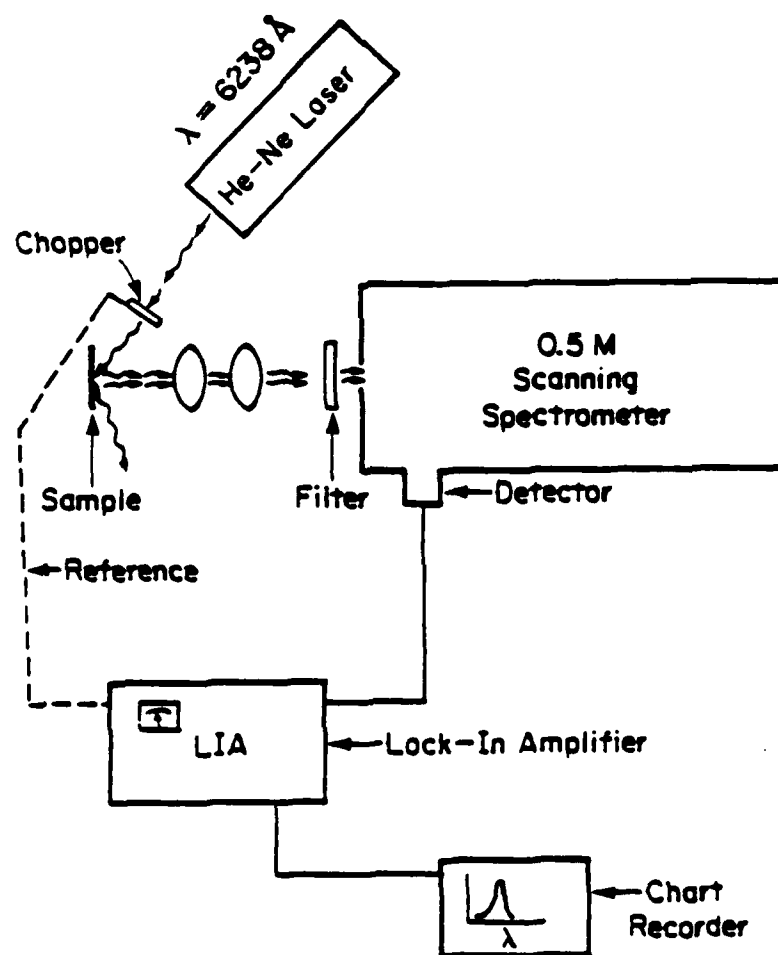
Figure 2.14: The schematic diagram of the photoluminescence set-up used in this work.

is shifted from that of the bulk layer. This shift is due to the carrier confinement effect. The emission of the multiple quantum well structure is predominantly due to the $n = 1$ sub-band transition. This is the electron to heavy hole ($e \rightarrow hh$) transition. The electron to light hole ($e \rightarrow lh$) transition is also clearly identifiable.

In an earlier section, we performed sub-band energy calculations for a single quantum well with a width of 125 Å. In Fig. 2.16, we show the luminescent spectrum of a particular single quantum well structure with a well width of 125 Å and an aluminum composition of 0.2 in the cladding layers. From the theoretical calculations, we showed that the $1e \rightarrow hh$ transition involves an energy change of 1.4491 eV which corresponds to an emission wavelength of $\lambda \sim$8557 Å. This value is in good agreement with the experimental photoluminescence peak assignment of this transition to $\lambda \sim$8530 Å. The calculated $1e \rightarrow lh$ transition involves an energy change of $\sim$1.4601 eV which corresponds to $\lambda \sim$8493 Å. This value again is in good agreement with the observed value of 8500 Å.

In the light-hole region, there is additional structure. The peaks in this region are separated from each other by $\sim$ 7.9 meV. These peaks could arise from fluctuations in the quantum well width. The nonuniformity postulated could be as depicted in Fig. 2.17. If this were the case, then the quantized energy levels as given in the previous sections would split into additional levels due to the fluctuations. The energy change due to a small change in well width can be estimated as follows. Since the structure is on the electron→light hole region, one would assume that the fluctuation mostly affected this transition. The emission energy of this transition in the absence of any perturbations can be written as
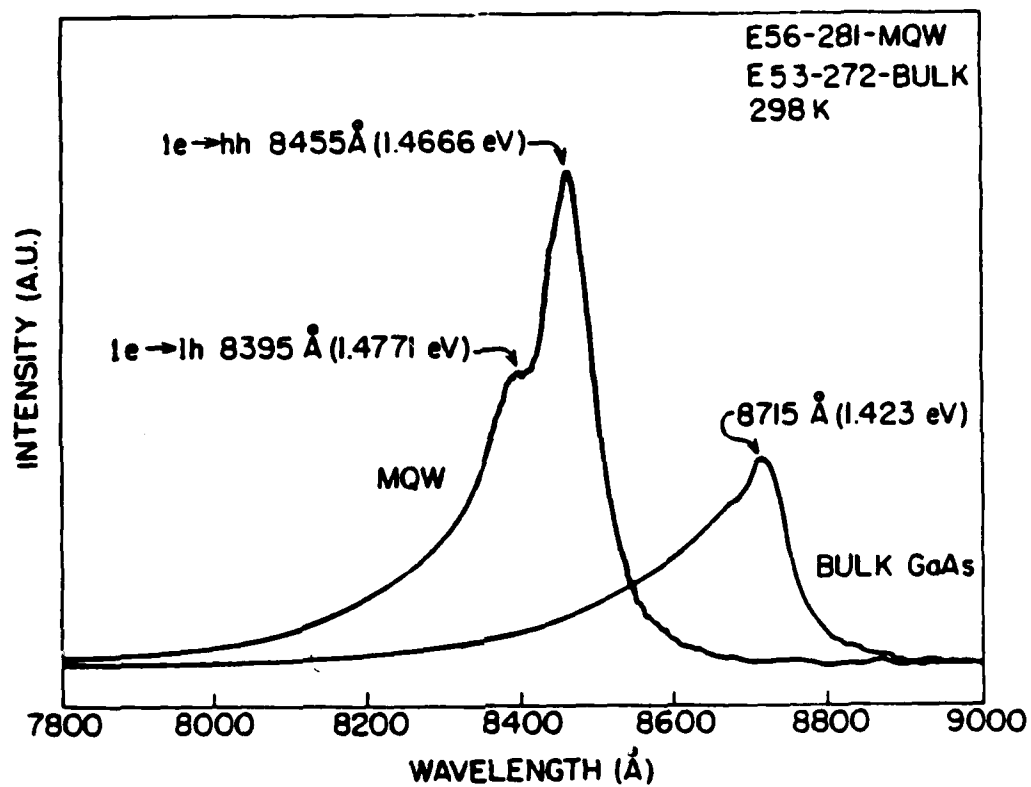
Figure 2.15: The room temperature photoluminescence spectrum of a multiple quantum well structure and that of a bulk crystal.
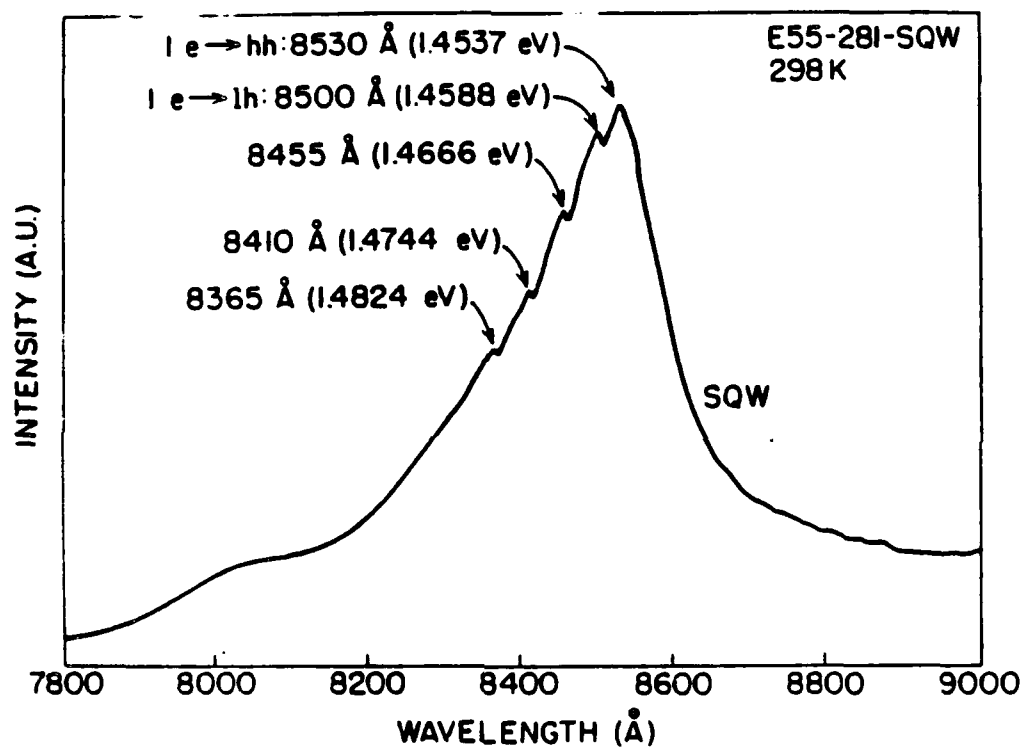
Figure 2.16: The room temperature photoluminescence spectrum of a single quantum well structure.

$$E_{e \to lh} \simeq E_g + \frac{\hbar^2 \pi^2}{2L_w^2} \left[\frac{1}{m_e} + \frac{1}{m_{lh}} \right] \tag{2.38}$$

where E_g is the band gap. This expression uses the simple "particle in a box" approximation. From Eq. (2.38), we see that for a small change in well width, ΔL_w

$$|\Delta E_{e \to lh}| \simeq \frac{\hbar^2 \pi^2}{L_w^3} \left[\frac{m_e + m_{lh}}{m_e m_{lh}} \right] \Delta L \tag{2.39}$$

For a monolayer fluctuation, $\Delta L = a_o/2$ (a monolayer is defined as one half the lattice constant, a_o) the corresponding energy change is ~ 2.9 meV. The parameter values used are those in Table 2.1. The separation energy of the peaks observed in Fig. 2.16 would correspond to a fluctuation of ~ 2.7 monolayers.

The subject of interface disorder and well width fluctuations, has received a lot of attention recently [23]- [31]. Fluctuations ranging from half a monolayer to two monolayers have been reported. In the extreme case where the disordering of the interface is thought to be due to alloy clustering [24], multiple quantum well systems have been reported to have merged and change the expected emission spectra. It has also been claimed that the reported alloy clustering can be avoided by use of the AlAs/GaAs system [25]. In another report, it is thought that the growth of (Al,Ga)As/GaAs quantum wells at high substrate temperatures (> 690°) leads to more disorder and fluctuations in the quantum well widths [30].

The most common manifestation of the well width fluctuations is a broadening in the photoluminescence emission spectrum. This broadening is often accompanied by the appearance of additional peaks in the spectrum. Our own results in this respect are consistent with what has been reported. Not all of our samples exhibited broad emission peaks. This leads one to
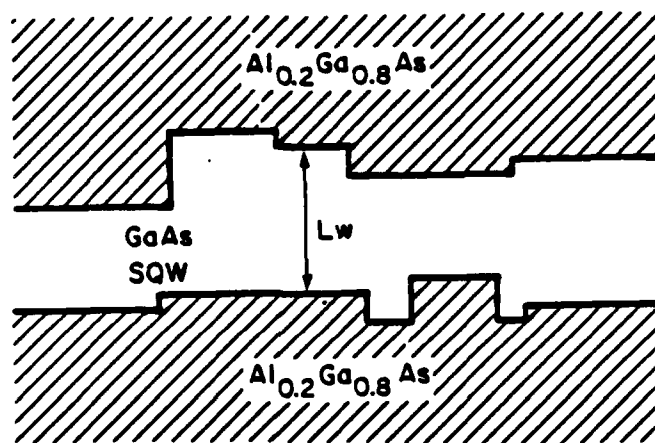
Figure 2.17: A postulated nonuniformity in the width of a single quantum well structure.

believe that the results of Fig. 2.16 are probably for a "worst case sample".

It was stated earlier that the technique of photoluminescence is used to assess optical quality. In Table 2.2, we summarize the photoluminescence results of some of our structures.

Table 2.2: Photoluminescence Results

Buffer	Structure	Intensity T=298 K	FWHM T=298 K	FWHM T=77 K	Doped
SLB	SQW	$10I_0$	46 meV	15 meV	Yes
SLB	MQW	$42I_0$	23 meV	7.8 meV	Yes
GaAs	MQW	$8I_0$	19.8 meV	6.7 meV	No
GaAs	Bulk GaAs	I_0	27.9 meV	9.2 meV	No

As a qualitative measure of intensity, we have used the room temperature luminescence intensity of bulk GaAs as a reference standard. As can be seen, the MQW structure with a superlattice buffer layer represents the "best" sample in terms of the relative intensity and spectral emission width. This type of structure is the one out of which the lasers used in this work are fabricated. The details of the synthesis of these structures are covered in the Technological Appendix.

Chapter 3

Laser Gain and Threshold Current

In the preceding chapter it was experimentally demonstrated that quantum well heterostructures exhibit more efficient luminescence intensities than bulk crystal heterostructures. In this chapter we show theoretically that incorporation of these structures in the active regions of laser devices leads to lasers with very low threshold current densities.

3.1 Graded Index Waveguide Structures

In the basic p-n junction laser structure, the two measurable parameters that characterize the quality of the device are the threshold current density and the external quantum efficiency. These parameters can be optimized by a modification of the basic structure to include other layers that enhance the optical and the carrier confinement properties of the device as a whole, thus increasing the efficiency and lowering the threshold current density.

The active region of the basic structure investigated in this work consists of either a single quantum well or a system of multiple quantum wells. As discussed in the proceding chapter, optical transitions in quantum wells

occur between discrete conduction and valence sub-band energy states. The
presence of a quantum well in the active region, therefore, allows one to
tailor the dominant wavelength (energy) of emission by appropriately ad-
justing the well width and depth. The density of the electronic states that
are involved in the discrete transitions can be increased by several times
that available in a bulk material. We saw earlier that the joint density of
states in a single quantum was given by

$$D_{vc}(E) = \left(\frac{m_h m_e}{m_h + m_e}\right) \frac{1}{\pi \hbar^2 L_w} \sum_n u_{-1}(E - \Delta E_n) \qquad (3.1)$$

One of the reasons why laser devices with quantum well structures in their
active regions have lower threshold current densities than their bulk coun-
terparts is because of the higher joint density of states available in quan-
tum well structures. This will become clear when we discuss the inter-
relationships of the gain, density of states and current in a later section.
We already saw in Chapter 2 that this high density of states also leads to
a high photoluminescent efficiency.

The device active region, which is composed of the quantum wells, is
surrounded by confining graded (Al,Ga)As layers. These confining layers
feature parabolically graded energy slopes down which the electronically
injected carriers slide before tumbling into the quantum well(s). Such a
structure was first proposed theoretically by Kazarinov *et al.* [32]. Because
of the simultaneous variability of the band gap and the index of refrac-
tion in this structure, efficient carrier confinement in the active region can
be achieved; optical confinement of the propagating mode in the direction
transverse to the p-n junction is also simultaneously achieved. The illus-
tration in Fig. 3.1 shows the schematic of the generic device structure
investigated and the inter-relationships of the other parameters designed

into it. In this illustration, we have only shown a structure with a single quantum well. Most of our experimental results, however, were obtained from multiple quantum well structures. The details of the typical structure used are shown in Fig. 3.2. Since the basic physics of multiple quantum well structures is similar to that of a single quantum well, we shall only discuss in detail, a single quantum well.

Another desirable feature of quantum wells and the graded band gap confining layers surrounding them is the formation of a barrier that prevents carrier motion out of the active region once they have been injected into that region. A good fraction of the carriers, thus tightly confined, recombine radiatively in the active volume leading to lower threshold current densities than in conventional double heterostructure lasers. The parabolic index variation in the direction perpendicular to the p-n junction forms a transverse optical waveguide which confines the optical mode very close to the active volume. This particular form of the waveguide structure was chosen because when the transverse wave equation is solved with the parabolic index profile in it, the allowed solutions are Hermite Gaussian functions with the fundamental solution having a minimum full width at half maximum intensity. If the thickness of the confining layer is judiciously chosen, only the fundamental Gaussian mode will be excited.

All these features taken together, contribute toward minimizing the threshold current density and maximizing the differential external quantum efficiency.

It is worth noting that the cladding layers adjacent to the waveguide layers in the devices studied here are composed of 50 % Al. This composition of the ternary compound has a wider band gap than the cladding layers traditionally used in double heterostructure lasers. Our purpose here was twofold. First, by having these $Al_{0.5}Ga_{0.5}As$ layers which have indirect
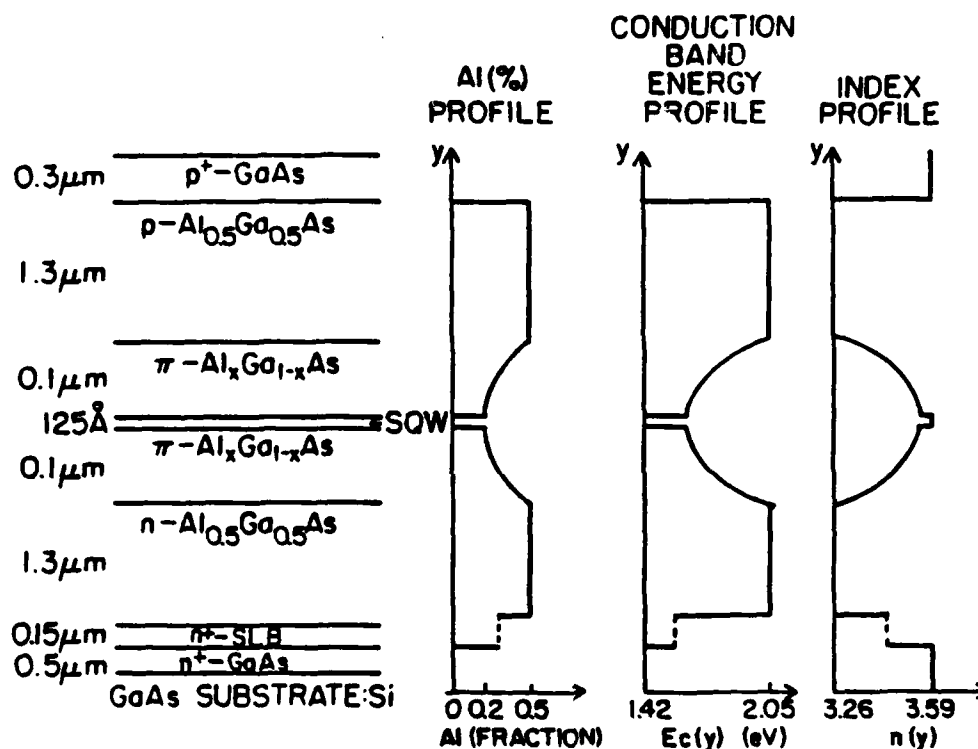
Figure 3.1: The structural composition of a quantum well laser, including the inter-relationships of the important parameters.
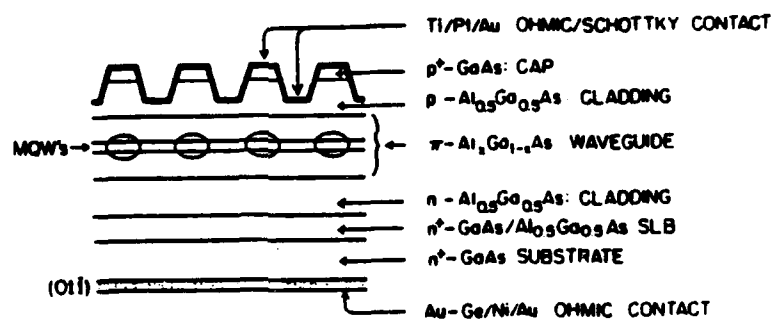
Figure 3.2: The composition of a multiple quantum well laser structure.

optical transitions, we decrease the probability of radiative recombination outside the waveguide region. Secondly, the high band gap material has a correspondingly low index of refraction. This has implications for the waveguiding properties of the graded index region. It means that the optical mode is tightly confined to propagate in the graded region only. The wide band gap material has another useful property which is not germane to the issues discussed here. This property is utilized in the formation of the Schottky barrier scheme used in confining the current to the longitudinal guides. We discuss this further in Appendix B.

3.2   Optical Gain in Quantum Well Lasers

The effects of carrier confinement in quantum well heterostructures and the attendant energy quantization that goes with it have enabled us to prepare lasers with very low threshold current densities (200 A/cm^2) and narrow gain spectra. Other useful characteristics that have been reported in the literature include: polarization-dependent gain [33] and less threshold current sensitivity to temperature [34].

In this section, we wish to discuss the factors that influence the threshold current density in quantum well lasers. The general empirical observation is that these lasers have much lower threshold current densities than regular double heterostructure lasers. Various methods of calculating the optical gain in these structures have been reported [35,36,37]. These methods, however, use the traditional dipole matrix element utilized in lasers with bulk material in the active region [38]. This dipole matrix element is incorporated in the gain expression which is then used in the threshold current relationship. Although this method is correct in principle, the use of the bulk matrix element underestimates the probabilty of transition. Because

of the energy quantization in the well, the allowed $\vec{k}$ vectors in the direction of quantization are discrete. Therefore, the averaging of the dipole moment over k-space is performed in an entirely different way. This in turn leads to a different effective dipole matrix element. Asada *et al.* [39] have recently performed a gain calculation in which they recognize this fact.

3.2.1   The Dipole Moment

In a semiconductor, the probability of a downward transition from the conduction band to the valence band is proportional to the absolute square of the momentum matrix element. For a quantum well, the momentum matrix element may be defined as

$$M_{qw} = \langle \Psi^*_{cnk_z}(r) \mid \vec{p} \mid \Psi_{vmk_h}(r) \rangle \tag{3.2}$$

where the functions $\Psi_{cnk_z}(r)$ and $\Psi_{vmk_h}(r)$ represent the final and the initial eigen-states of the carriers involved in the transition. The momentum, $\vec{p}$, is utilized in its quantum mechanical operator form. For quantum well structures, the function $\Psi_{cnk_z}(r)$ is given as

$$\Psi_{cnk_z}(r) = \Phi_{cn}(y)u_c(y)\exp(jk_z\vec{r}) \tag{3.3}$$

$\Phi_{cn}(y)$ is an envelope function that describes the effect of carrier confinement in the quantum well. This class of functions was introduced in Chapter 2. $u_c(r)$ is the cell-periodic part of the Bloch function of bulk crystals as long as the thickness of the quantum well is many elementary cells wide. The subscripts c (or v) and $n=1,2, 3.....$ denote the conduction (or valence) band and the number of quantized sub-band level in the well, respectively. k_z and r represent the electron wave vector and the position vector, respectively. From Eq.(3.3), the matrix element formed by an electron in

sub-band n and a hole in sub-band m, is given by

$$M_{qw} = \left[\int_{-\infty}^{+\infty} \Phi_{cn}^*(y)\Phi_{cm}(y)dy \right] M_o \qquad (3.4)$$

where

$$M_o = \int_{unit\ cell} u_c^*(r)\vec{p}u_v(r)dr \qquad (3.5)$$

The integral in the brackets is very close to δ_{nm} ($n = m$) because of the symmetry of the potential wells in the conduction and valence bands. The deviation from unity is caused by the different effective carrier masses and also because of the differences between the conduction and valence band discontinuities (0.62/0.38). The second integral over the unit cell must be calculated using the k.p method developed by Dresselhaus [40] and Kane [41]. The functions $u_c(r)$ and $u_v(r)$ are expressed in terms of the atomic s- and p-functions which have the properties of the tetrahedral group under symmetry operations. Following Kane [42], we represent the s-like function with S and the p-like functions with X, Y and Z. In forming the basis functions to obtain a diagonal Hamiltonian, we must remember that because of the energy quantization, the $\vec{k}$ vector used in the computation of the Hamiltonian is inclined at an angle of θ to the cartesian coordinate y-axis as shown in Fig. 3.3. This brings about a complication in that the basis functions have to be rotated. When this rotation is performed, the correct basis functions for the unit cell in a region close to the Brillouin center (small k) are:

$$|S\rangle |\uparrow\rangle \qquad or \qquad |\downarrow\rangle \qquad (3.6)$$

for the conduction band and for the heavy hole valence band this function is

$$\frac{1}{\sqrt{2}}[\mathcal{X} - \mathcal{Y} + \mathcal{Z}]\,|\!\uparrow\rangle \qquad or \qquad |\!\downarrow\rangle \tag{3.7}$$

where

$$\mathcal{X} = (\cos\theta\sin\phi \pm j\cos\phi)\,|\,X\rangle \tag{3.8}$$

$$\mathcal{Y} = \sin\theta\,|\,Y\rangle \tag{3.9}$$

$$\mathcal{Z} = (\cos\theta\cos\phi \mp j\sin\phi)\,|\,Z\rangle \tag{3.10}$$

The angles θ and ϕ represent the directions of the electron k vector in polar coordinates. $|\!\uparrow\rangle$ and $|\!\downarrow\rangle$ are the spin functions of the electron. We shall ignore the wavefunction for the light hole on the ground that the contribution of the light holes to the matrix element is small. The rotation is performed in a manner analogous to that suggested by Kane [42].

In performing the matrix element calculation, we use the experimental fact that the radiation and hence the gain of a quantum well laser is polarization-dependent [33]. The emitted light can be resolved into TE and TM polarizations. In the context of Fig. 3.3, this means that the electric field is parallel to the x-direction in the TE case and parallel to the y-direction in the TM case. The momentum operator components that lead into these polarizations are the p_x- and p_y-components. Therefore, from Eq. (3.6) and Eq. (3.7)

$$M_o = \langle S\,|\,p_x + p_y\,|\,\frac{1}{\sqrt{2}}(\mathcal{X} - \mathcal{Y} + \mathcal{Z}) \tag{3.11}$$

where $\mathcal{X}$, $\mathcal{Y}$ and $\mathcal{Z}$ are as defined previously. With the aid of symmetry arguments for the p-like functions, we evaluate the squared momentum
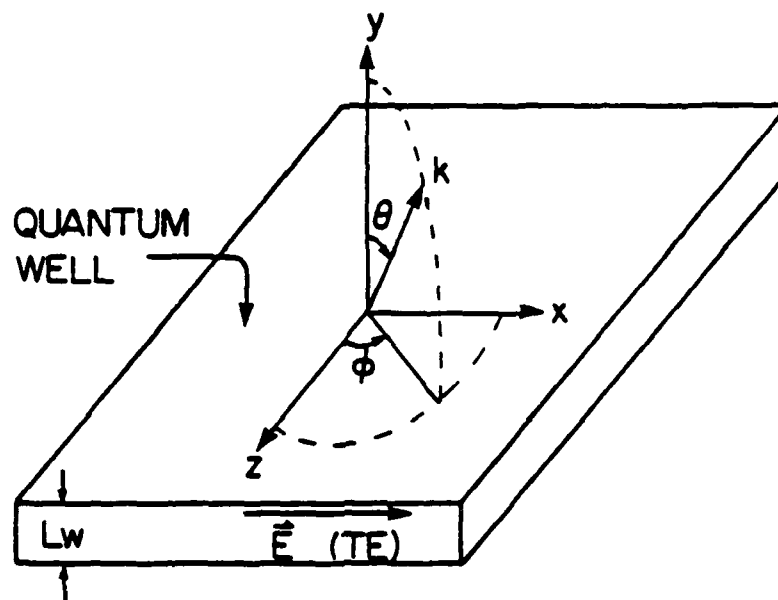
Figure 3.3: The geometrical representation of a quantum well structure and the relationship of the k vector to the TE field.

matrix elements of Eq. (3.11). When averaged over the angle ϕ, these matrix elements evaluate to

$$M_o^2 = \frac{3}{4}M_b^2(1 + \cos^2\theta) \qquad for \quad TE \quad modes \qquad (3.12)$$

and

$$M_o^2 = \frac{3}{2}M_b^2\sin^2\theta \qquad for \quad TM \quad modes \qquad (3.13)$$

A factor of 1/2 is included in these expressions to account for electron spin. The parameter M_b^2 is the conventional matrix element for III-V bulk materials and from Kane's [42] analysis, it is given by [38]

$$M_b^2 = \frac{m_o^2 E_g}{12m_e}\left(\frac{E_g + \Delta}{E_g + (2/3)\Delta}\right) \qquad (3.14)$$

where m_o is the free electron mass, m_e is the electron mass in the particular III-V semiconductor under consideration, E_g and Δ are, respectively, the energy gap and the spin-orbit splitting. If we use GaAs parameters in Eq. (3.14), the value of $M_b^2 \simeq 1.33 m_o E_g$.

The components of the electron k-vector are related to the angle θ and the energy of the electron in the conduction band quantum well by the expression

$$\cos^2\theta = \frac{k_{ny}^2}{k^2} = \frac{E_n}{(\hbar^2 k_{||}^2/2m_e) + E_n} = \frac{E_n}{E_{tn}} \qquad (3.15)$$

where E_n is the n-th quantized eigen-energy in the y-direction and E_{tn} is the total energy of the electron in the n-th sub-band. $(\hbar^2 k_{||}^2)/(2m_e)$ is the electron energy parallel to the quantum well.

We are now in a position to give the momentum matrix element in a quantum well. This quantity, expressed as a multiple of the dipole matrix

element in a bulk material, is given by combining our results from Eqs. (3.4), (3.12), (3.13) and (3.15):

$$M_{qw}^2 = \frac{3}{4}M_b^2(1 + E_n/E_{tn}) \qquad for \quad TE \quad modes \qquad (3.16)$$

Close to a sub-band edge, most of the energy of the confined carrier is due to the confinement effect and the parallel component is very small; in this case one can approximate Eq. (3.16) by

$$M_{qw}^2 \simeq \frac{3}{2}M_b^2 \qquad for \quad TE \quad modes \qquad (3.17)$$

In the light of the experimental evidence that the gain in quantum well lasers [33,43] is polarization dependent and that the field emission is predominantly of the TE kind, we shall, henceforth, concern ourselves only with the TE field. The mechanics of the analysis for the TM field are, *mutatis mutandis*, the same.

3.2.2   Band-to-Band Transitions with k-Conservation

In this model, it is assumed that when an electron makes a transition, say from an initial energy state E_i in the conduction band to a final energy state E_j in the valence band, this transition is made with *no* change in momentum ($p = \hbar k$). The energy of the electron in the conduction and the valence band is then given, respectively, by

$$E_i = E_c + \frac{\hbar^2 k^2}{2m_e} \qquad (3.18)$$

$$E_j = E_v - \frac{\hbar^2 k^2}{2m_h} \qquad (3.19)$$

where E_c and E_v are the band edges; k is the vector representing the conservation of momentum. The zero of energy is at the edge of each band

such that energy is measured positive up into the conduction band and positive downward into the valence band.

The conservation of k-vector implies that Eqs. (3.18) and (3.19) can be rewritten as

$$E_i = E_c + \left[\frac{m_h}{m_h + m_e}\right](E - E_g) \tag{3.20}$$

$$E_j = E_v - \left[\frac{m_e}{m_e + m_h}\right](E - E_g) \tag{3.21}$$

where E is the photon energy of the transition and E_g is the "band gap".

The expression for the optical gain in a semiconductor has been given by Lasher and Stern in their classic paper [44] as

$$g(E) = \left[\frac{\pi q^2 \hbar \langle M \rangle^2}{\epsilon_o m_o^2 cnE}\right] D_{vc}(E)[f_u(E) - f_l(E)] \tag{3.22}$$

where $D_{vc}(E)$ is the joint density of electronic states, $f_u(E)$ and $f_l(E)$ are the Fermi occupation probabilities of the upper and lower states. This expression is written for the case of k-conservation and it is in MKS units. The original expression was written in cgs units.

For a quantum well, the joint density of states was derived in Chapter 2 and given by Eq. (3.1). The matrix element $\langle M \rangle^2$, must be replaced by the expression given in Eqn. (3.17). The Fermi functions $f_u(E)$ and $f_l(E)$ are given by

$$f_u(E) = \left[1 + \exp\{\frac{m_h}{m_h + m_e}(\frac{E - (E_g + E_{cn} + E_{vc})}{kT}) - \frac{F_c}{kT}\}\right]^{-1} \tag{3.23}$$

$$f_l(E) = 1 - \left[1 + \exp\{\frac{-m_e}{m_e + m_h}(\frac{E - (E_g + E_{cn} + E_{vn})}{kT}) - \frac{F_v}{kT}\}\right]^{-1} \tag{3.24}$$

where F_c and F_v are the quasi-Fermi levels in the conduction and valence bands, respectively. The parameters E_{cn} and E_{vn} are the quantized eigen-energies of the respective sub-bands as discussed earlier. In writing these equations, use has been made of the expressions given in Eqs. (3.20) and (3.21).

The quasi-Fermi levels, F_c and F_v, are related to the injected carrier densities through the expressions

$$N = \int \rho_c(E) f_c(E) dE \qquad (3.25)$$

$$P = \int \rho_v(E) f_v(E) dE \qquad (3.26)$$

where $\rho_c(E)$ and $\rho_v(E)$ are the densities of the states in the conduction and valence bands. These functions are not to be confused with the *joint* density of states function given in Eq. (3.1). In the conduction band for example,

$$\rho_c(E) = \frac{m_e}{\pi \hbar^2 L_w} \sum_n u_{-1}(E - \Delta E_n) \qquad (3.27)$$

A similar expression can be written down for $\rho_v(E)$. The functions $f_c(E)$ and $f_v(E)$ are the ordinary Fermi functions. The quasi-Fermi levels F_c and F_v are best determined by numerically solving Eqs. (3.25) and (3.26). Fig. 3.4 illustrates a typical curve for a 12.5 nm quantum well. From a curve such as this, one can determine the quasi-Fermi level for electrons for a given injection level.

With the foregoing considerations for quantum well structures, the relevant modified gain expression is given by

$$g(E) = \sum_{n=1}^{m} \left[\frac{q^2 \langle M_{qw} \rangle^2}{\epsilon_o m_o^2 c n \hbar E L_w} \right] \left[\frac{m_e m_h}{m_e + m_h} \right] [f_u(E) - f_l(E)] \qquad (3.28)$$

The numerical evaluation of this equation involves a modest amount of computation which is best done on a computer. An algorithm, which has been implemented into a computer code, has been developed. The basic idea of the algorithm is to rapidly determine the optical gain for given injection levels. If this information is given in the form of a current density, it is first converted to a carrier density which is then used to compute the quasi-Fermi levels. The quasi-Fermi levels, which represent the injected carrier densities, enter the gain expression via Eqs. (3.23) and (3.24).

As an example, we illustrate in Fig. 3.5 the gain spectra of two different well sizes at the same injected carrier density of 2×10^{18} cm^{-3}. In this particular calculation, we have assumed that the main lasing transition is due to the lowest confined particle states in the conduction and the valence bands. This assumption is based on the experimental evidence discussed in Chapter 2 on the photoluminescence emission of quantum well structures. It was demonstrated there and confirmed by calculation that the main photoluminescence emission from quantum well structures is primarily due to the electron $\rightarrow$ heavy hole ($1e \rightarrow hh$) ground state transition. The electron $\rightarrow$ light hole ($1e \rightarrow lh$) transition will be neglected here because the density of states of the light holes is much lower in comparison to that of the heavy hole sub-bands. The pholuminescence emission due to this band was also shown to be relatively low in Chapter 2. The well sizes in question are L_w=12.5 nm and 20.0 nm. We note that the gain is zero below a certain energy corresponding to the "gap" of the first sub-band for each well size; it vanishes again for photon energies larger than $F_c - F_v$, which satisfies the Bernard-Duraffourg condition [45]. The higher
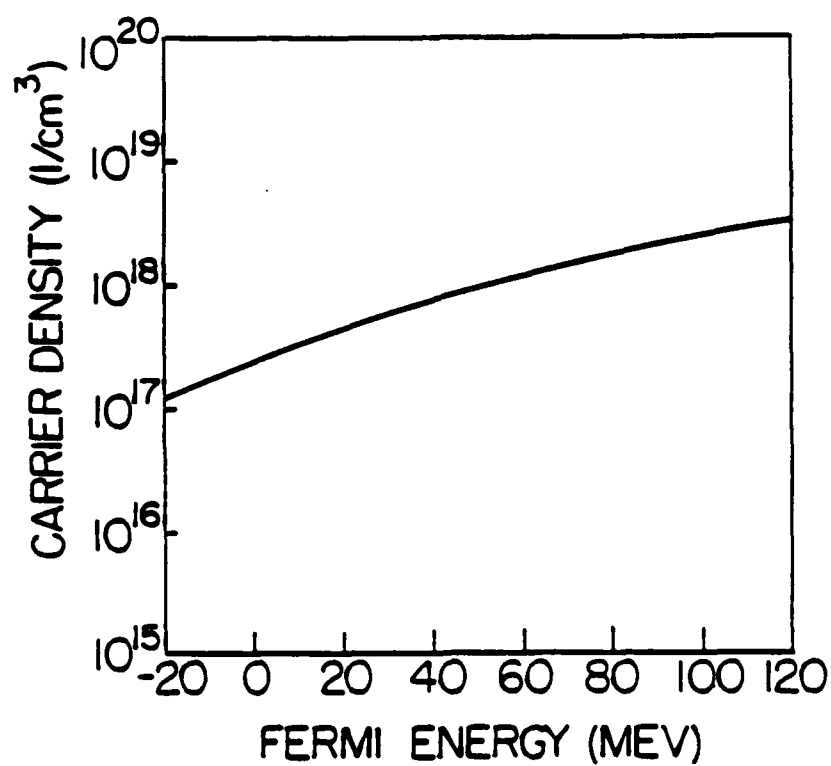
Figure 3.4: A curve relating the electron quasi-Fermi level to the number of injected carriers in a 12.5 nm-quantum well structure.

gain of the narrower quantum well can be understood in terms of the high density of optical states available in narrow size wells (see Eqs. (3.1) and (3.27)). In general, the optical gain of a quantum well structure, for a given carrier injection level, will increase with decreasing well size until a point is (L_w <5 nm) reached where the separation between the electron or hole energy and the corresponding quasi-Fermi level begins to decrease such that the Fermi inversion factor $(f_u(E) - f_l(E))$, in the gain equation becomes small. Beyond this point, despite the increase of the density of states with decreasing L_w, the gain will decrease. In terms of the current density, this means that it will decrease to a minimum for a given well size and injection level and begin to rise again for well sizes smaller than the critical minimum. This theoretical prediction is in agreement with reported experimental observations [46].

3.3 Threshold Current Density Calculations

The threshold gain, g_{th}, for a given laser diode with an optical confinement factor, Γ, is the gain required to overcome all the losses in the active cavity before the onset of lasing. This quantity is related to the other parameters in the laser cavity by the well known expression [47]

$$g_{th} = (1/\Gamma)\left[\alpha_i + (1/L)\ln(1/R)\right] \qquad (3.29)$$

where α_i is the total internal losses mostly due to free carrier absorption and diffraction losses. The parameter L is the cavity length and R is the facet relectivity. We take for values, $\alpha_i = 12$ cm^{-1} (the free carrier absorption part of α_i is estimated from the formula for free carrier absorption). L is chosen to be $\simeq 350\mu$m, a typical value for the broad area lasers studied in this work. The reflectivity is estimated from Fr   ''s formula which relates
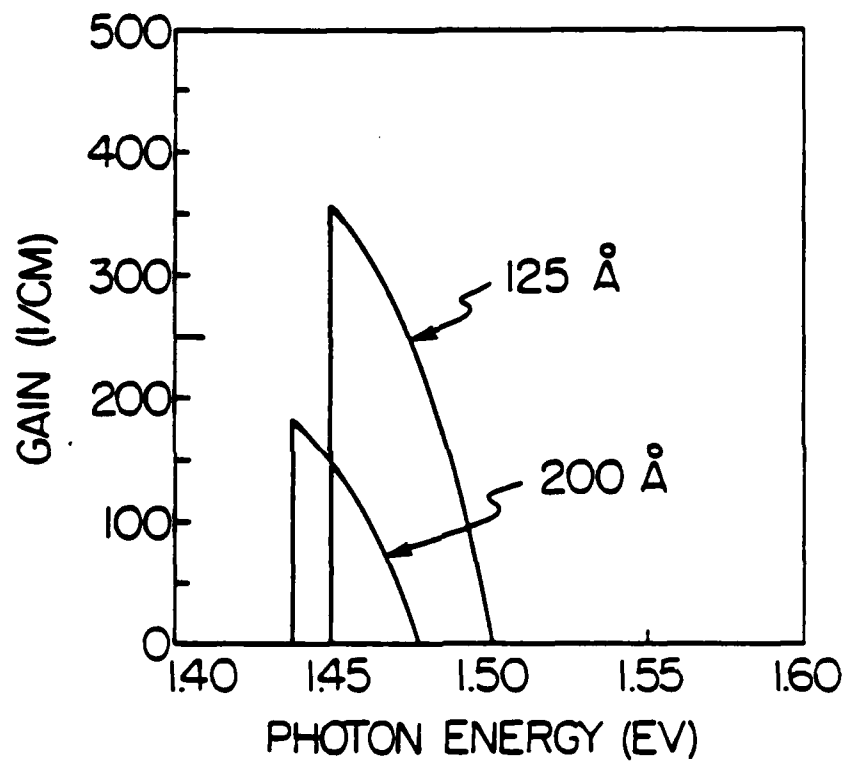
Figure 3.5: The optical gain spectra of two different quantum well sizes at an injected carrier density of 2×10^{18} cm^{-3}.

the index of refraction n to the reflectivity, R. Thus for $n \simeq 3.6$, we have

$$R = \frac{(n-1)^2}{(n+1)^2} \simeq 0.32 \qquad (3.30)$$

The confinement factor, Γ, is given by the approximate relationship $\Gamma \simeq L_w/2w_0$. See Appendix A for the derivation of this formula. L_w is the quantum well width. In this case $L_w = 12.5$ nm. The parameter w_0 is the gaussian beam radius for the fundamental field solution to the transverse wave equation. The dimension w_o is estimated by using Eq. (A.2) in Appendix A to determine the confocal parameter which is then used in the calculation of w_0. For a single quantum well structure surrounded by a 200 nm graded barrier waveguide, $w_0 \simeq 164.7$ nm, $\Gamma \simeq 0.038$. With these numerical values, we obtain through use of Eq. (3.29) that $g_{th} \simeq 1170\,\mathrm{cm}^{-1}$. The carrier density that is necessary to achieve this gain is computed by the algorithm discussed earlier.

The threshold current density, J_{th}, is written as

$$J_{th} = \frac{qL_w N_w N_{th}}{\tau_{sp}} \qquad (3.31)$$

where q is the electronic charge, L_w is the well size, N_w is the number of wells, N_{th} is the computed carrier density corresponding to g_{th} and τ_{sp} is the spontaneous radiative carrier life time. This life time has recently been measured in quantum well structures to be $\sim 2.8 \times 10^{-9}$ seconds [48]. For a single quantum well, with the parameters given here, the threshold current density is calculated to be $\simeq 450$ A cm^{-2}. The best measured threshold current density of our SQW devices was about 650 A cm^{-2}. We have also measured values as high as 1.0 kA cm^{-2} and worse. Tsang [49] has reported experimental threshold current densities of 810 A cm^{-2} for 20.0 nm-wide single quantum well lasers. And threshold current densities of $\sim$410 A

cm^{-2} have also been reported in the literature [50] for SQW lasers. The agreement between the theoretical value and our best experimental result is fair. Our results are also consistent with what has been reported in the literature.

In the calculation of the threshold current density for a multiple quantum well (MQW) laser structure, the effect of the other wells on the confinement factor must be considered. We have calculated the threshold current density for a MQW device with the following structure in the acitve layer: 5 quantum wells, each 12.5 nm wide, separated by 25.0 nm barriers. The MQW region is surrounded by a waveguide whose thickness is 200.0 nm. the effective thickness of the quantum wells is $L_{eff} = 5L_w$. In the same spirit, the beam radius, $w_{eff} \sim 187.3$ nm. These modified dimensions lead to an increased confinement factor, $\Gamma \simeq 0.170$. Assuming that the losses remain the same as in the SQW case, we obtain, for the same cavity length and reflectivity as before, a threshold gain, $g_{th} \simeq 258.4$ cm^{-1}. Further calculations show that the corresponding threshold current density, $J_{th} \simeq 500$ A cm^{-2}. The average experimentally determined value for our best MQW devices was about 200 A cm^{-2}. The agreement between theory and experiment, again is fair. We caution, however, that the value for the confinement factor used in this case may actually be smaller than what it should be, in which case the agreement should even be better for more accurate Γ values. This issue arises because the approximation used in the derivation (see Appendix A) of the confinement factor is really for a SQW device where the contribution of the well to the index profile is neglected. For the MQW case, the approximation of the MQW and barrier contribution to the index may not be accurately reflected. In this particular case, the profile has been averaged in this region.

We recall here also that the gain model in this calculation does not

include the TM contribution. It is expected that the calculated values will agree very closely with the experimental values when this component is included. These results should therefore be viewed as first order calculations within the approximations made.

3.4 Gain Broadening Mechanisms

It is customary when discussing laser gain, to include in the discussion some mention of the mechanisms that prevent ideal behavior above threshold. In this thesis, however, since no spectral measurements as a function of pumping intensity were conducted, the discussion here will be limited to a comment-in-passing.

The gain model discussed in this work for the calculation of the threshold current density incorporates only the most essential features necessary in the calculation. Mention was not made of the other processes that might affect the gain spectrum at the onset of lasing. This is partly because, in retrospect, the simple model is adequate in explaining the results of our measurements. The other reason is that theoretical difficulties still remain in a complete quantitative understanding of these mechanisms. The mechanisms we speak of are the many-body effects of scattering for example, by carrier-carrier, carrier-lattice interactions. These mechanisms are intimately linked to the transportation phenomena in semiconductors. What one is then faced with is a problem of having to treat both particle transport and optical transition in the injection laser by having to define the position, r, and the wave vector k of a carrier at the same time. The simultaneous definition of the position and the wave vector of a carrier is, in general, very difficult. It raises the philosophical difficulties discussed, for example, by Heisenberg [51].

It is generally thought that semiconductor lasers are homogeneously broadened [52,53]. This means that all injected carriers have an equal opportunity to participate in the lasing emission of photons with energy E_m. Because of rapid scattering rates, the carriers are assumed to be indistinguishable and thus the inverted population depletion and the saturation of the gain is "uniformly spread" over the whole energy spectrum of the available carriers. Depending on the interaction kinetics, however, a different state of affairs can exist. Assume for example, that photons with energy E_m are only coupled to states separated by an energy E_m. Then for the gain to saturate uniformly, the rate at which carriers are being consumed from the lasing states by stimulated emission must equal the rate at which carriers are being replenished into those states by intraband scattering. If the consumption rate exceeds the replenishment rate, then a local depletion will be found in the lasing states. This is the origin of the concept of "spectral hole burning". An elegant exposition of it has been rendered by Nishimura [54] using the semiclassical density matrix method.

Because of the many-body effects (scattering) we spoke of earlier, theoretical studies have been conducted to extend the laser gain theory to include these effects [55,56] in the regular double heterostructure laser devices. The lasing energy spectrum is thought to be broadened by scattering. The assumed broadening lineshape is Lorentzian with an energy uncertainty given by $\hbar/\tau_R$ where τ_R is the scattering time or the energy relaxation time. The entire emission line function is then inhomogeneous and it is given by the sum of all the homogeous lines of the individual lasing lines. Quantitatively, this means that Eq.(3.22) is modified in the manner indicated below.

$$g(E) = \sum_{n=1}^{m} \left[\frac{q^2 \langle M_{qw} \rangle^2}{\epsilon_o m_o^2 cn\hbar E L_w} \right] m_r \int_{E_g + E_{c1} + E_{v1}}^{\infty} d\mathcal{E} \left[f_u(\mathcal{E}) - f_l(\mathcal{E} - E) \right] W(k, \mathcal{E})$$

(3.32)

where $\mathcal{E} = E_g + E_{cn} + E_{vn}$,

$$m_r = \frac{m_e m_h}{m_e + m_h}$$

(3.33)

and

$$W(k, \mathcal{E}) = \int d^3k L_c(k, \mathcal{E}) L_v(k, \mathcal{E} - E)$$

(3.34)

The functions $L_c(k, \mathcal{E})$ and $L_v(k, \mathcal{E}_E)$ are the respective spectral weight functions that account for the broadening of the energy levels in the conduction and valence bands. The general spectral weight function is given by

$$L(k, \mathcal{E}) = \frac{1}{\pi} \frac{\gamma_L}{(\mathcal{E} - (\hbar^2 k^2)/2m) + \gamma_L^2}$$

(3.35)

where $\gamma_L = \hbar/\tau_R$ is the width of a broadened discrete individual energy level. The discussion here follows closely the arguments given in Ref. [55]. The treatment here, however, has been specialized to the case of quantum well lasers. In particular, we note that this broadening effect could be significant if the energy $\gamma_L = \hbar/\tau_R$ is on the order of the separation of the eigen energies in the quantum well. The energy level separation between the first and the second eigen states in our typical 12.5 nm well is ~60 meV in the conduction band. This means that if the electron scattering processes are extremely fast, $\sim 1.1 \times 10^{-14}$ seconds, the energy quantization in the quantum well will be washed out. These times, however, are estimated to be larger than this [56].

We propose here that because of the fluctuations inherent in quantum well thicknesses, the quantized eigen-energies may have an additional broadening due to these fluctuations. Consequently, the energy γ_L would have a contribution from these effects.

3.5 SQW versus MQW Laser Structures

From the calculations of Section 3.3 , there does not appear to be any overwhelming theoretical reason for a choice of either a SQW or a MQW laser structure. Both structures are ideally capable of yielding low threshold current densities. The SQW structure, however, requires a much higher threshold gain. This is simply because the confinement factor, Γ, is small for this structure.

The experimental results of the structures studied in this work and elsewhere [57,58], however, favor the MQW structure. The practical difficulties associated with current MBE technology in achieving a uniform thickness in a quantum well, we believe, make it very hard for a single quantum well structure to approximate the ideal conditions necessary for a low threshold current density on a routine basis. In the MQW structures, the first one or two quantum wells deposited may not necessarily be uniform but as the evidence discussed in Chapter 2 on the growth of superlattices suggests, the subsequent wells are more uniform. These are the wells that would closely approximate the ideality of perfection required for the low threshold conditions. And as the photoluminescence results of that chapter also demonstrated, the MQW structures have inherently better emission efficiencies because of the increased density of states available for optical transitions. For these experimental reasons, therefore, the phase-locked laser arrays discussed in this thesis were made out of MQW structures.

Chapter 4

Phase-Locking in Semiconductor Lasers

This chapter provides the theoretical framework within which we shall discuss the lasers fabricated from the structures discussed in the preceding chapters. This background is needed for the next chapter. In what follows we discuss the principles of operation of phase-locked laser arrays. We begin by outlining the basic ideas of wave-guidance in passive guides and then make a connection to how the unguided evanescent waves can be used to induce phase-locking. Following this, we introduce the mixed-mode phase-locked laser array. In this type of array, phase-locking is caused by coupling through diffraction.

4.1 Principles of Phase-Locking

The basic ideas of phase-locking are best understood by considering a simple linear array of ideal radiators (antennas) of electromagnetic energy. We shall consider, as an example, a row of equally spaced emitters. Suppose that each one of the emitters can launch a wave of the same frequency (wavelength). This can be arranged, for example, by devising a method for

78

connecting all the emitters to the same master oscillator. Suppose also that each emitter can produce a random intrinsic phase, $\varphi_n(x,t)$, for each wave it launches. The phase, $\varphi_n(x,t)$, is a function of the spatial coordinate x and time t. Since the individual phases of the emitters are uncorrelated with one another, the emitters are said to be *incoherent*. Such an array of emitters would produce a random interference pattern in space, one which fluctuates rapidly and whose time average is independent of the angle of observation.

If the array of emitters is as shown in Fig. 4.1, the angle of observation θ, is the angle subtended by a line from an emitter to the point O and the normal to the row of emitters. An incoherent array of emitters serves no practical purpose. What would be much more useful is a set of *coherent* emitters. By a *coherent* set of emitters we mean ones that maintain a definite phase relationship with one another. The radiation as observed at the point O, would then have a distinct pattern to it.

Consider for simplicity that we are able to force (by some mechanism whose origin it is not important to know) *all* the emitters to add *no* intrinsic phase to the waves each one of them launches. What we now have is a set of phase-locked emitters. The radiation pattern of such emitters as observed at point O, has some very interesting and desirable features. We discuss these features below.

Let us assume that each radiator emits radiation of frequency ω with phase $\varphi = 0$. Far away from the emitters, at the observation point O, the total electric field amplitude is

$$\vec{E} = \hat{\imath}_x \frac{C}{r} f(w) [e^{j(\omega t - k_n r_o)} + e^{j(\omega t - k_n r_1)} + \cdots + e^{j(\omega t - k_n r_{N-1})}] \qquad (4.1)$$

$$\vec{E} = \hat{\imath}_z \frac{C}{r} f(w) e^{j(\omega t - k_o r_o)} [1 + e^{-j\delta} + e^{-j2\delta} + \cdots + e^{-j(N-1)\delta}] \qquad (4.2)$$

where

$$f(w) = \int_{w/2}^{w/2} e^{-j k_o \sin\theta x} dx \qquad (4.3)$$

C is a complex constant, $k_o = 2\pi/\lambda_o$, is the propagation constant, r is the average distance from a radiator to the point O and $\delta = k_o(r_1 - r_o) = k_o \tilde{s} \sin\theta$ is the phase difference between neighboring emitters as observed at point O. The integral $f(w)$ expresses the spatial Fourier transform of a single emitter in the array. The parameter w is the width of the spatial extent of each emiter. Eq. (4.2) contains a geometric series which can be summed; and if we also perform the indicated integration, we get

$$\vec{E} = \hat{\imath}_z \frac{C}{r} \frac{\sin\{(k_o w/2) \sin\theta\}}{(k_o w/2) \sin\theta} \left[\frac{1 - e^{-jN\delta}}{1 - e^{-j\delta}} \right] e^{j(\omega t - k_o r_o)} \qquad (4.4)$$

The intensity of radiation at O is given by

$$I = \langle \vec{E}.\vec{E}^* \rangle \qquad (4.5)$$

where the angle brackets denote time-averaging over one cycle of oscillation. Performing the operation indicated in Eq. (4.5) gives

$$I = I_0 \left[\frac{\sin\{(k_o w/2) \sin\theta\}}{(k_o w/2) \sin\theta} \right]^2 \left[\frac{1 - \cos(N k_o \tilde{s} \sin\theta)}{1 - \cos(k_o \tilde{s} \sin\theta)} \right] \qquad (4.6)$$

where I_0 is a constant and N is the total number of emitters in the array. We can make some remarkable observations from Eq. (4.6).[1] First, we notice that the second term of Eq. (4.6) after the constant I_0 is the expression for

---

[1] The theoretical discussion here parallels the treatment that is generally used in discussing the diffraction grating. The relevant details of the arguments can be found in any good optics text (e.g. Born and Wolf).
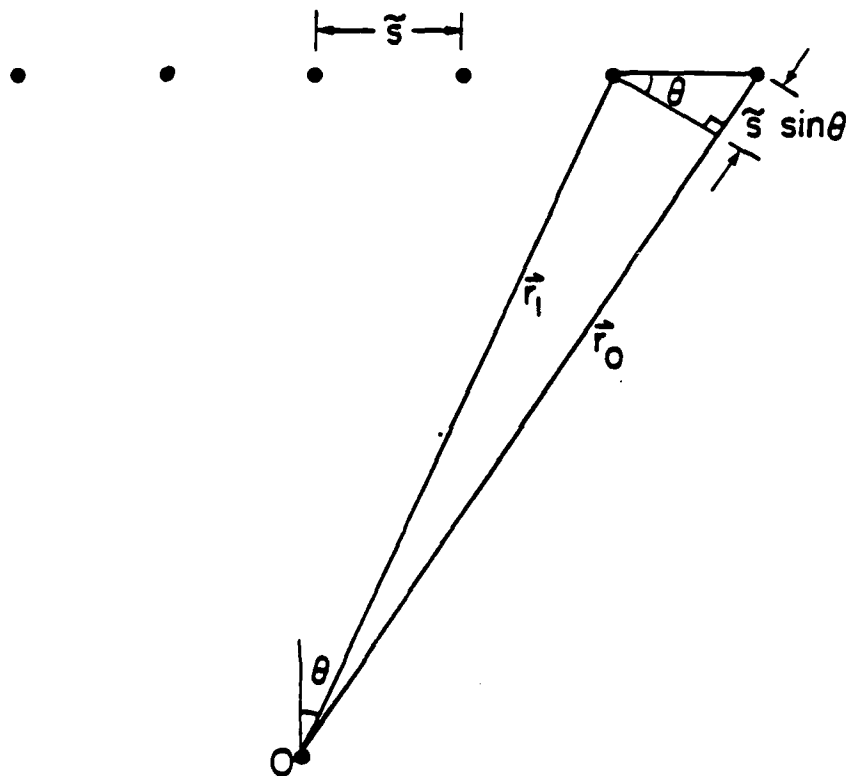
Figure 4.1: An array of ideal electromagnetic radiators.
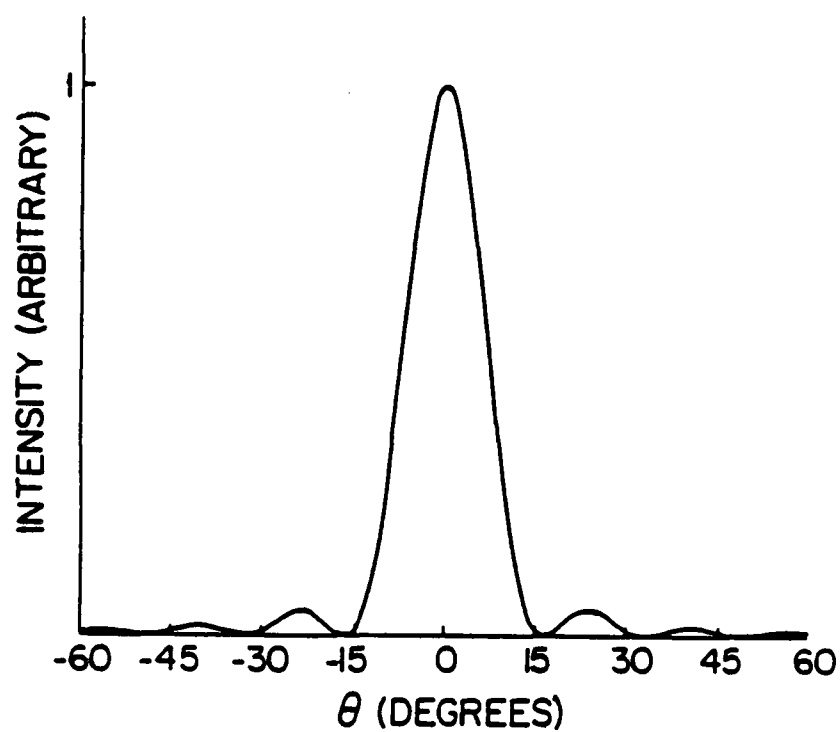
Figure 4.2: Far-field radiation characteristic of one ideal emitter.
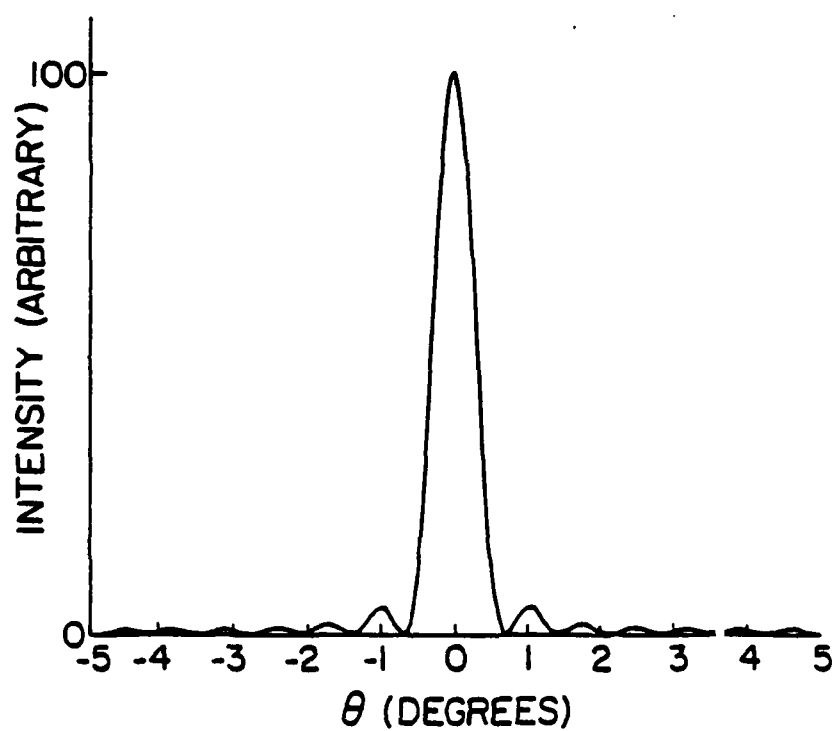
Figure 4.3: Far-field radiation pattern of ten coherent ideal radiators.

diffraction from a single aperture. The third term is the expression due to the interference effects between the apertures of the emitters in the array.

In order to appreciate the effect and advantage of an array of coherent emitters, we illustrate the far-field intensity patterns for two cases in Figs. 4.2 and 4.3. In the first case, we only have one emitter ($N=1$). The expression for the far-field intensity pattern reduces, in this case, to

$$I = I_0 \left[\frac{\sin\{(k_o w/2)\sin\theta\}}{(k_o w/2)\sin\theta} \right]^2 \tag{4.7}$$

The parameter values used in Fig. 4.2 are $\lambda_o = 0.86$ μm, $w = 3$ μm. In the second case, there are ten ($N = 10$) emittters in the array with a center-to-center spacing of $\tilde{s}=7$ μm. The far-field intensity pattern shown in Fig. 4.3 is two orders of magnitude (N^2) stronger than that from the single emitter; this pattern is also narrower than the previous one. The importance of a coherently operating set of linear radiators lies in the fact that for a large number of them, the radiation emitted can be concentrated into a very narrow, intense lobe. This has practical applications. If the radiators are radar antennas, it gives one the ability to scan the lobe spatially by introducing a phase factor. What is important to note here is that the concepts of coherence and phase-locking discussed above can be extended to semiconductor lasers. After all, lasers are generators of electromagnetic radiation at optical frequencies.

The notion of phase-locking in semiconductor lasers can be implemented if, by some means, one can contrive to place individual lasing elements within a close proximity of one another. An individual semiconductor laser by itself generates coherent radiation. However, because of inhomogeneities in the lasing medium and irregularities in the photon generation process across the entire medium, it may not be possible that an array of lasing

elements will always be *collectively* coherent. Therefore, some means of forcing *collective* coherence has to be implemented so that all the elements of the array have the same relative phase.

The method of inducing phase-locking that we use in this work involves coupling a fraction of the radiation propagating in one guide to another adjacent to it and vice-versa. This is done across the entire array of elements. When the conditions are right, the individual elements will all operate with the same phase. The method of evanscent wave coupling is the simplest technique of phase-locking adjacent laser elements. This technique depends critically on the ability to delineate waveguides on the laser structure. Therefore, wave guidance is important in the array elements. We discuss waveguiding in the phase-locked lasers fabricated for this thesis in the next section.

4.2   Wave Guidance in Phase-Locked Lasers

The laser arrays we fabricated featured both lateral and transverse mode confinement. The transverse electromagnetic mode confinement is automatically built into the laser structure by the several hetero-epitaxial layers that constitute a wave guide in that direction. In Fig. 4.4, we have abstracted a simple model of the laser array. In this model, we have only retained the epitaxial layers that are necessary for the guidance of an optical mode in the structure. The structure in Fig. 4.4a shows the n-type $Al_xGa_{1-x}As$ and the top p-type $Al_xGa_{1-x}As$ cladding layers. Sandwiched between them is a single quantum well active layer surrounded by a parabolically graded $Al_xGa_{1-x}As$ waveguide. Fig. 4.4b shows two of the ridge waveguides necessary for lateral confinement of the modes. The ridge of index n_c is surrounded by a medium of index n_o (in this case air). For this

analysis, we shall assume (temporarily) that the waveguides are passive. This assumption allows us to choose the guided modes of such a structure to be essentially of the TE or TM kind with two families: E_{mn}^z and E_{mn}^y, where m and n are the mode label indices.

Before proceeding with the analysis, we extract further, another model from Fig. 4.4. This new model of the ridge waveguide is shown in Fig. 4.5. Consider the structure shown in the lower illustration and the suggested equivalent structure viewed from the top above it. This structure is symmetric about the x-axis and can be thought of as an equivalent guide that provides confinement in the x-direction. The effect of the extra ridge thickness t, is to create a region of *effective index N_c*, higher than that of the outer regions, N_g.

In order to avoid confusion later, we will say a few things about the *index of refraction n*, and the *effective index of refraction N*. The indices of refraction of the original ridge waveguide structure are n_c, n_g and n_o. In this case $n_g > n_c$ and $n_g > n_o$. Out of this guide, we derive the equivalent planar guide shown in the top illustration of Fig. 4.5a. This guide has *effective indices of refraction* defined by $N = \beta/k$ through a transcendental dispersion relation which we derive later. The method of analysis we use here is the effective index method [59].

In Fig. 4.5, the effective indices of refraction N_c and N_g are redefined for convenience in regions 1, 2 and 3 of the equivalent guide as follows:

$$n_1 \equiv N_g = n_3 \tag{4.8}$$

$$n_2 \equiv N_c. \tag{4.9}$$

Notice that $n_1 = n_3$ for this particular structure because of the symmetry
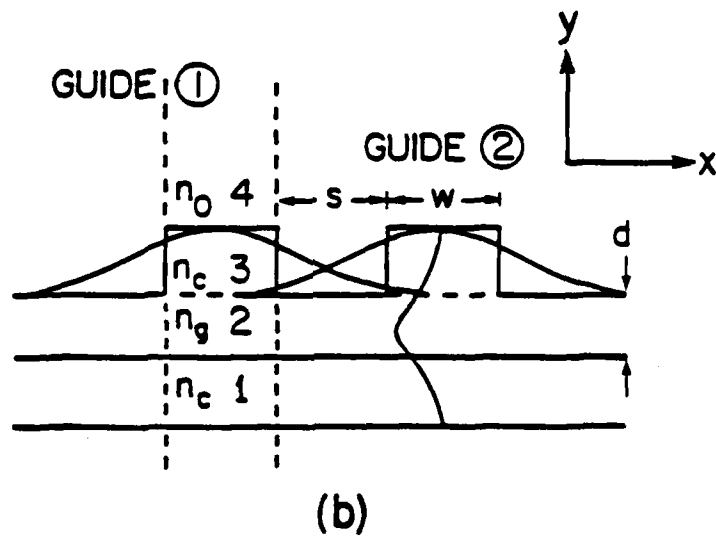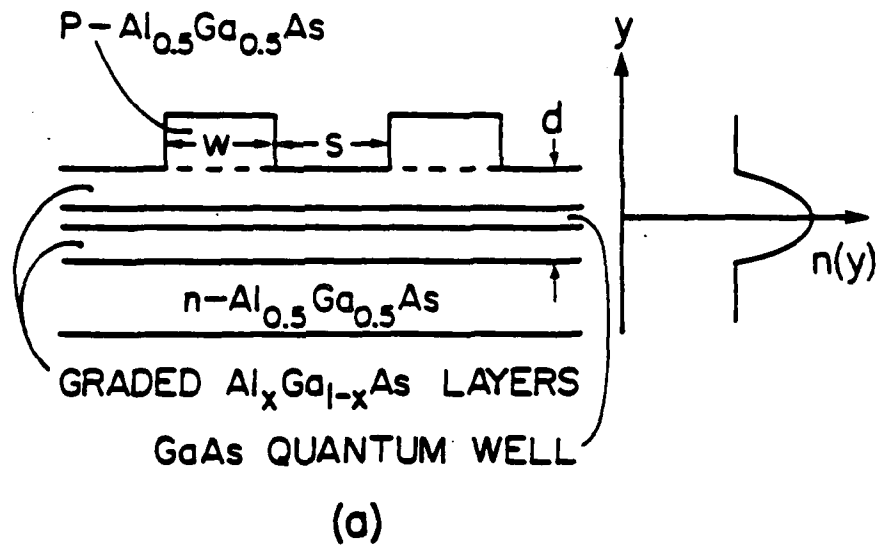
Figure 4.4: The coupled waveguide laser structure for (a) the lateral guides and (b) the transverse guide.
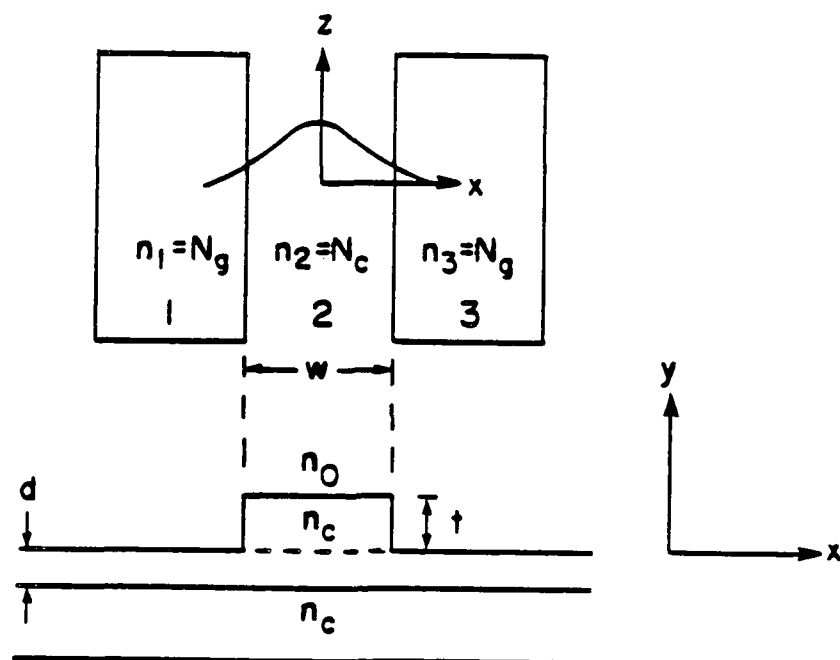
Figure 4.5: The equivalent guide structure abstracted from Fig. 4.4.

inherent in the ridge waveguide about the x-axis.

In what follows, it will be understood that any undefined quantity associated with a field has its usual meaning in electromagnetic field theory. For an assumed E_y field distribution of the form

$$E_y(x, z, t) = \mathcal{E}_y(x)e^{j(\omega t - \beta z)} \tag{4.10}$$

we find from Maxwell's equations that

$$H_z(x, z, t) = \frac{-\beta}{\omega \mu_o} \mathcal{E}_y(x)e^{j(\omega t - \beta z)} \tag{4.11}$$

$$H_z(x, z, t) = \frac{j}{\omega \mu_o} \frac{\partial E_y}{\partial x} \tag{4.12}$$

The lateral field distribution, $\mathcal{E}_y(x)$, can be asssumed to be of the form:

$$\mathcal{E}_y(x) = Ae^{q(x+w/2)} \qquad x \leq w/2 \tag{4.13}$$

$$\mathcal{E}_y(x) = Be^{jhx} + Ce^{-jhx} \qquad |x| \leq w/2 \tag{4.14}$$

$$\mathcal{E}_y(x) = De^{-p(x-w/2)} \qquad x \geq w/2 \tag{4.15}$$

where A, B, C and D are constants to be determined by imposing continuity conditions on the tangential electric and magnetic fields at the guide interfaces. The constants q, h and p are the lateral propagation constants in the different regions of the waveguide.

Application of the continuity conditions to Eqs. (4.13), (4.14), (4.15) and to a similar set derived from (4.12) leads to a system of linear equations whose determinantal equation, when set to zero, immediately yields the eigenvalue equation

$$hw = \tan^{-1}\left(\frac{p}{h}\right) + \tan^{-1}\left(\frac{q}{h}\right) + m\pi, \qquad m = 0, 1, 2, \ldots \qquad (4.16)$$

where m is the lateral mode number. Substitution of the field quantities in Eqs. (4.13), (4.14) and (4.15) into the wave equation results in the additional relationships

$$
\begin{aligned}
q &= \sqrt{\beta^2 - (n_1 k_o)^2} \\[2mm]
h &= \sqrt{(n_2 k_o)^2 - \beta^2} \\[2mm]
p &= \sqrt{\beta^2 - (n_3 k_o)^2} \\[2mm]
k_o &= 2\pi/\lambda_o
\end{aligned}
\qquad (4.17)
$$

where λ_o is the free-space wavelength of propagation.

Before proceeding further, we introduce normalizations that combine several guide parameters. Let us define a normalized width W by

$$W = k_o w \sqrt{n_2^2 - n_1^2}. \qquad (4.18)$$

Also, let us define the normalized guide index b related to the effective index N (and β) by

$$b = \frac{N^2 - n_1^2}{n_2^2 - n_1^2}. \qquad (4.19)$$

This normalized index takes on values between zero and unity. Using the expressions of Eq. (4.17) and the normalizations of Eqs. (4.18) and (4.19), we can rewrite the eigenvalue equation (4.16) in the form

$$W\sqrt{1-b} = \tan^{-1}\sqrt{\frac{b}{1-b}} + \tan^{-1}\sqrt{\frac{b}{1-b}} + m\pi. \qquad (4.20)$$

This equation can now be solved graphically. The graph thus obtained is used to determine the guide width, w, from the effective indices N_g and N_c. Fig. 4.6 shows the graphical solution of Eq. (4.20) for the $m = 0$ mode or the fundamental mode.

The effective index, N_c, requires us to find the equation that governs the transverse guided mode. We do this by considering the transverse guide as defined in Fig. 4.4. The pertinent regions are as labeled in the figure. In a manner exactly analogous to before, we seek solutions for the transverse confined modes. Using Maxwell's equations and matching the tangential field components at the interfaces, we obtain the transcendental eigenvalue equation governing the propagation characteristics in the transverse direction. This equation is similar in form to Eq. (4.16). It is

$$k_2 d = \tan^{-1}\left(\frac{\gamma_1}{k_2}\right) + \tan^{-1}\left(\frac{\gamma_3}{k_2}\frac{1 - \eta e^{-\gamma_3 t}}{1 + \eta e^{-\gamma_3 t}}\right) + m\pi, \qquad m = 0, 1, 2, \ldots \tag{4.21}$$

where η is defined as

$$\eta = \frac{\gamma_3 - \gamma_4}{\gamma_3 + \gamma_4}. \tag{4.22}$$

The transverse propagation constants in each layer are given by

$$
\begin{aligned}
\gamma_4 &= \sqrt{\beta^2 - (k_o n_o)^2} \\[1mm]
\gamma_3 &= \sqrt{\beta^2 - (k_o n_c)^2} \\[1mm]
k_2 &= \sqrt{(k_o n_g)^2 - \beta^2} \\[1mm]
\gamma_1 &= \sqrt{\beta^2 - (k_o n_c)^2}
\end{aligned}
\tag{4.23}
$$
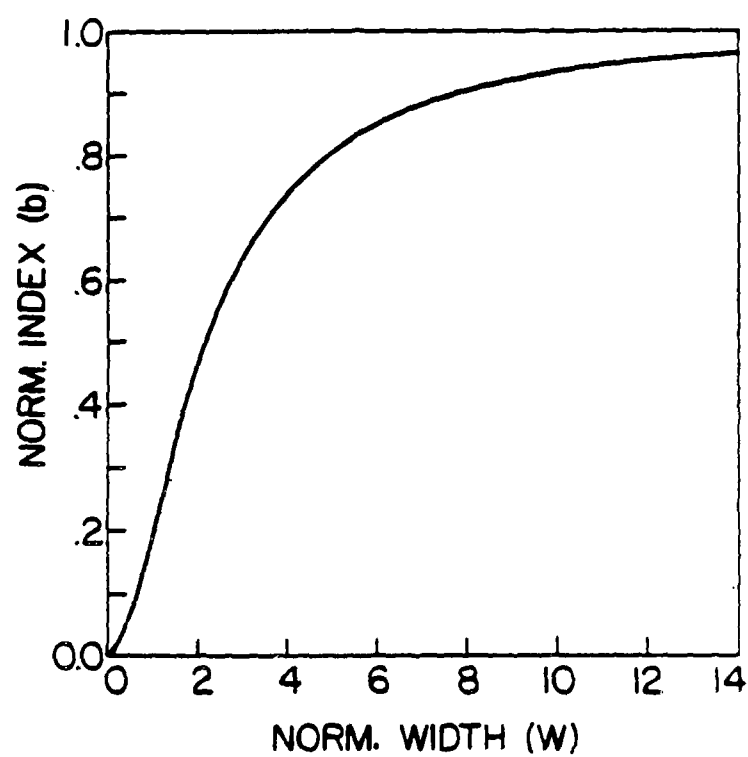
Figure 4.6: Normalized dispersion curve of the ...
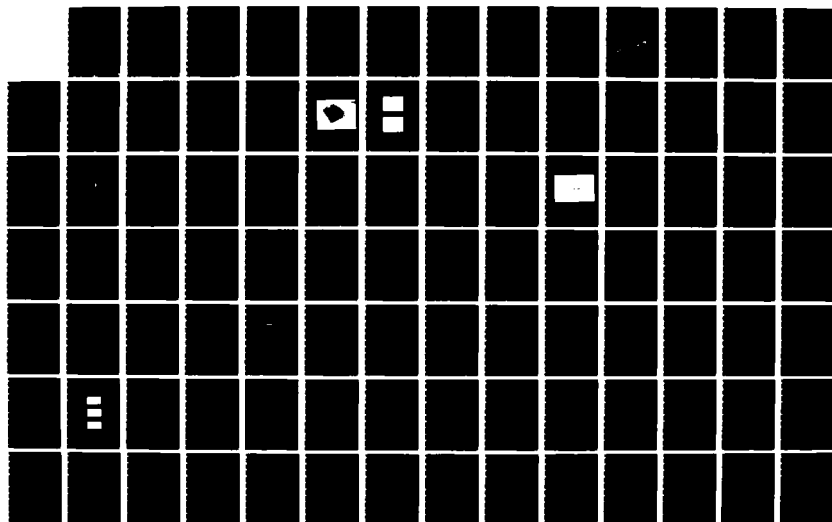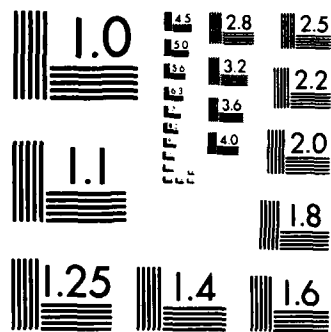
MICROCOPY RESOLUTION TEST CHART

NATIONAL BUREAU OF STANDARDS-1963-A

where $k_o = 2\pi/\lambda_o$ as before. We can define normalizations as before. Let the normalized thickness of the guide be

$$D = k_o d\sqrt{n_g^2 - n_c^2} \tag{4.24}$$

and the normalized guide index ρ be given by

$$\rho = \frac{N^2 - n_c^2}{n_g^2 - n_c^2}. \tag{4.25}$$

The effective index is still defined through

$$N = \beta/k \tag{4.26}$$

Using these normalizations and the expressions of Eqs. (4.22) and (4.23), we can recast the eigenvalue Eq. (4.21) in the form

$$D\sqrt{1-\rho} = \tan^{-1}\sqrt{\frac{\rho}{1-\rho}} + \tan^{-1}\left(\sqrt{\frac{\rho}{1-\rho}}\frac{1 - \eta e^{-2k_n\sqrt{\rho\sigma}t}}{1 + \eta e^{-2k_n\sqrt{\rho\sigma}t}}\right) + m\pi \tag{4.27}$$

where η is redefined as

$$\eta = \frac{\sqrt{\rho\sigma} - \sqrt{\rho + \frac{\alpha}{\sigma}}}{\sqrt{\rho\sigma} + \sqrt{\rho + \frac{\alpha}{\sigma}}} \tag{4.28}$$

and α and σ are constants defined by

$$\begin{aligned} \alpha &= n_c^2 - n_o^2 \\ \sigma &= n_g^2 - n_c^2 \end{aligned} \tag{4.29}$$

The normalized index of Eq. (4.25) ranges between zero and unity. As before, we can solve Eq. (4.27) graphically. The ridge thickness, t, appears as a parameter that can be set to any desired value. As expected, this thickness controls the effective index, N_c. The effective index N_g, in regions

1 and 3 in Fig. 4.5 is obtained by setting $t = 0$. In Fig. 4.7, we show the graphical solution of Eq. (4.27) for the fundamental transverse mode for two different ridge thicknesses.

4.2.1 A Numerical Example

The analysis performed in Section 4.2 and the resulting curves of Fig. 4.6 and Fig. 4.7 constitute the major design tools used in the determination of the appropriate waveguide dimensions in this study. As an example, we illustrate the use of these curves in the design of a typical ridge waveguide laser. Assume that only the fundamental ($m = 0$) transverse and lateral modes are allowed in the guide and that the wavelength of oscillation is $\lambda_o \simeq 0.86~\mu m$. Let the active region be a layer of GaAs, 250 Å thick surrounded by an optical waveguide of $Al_{0.18}Ga_{0.82}As$ whose thickness is 4400 Å. The total composite guide thickness, d, is 4650 Å. For an AlAs mole fraction of 0.18 in the waveguide, $n_g \simeq 3.469$ for $|y| \leq d$. suppose that the cladding layers have an AlAs mole fraction of 0.35; then $n_c \simeq 3.353$. This cladding layer is etched down to form a ridge waveguide whose height is $t = 0.8\mu m$. From these values, we can obtain the transverse normalized guide thickness from

$$D = \frac{2\pi}{\lambda_o}d\sqrt{n_g^2 - n_c^2} \simeq 3.05. \tag{4.30}$$

With this value of D, we determine the corresponding normalized guide index, ρ, from Fig. 4.7 (using the curve with $t = 0.8\mu m$), and this is $\rho = 0.65$. Through use of Eq. (4.25), we get the effective index value of $N_c = 3.429$. By using the curve for $t = 0$, we obtain the effective index value of $N_g = 3.411$.

We are now in a position to use the effective index values of N_c and
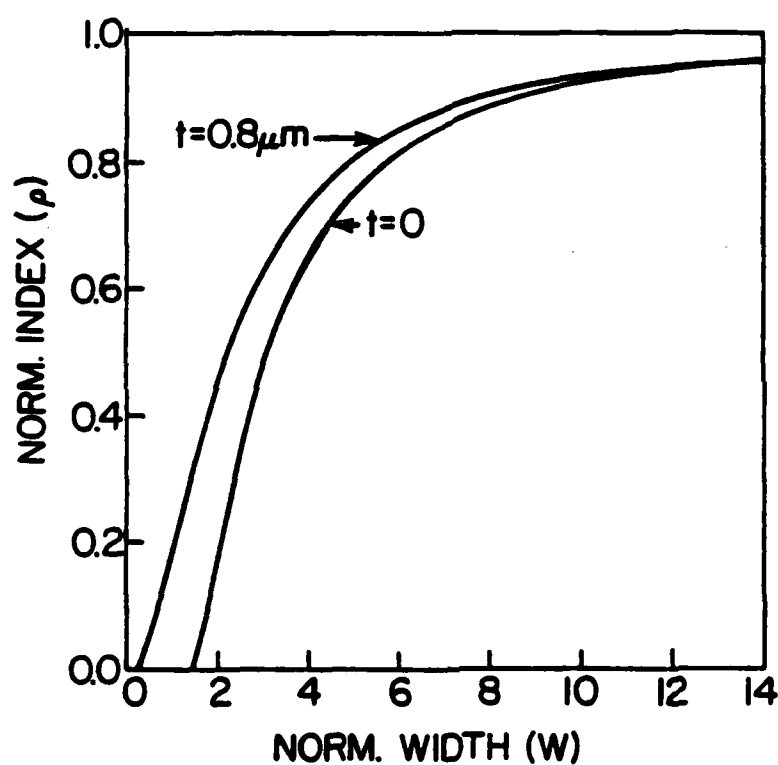
Figure 4.7: Normalized dispersion diagram of the transverse guide of the ridge waveguide laser structure.

N_g as if they were the ordinary indices used in Eqs. (4.18) and (4.19) in order to help determine the guide width, w in the lateral direction. Any combination of normalized width W and normalized index b that lies on the graph in Fig. 4.6, will give parameters for the fundamental lateral mode. For any one free parameter we choose, (as long as its value is on the curve) we can determine the others by using Eqs. (4.18), (4.19) and Fig. 4.6.

4.3 Phase-Locking by Evanescent Coupling

The simplest and most extensively studied method of phase-locking semi-conductor lasers is evanescent wave coupling. By fabricating the laser array elements sufficiently close to one another, the evanescent wave propagating in the interguide space can overlap with a guided wave in another guide. The idea here is that after several roundtrips in the cavity, the individual guided modes will eventually acquire a common phase because of the cross-coupling over the entire array.

The fraction of field energy coupled evanescently into a guide depends on several guide parameters. We discuss below the nature of this relationship.

The field expressions of Eqs. (4.13), (4.14) and (4.15) can be rewritten in terms of an arbitrary amplitude, A, so that:

$$\mathcal{E}_y(x) = Ae^{(qx+w/2)} \qquad x \leq -w/2 \qquad (4.31)$$

$$\mathcal{E}_y(x) = A\left[\frac{p}{h}\sin(hx) + \cos(hx)\right] \qquad |x| \leq w/2 \qquad (4.32)$$

$$\mathcal{E}_y(x) = A\left[\frac{p}{h}\sin(\frac{hw}{2}) + \cos(\frac{hw}{2})\right]e^{-p(x-w/2)} \qquad x \geq w/2 \qquad (4.33)$$

The constant A is chosen in such a way that the field $\mathcal{E}_y(x)$ in the previous equations corresponds to a power flow of one unit (per unit width in the y-direction) in a mode. This normalization condition can be expressed as

$$-\frac{1}{2}\int_{-\infty}^{\infty} E_y H_z^* = \frac{\beta_m}{2\omega\mu_o}\int_{-\infty}^{\infty}[E_y^m(x)]^2 dx = 1 \qquad (4.34)$$

where m denotes the m-th confined lateral mode. Substitution of Eqs. (4.31) through (4.33) into (4.34) results (after a bit of algebra and setting $q_m = p_m$) in

$$A = 2h_m\left[\frac{\omega\mu_o}{\beta_m(w + \frac{2}{p_m})(h_m^2 + p_m^2)}\right]^{1/2} \qquad (4.35)$$

The coupling coefficient from one guide to another is normally defined through the electric polarization perturbation. It can be shown that this coefficient, $\kappa_{n+1,n}$ is given by [60]

$$\kappa_{12} = \kappa_{21} = \frac{\partial^2}{2\omega\partial t^2}\int_{-\infty}^{\infty} P_{pert}(x,t)\mathcal{E}_y(x)dx \qquad (4.36)$$

$P_{pert}(x,t)$ is the polarization perturbation that leads into the coupling. By use of the index of refraction in the guide and the fields propagating in the two guides, we can rewrite Eq. (4.36) as

$$\kappa_{12} = \kappa_{21} = \frac{\omega}{4}\int_{-\infty}^{\infty} \mathcal{E}_{1y}^*(x)\epsilon_o(N_c^2 - N_g^2)\mathcal{E}_{2y}(x)dx \qquad (4.37)$$

where N_c and N_g are the effective indices of the guide as defined previously.

Using the field expressions of Eqs. (4.31) through (4.33) and the value for the constant A in Eq. (4.35), we can perform the integration of Eqn. (4.37). In the field expressions for the second guide, it should be noted that the expressions are shifted by $w + \tilde{s}$, where w is the guide width and $\tilde{s}$ is the

interguide center-to-center separation. After a fair amount of algebra, we arrive at the result

$$\kappa_{12} = \kappa_{21} = \left[\frac{2h_o^2 p_o}{\beta_o (w + \frac{2}{p_o})(h_o^2 + p_o^2)} \right] e^{-p_o \hat{s}} \qquad (4.38)$$

Notice that this result has been particularized to the fundamental, symmetric lateral mode (the subscript o is an indication of this fact). The physical meaning of this equation is intuitively obvious. It says that the coupling between the laser guides increases exponentially as the guides are brought closer to one another.

Although the evanescently coupled lasers have been studied extensively, it has not been possible to consistently achieve phase-locked operation. In the majority of the cases reported in the literature [61]-[69], the arrays have tended to operate in a mode that leads to a double-lobed far-field intensity pattern. It is speculated [70,71,72] that this mode of operation is favored whenever adjacent lasers in the array maintain a phase difference between them of π radians. This phase difference has been attributed to loss between the active elements of the array [73,74,75]. At the moment, there does not seem to be a method to correct this phase difference in the parallel-element geometry.

Recent efforts in this field have now shifted to exploring other device structures that might yield narrow, single-lobe far-field patterns. Research in new device structures that is being conducted concurrently with our own effort is going on at the University of California at Berkeley, the California Institute of Technology and Spectra Diode Laboratories. The groups at UC Berkeley and Cal Tech are working on a technique of coupling based on diffraction. In their structure, a region where the modes are not guided is included just before one of the laser mirrors. After reflection from the

mirror, the portion of radiation that returns is coupled into more than one guide [76,77]. The group at Spectra Diode is refining a technique originally used by Scifres *et al.* [78]. This technique involves coupling via a "Y"-branching guide [79]. In the next section, we introduce and discuss the structure for phase-locking that has been studied in this thesis.

4.4 Mixed-Mode Phase-locking

The motivation behind the mixed-mode phase-locking (M^2PL) technique was to provide another method of coupling the lasers. The basic idea is to retain the usual parallel-element array guides but to incorporate a section in the middle of the device where the modes are unguided. This middle section forms the mode-mixing region. It allows the eigen-modes from each individual guide to mix because of diffraction, thus promoting phase-locking. If indeed there is loss between the guides, the presence of this uniformly pumped region will also minimize this loss. We illustrate in Fig. 4.8 the schematic of the M^2PL laser array.

This novel laser design allows the possibility of coupling to more than just nearest adjacent neighbor. Unlike the structure being studied by the groups at Berkeley and Cal Tech, our design offers the feature of simultaneous bidirectional coupling. The M^2PL laser is also capable of much more efficient coupling than the other structures. In the Berkeley structure, having the coupling region adjacent to the facet makes it susceptible to the intrinsic absorption losses at the facet and also to the normal losses due to transmission at the mirror. One major disadvantage of the Berkeley structure is that it is not easy to control the length of the coupling region during the mirror-cleaving process. The magnitude of this length, of course, is of prime importance in determining in-phase coupling. We shall discuss this

further in the next section. In the M²PL laser, having the mode-mixing region in the middle of the device means that it can be predetermined and defined accurately by photolithography. This length is then guaranteed not to change during all the subsequent device processing steps. If desired, the M²PL laser can also be designed to retain the evanescent wave coupling property of the previous laser structures. This, however, is not absolutely necessary as sufficient coupling can be attained by use of the mode-mixing region.

4.5   Theory of Mixed-Mode Phase-Locking

In Section 4.2, we assumed that the ridge waveguides that form the M²PL laser arrays were passive. This assumption allowed us to calculate the important parameters of the waveguides without the added complication of the gain and loss processes that are intrinsic to the operation of a laser. In this section, we wish to modify the assumption to include gain and loss. Ordinarily, the quantitative determination of the allowed mode structures for waveguides that include gain and loss is a prohibitively difficult task. In the analysis we will undertake here, however, we shall appeal to empirical evidence to bypass the complicated calculations.

In has been demonstrated experimentally [80] that for a well behaved lasing mode, where the lateral extent of the mode is determined by a stripe width, the near- and far-field scans of the lowest order mode is Gaussian in form. The Gaussian modal distribution of the emitted radiation is a result of the complex photon-carrier interactions in the cavity. These interactions manifest themselves macroscopically as gain and loss. Given these facts, it is reasonable to assume that the individual guided modes in the ridge waveguides we use here are Gaussian. Furthermore, each guide (as analysed
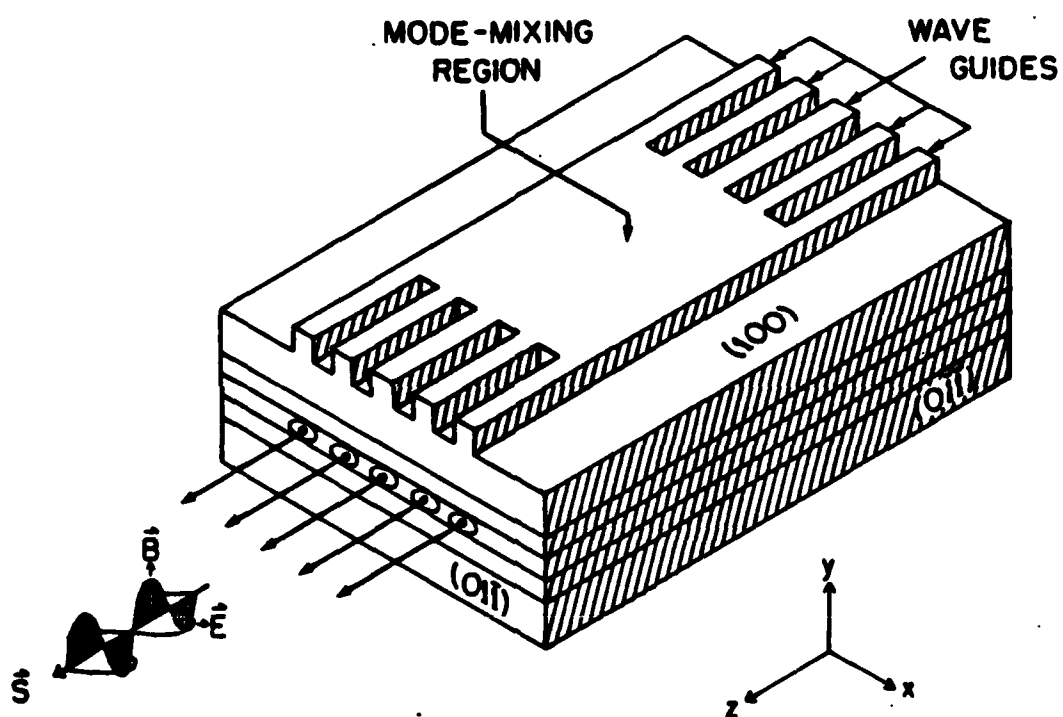
Figure 4.8: The schematic structure of the M²PL laser array.

in Section 4.2) can be chosen such that it supports only the fundamental mode.

We begin our analysis of the M^2PL lasers by formulating a simple model. Having assumed that the allowed mode structure in each guide is Gaussian, we write the paraxial scalar wave equation describing the propagation characteristics of the mode:

$$\nabla^2 u + k^2 u = 0 \qquad (4.39)$$

where u is a field component and $k = 2\pi n_{eff}/\lambda_o$ is the propagation constant in the medium; n_{eff} is the effective index of refraction. For light propagating in the z-direction, let

$$u(x, y, z) = \mathcal{E}(x, y, z) \exp(-jkz) \qquad (4.40)$$

where $\mathcal{E}(x, y, z)$ is a slowly varying complex function that represents the nonuniform field intensity distribution, the beam expansion as a function of propagation distance and also phase front curvature. Substitution of Eq. (4.40) into Eq. (4.39) results into

$$\frac{\partial^2 \mathcal{E}}{\partial x^2} + \frac{\partial^2 \mathcal{E}}{\partial y^2} - 2jk\frac{\partial \mathcal{E}}{\partial z} = 0 \qquad (4.41)$$

where the function $\mathcal{E}(x, y, z)$ is assumed to have a slow variation with z and therefore we have neglected the second derivative of $\mathcal{E}(x, y, z)$ with respect to z in comparison to the other terms. Eq. (4.41) has the form of the time-dependent Schrödinger equation in two dimensions, where z plays the role of time [81]. The solution to this equation has the form

$$\mathcal{E}(x, y, z) = \exp\left\{-j\left[P(z) + \frac{k}{2q(z)}r^2\right]\right\} \qquad (4.42)$$

where $r^2 = x^2 + y^2$. We have also introduced the "q-parameters" for the description of Gaussian beam optics [82,83,84]. The parameter $P(z)$ is complex and represents the phase shift associated with the propagation of the light, $q(z)$ is also complex and describes the Gaussian variation of the mode intensity with distance r from the optic axis. When we substitute Eq. (4.42) into Eq. (4.41), we obtain

$$-(\frac{k}{q})^2 r^2 - 2j(\frac{k}{q}) - k^2 r^2 (\frac{1}{q})\prime - 2kP\prime = 0 \qquad (4.43)$$

where the prime denotes differentiation with respect to z. Eq. (4.43) is true when the different coefficients of all powers of r equal to zero so that

$$(\frac{1}{q})^2 + (\frac{1}{q})\prime = 0 \qquad (4.44)$$

$$P\prime = \frac{-j}{q} \qquad (4.45)$$

It can be shown that Eq. (4.44) integrates to [83]

$$q(z) = j\frac{\pi w_o^2 n_{eff}}{\lambda_o} + z \qquad (4.46)$$

An imaginary constant of integration, $q_o = (j\pi w_o^2 n_{eff}/\lambda_o)$, has been included in this result. The choice of this constant leads to physically meaningful waves whose energy is closely confined to the z-axis.

Inserting this result into Eq. (4.45) and performing the required integration yields the complex phase parameter

$$P(z) = j\ln\sqrt{1 + (z\lambda_o/\pi w_o^2 n_{eff})^2} - \tan^{-1}(\lambda_o z/\pi w_o^2 n_{eff}). \qquad (4.47)$$

The constant of integration has been conveniently chosen to be zero. The only consequence of doing this is a shift in the time origin of the field

solutions. When we substitute the expressions of Eq. (4.46) and Eq. (4.47) into Eq. (4.40) via Eq. (4.42) we obtain the desired functional dependence of the fundamental Gaussian beam shape in the guide:

$$u(x, y, z) = \frac{w_o}{w(z)} \exp\left\{-j(kz - \varphi(z)) - (x^2 + y^2)\left(\frac{1}{w^2(z)} + \frac{jk}{2R(z)}\right)\right\}$$
(4.48)

This is our basic result with the following parameter definitions: the dimension $2w_o$ is the minimum diameter of the Gaussian beam, called the *beam waist*. For ideal conditions, we shall assume that this parameter is on the order of the guide width.

$$w(z) = w_o^2\left[1 + \left(\frac{z\lambda_o}{\pi w_o^2 n_{eff}}\right)^2\right]$$
(4.49)

$$R(z) = z\left[1 + \left(\frac{\pi w_o^2 n_{eff}}{\lambda_o z}\right)^2\right]$$
(4.50)

$$\varphi(z) = \tan^{-1}\left(\frac{\lambda_o z}{\pi w_o^2 n_{eff}}\right)$$
(4.51)

The parameter $w(z)$ gives the expansion of the beam diameter as a function of z in the medium without wave guides; $R(z)$ is the radius of curvature of the Gaussian wavefront at z. The angle by which the beam spreads from the optic axis is given by $\varphi(z)$.

Now consider the illustration depicted on Fig. 4.9. The figure shows three parallel lasers with a mode-mixing region at the center of the structure. The guided modes of the structure, when they reach the mode-mixing region, will spread in a manner described by Eq. (4.48). This spreading, depending on the length of the mode-mixing region z_1 will couple a fraction of the radiation guided in guide 2 to guide 1 and vice-versa. In order for

radiation from one guide to couple coherently to its nearest neighbor, the phase difference between the phase fronts of the modes emanating from the two guides in question must be an integral multiple of 2π. This is another way of saying that the optical path difference of the coupled wave must be an integral number of wavelengths. If this is true for all guides across the laser array, then we have the necessary condition for phase-locking. From Eq. (4.48), we observe that after traveling a distance z, a mode acquires a phase given by

$$\phi(z) = kz - \varphi(z) \tag{4.52}$$

The condition for *collective* coherence as stated above can be expressed thus:

$$\Delta\phi = \frac{\phi_2 - \phi_1}{2\pi} \tag{4.53}$$

where $\Delta\phi$ is defined only for integer values. From Eqs. (4.52), (4.53) and the geometry of Fig. 4.9, we obtain

$$\Delta\phi = \frac{n_{eff}}{\lambda_o}\left[\sqrt{z_1^2 + \bar{s}^2} - z_1\right] + \frac{1}{2\pi}\tan^{-1}\left[\frac{\lambda_o z_1}{\pi w_o^2 n_{eff}}\right] - \frac{1}{2\pi}\tan^{-1}\left[\frac{\lambda_o\sqrt{z_1^2 + \bar{s}^2}}{\pi w_o^2 n_{eff}}\right] \tag{4.54}$$

By solving Eq. (4.54) graphically, one can determine the correct length of the mode-mixing region for *collective* coherence in order to achieve phase-locking. Note that the inter-guide center-to-center separation, $\bar{s}$, appears as a parameter in this equation and it can be set to any reasonable value. Fig. 4.10 depicts a graphical solution of this equation for several values of the inter-guide separation, $\bar{s}$. Given this value, the right length, z_1, for the mode-mixing region can be established by a quick reference to the figure.
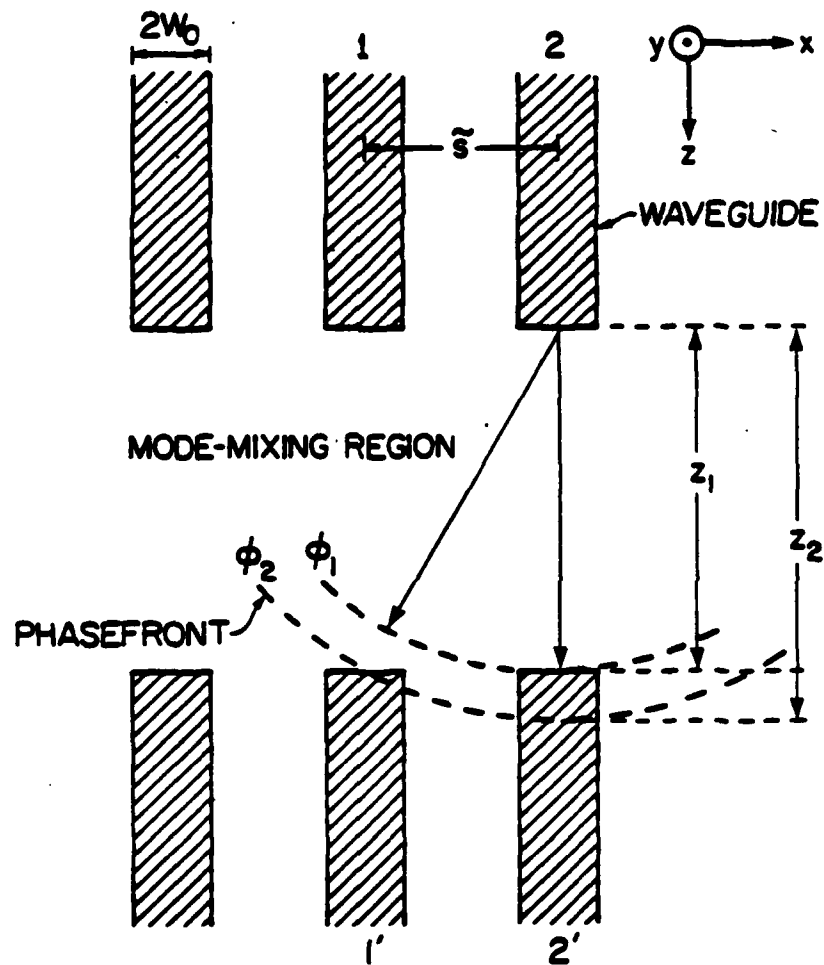
Figure 4.9: An illustration of the diffraction-coupling scheme of the M^2PL laser array.
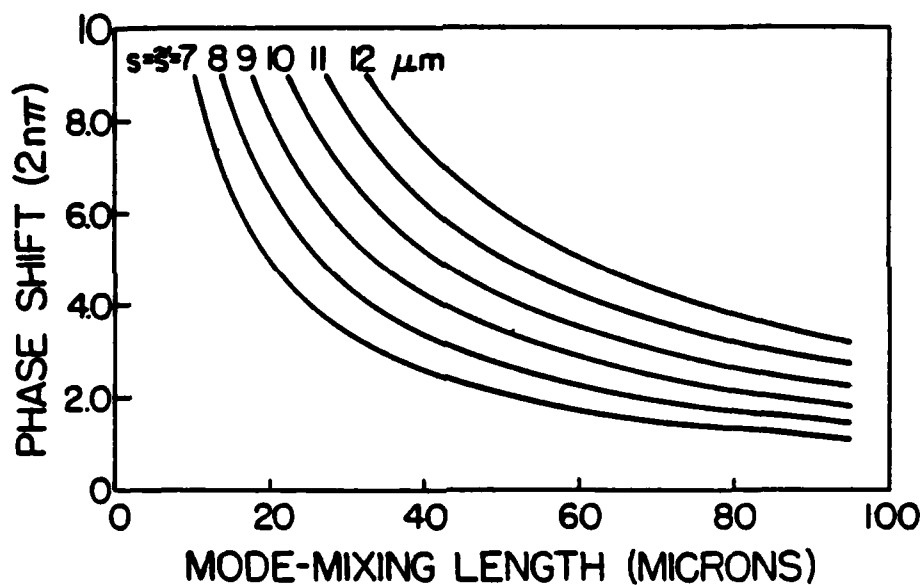
Figure 4.10: The relationship of the phase-locking condition to the length of the mode-mixing region.

Chapter 5

Discussion of Device Results

This chapter presents and discusses the experimental results of the mixed-mode phase-locked laser arrays studied in this thesis. Some of the theoretical and analytical aspects of the work discussed earlier are unified with the experimental device results. We begin the chapter by showing, in Fig. 5.1, a photomicrograph of the device whose results are to be discussed. Each guide in this figure is 3 μm wide and the center-to-center spacing of the guides is 7 μm. The central mode-mixing region is 75 μm long and the waveguide regions on either side are approximately 100 μm long.

5.1 Current Versus Voltage Characteristics

The measurement of the current versus voltage (I-V) characteristic of a laser device usually represents one of the very first measurements done on the device. Fig. 5.2 shows a representative I-V characteristic of an M^2PL laser. The forward turn-on voltage is $\sim$1.1 V, a typical value for (Al,Ga)As/GaAs laser diodes. The reverse characteristic of the I-V displays a very sharp breakdown at a voltage of $\sim$19.0 V. The sharpness of the breakdown point is an indication of the abruptness of the p-n junction. An estimate of

the background doping, N_B, of the active layer can be made through the formula

$$V_B = 60(E_g/1.1)^{3/2}(N_B/10^{16})^{-3/4} \tag{5.1}$$

where V_B is the breakdown voltage and E_g is the "band gap" of the active layer. This approximate universal formula for abrupt junctions was first derived by Sze and Gibbons [85].

For the breakdown voltages of 19–20 volts encountered in our lasers, we estimate the background doping to be about 7.0×10^{16} cm^{-3}. This value is reasonable for unintentionally doped GaAs layers grown by molecular beam epitaxy. The diffusion of Be (a p-dopant) from the top cladding layer may actually account for the slightly high value of the background. The active layer of this particular device is composed of an undoped system of multiple quantum wells surrounded by an undoped waveguide layer several hundred angstroms thick. It is therefore a complicated matter to determine the exact location and extent of the depletion layer. The background carrier density as determined here, is at most, an upper limit. What is important to realize here is that a low background carrier density is essential in the active region to minimize excessive free carrier optical absorption during the operation of the laser device.

The general sharpness of the turn-on and breakdown points of the I-V characteristic are an indirect proof that the device does not have additional unwanted current paths. This fact is borne out by the low threshold currents measured for these devices.

Another piece of valuable information obtainable from the I-V characteristic is the quality of the ohmic contacts to the device. One can assess the quality of the ohmic contacts by measuring the forward series resistance
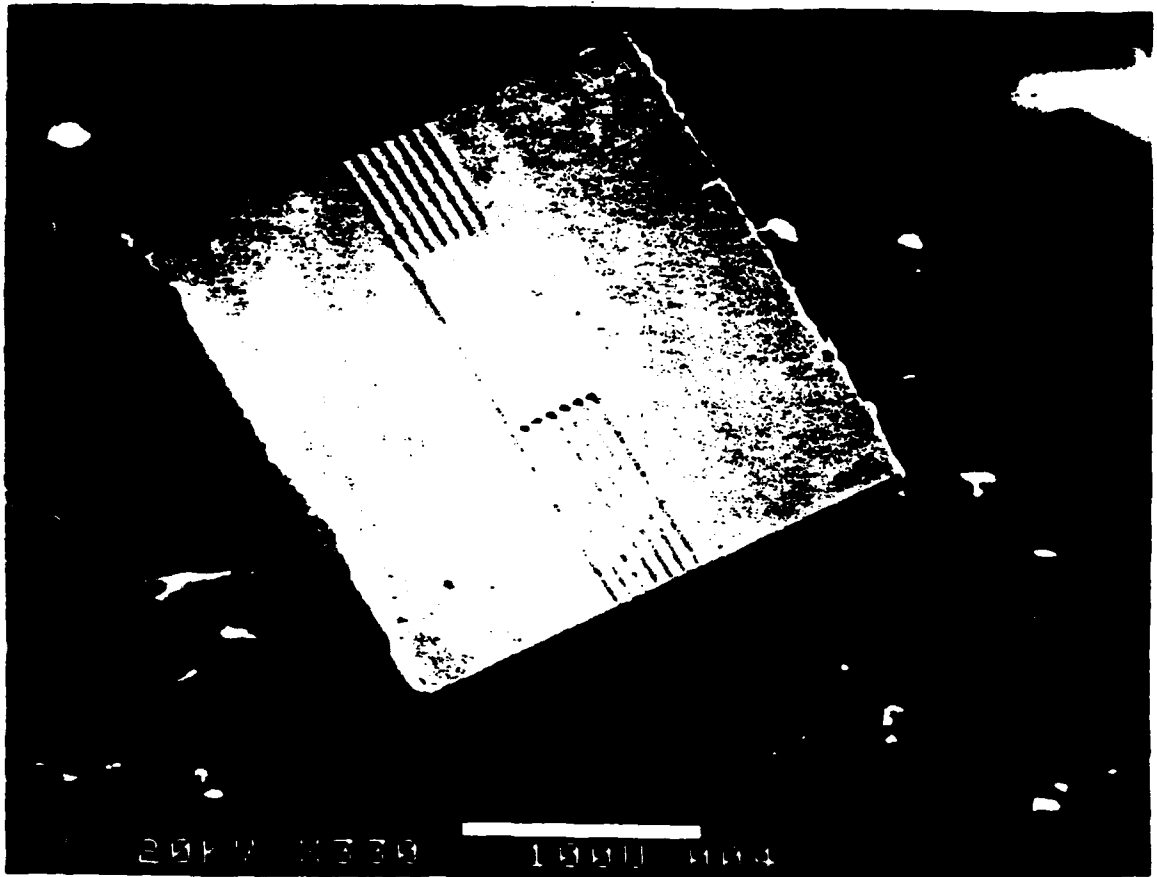
Figure 5.1: A photomicrograph of the mixed-mode phase-locked laser array.

I-V Characteristics
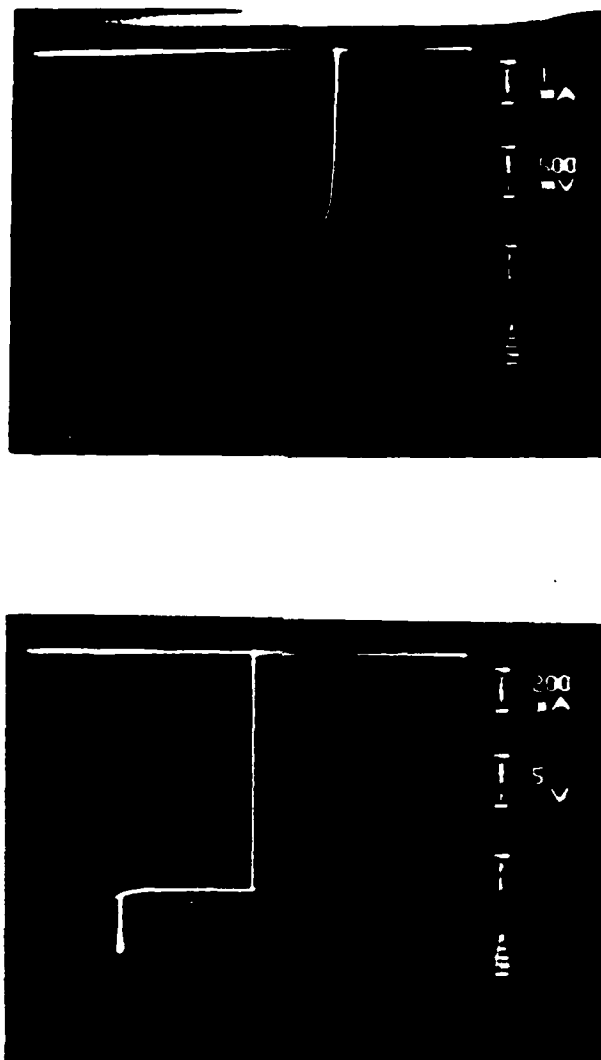
Figure 5.2: Current versus voltage (I-V) characteristics of a typical mixed-mode phase-locked laser array.

of the diode. This resistance is very simply the reciprocal of the differential slope of the I-V curve. Fig. 5.3 shows the measurement of this resistance performed on a commercial parameter analyzer. The measured differential series resistance is about 4.5 Ω. In order to correctly evaluate this resistance, one must first measure the resistance introduced by the sampling probes. In our case, this resistance is about 3 Ω. Therefore, the true differential series resistance of the M²PL lasers is about 1.5 Ω. Although this value is reasonable, it can and must be made lower if long term cw operation is desired.

5.2 Light Versus Current Characteristics

In the basic p-n junction laser structure, the two important parameters that characterize the quality of the device are the threshold current density and the external differential quantum efficiency. The threshold current density is a relative measure of how many electron-hole pairs have to be injected to overcome the spontaneous emission process and the associated cavity losses before the onset of lasing. The lower the threshold, the better the device. The major factors that control the threshold current density were outlined and discussed in Chapter 3.

For the lasers studied during the course of this project, the threshold current density as a measure of quality only has meaning when it is used in connection with broad area lasers. During the initial phase of the project, broad area lasers fabricated from regular double heterojunction structures exhibited threshold current densities of about 2.5 kA/cm². With improvements in crystal quality (largely attributed to growth techniques) and a change to quantum well structures, we were able to obtain lower thresholds. For a multiple quantum well structure, the best threshold current
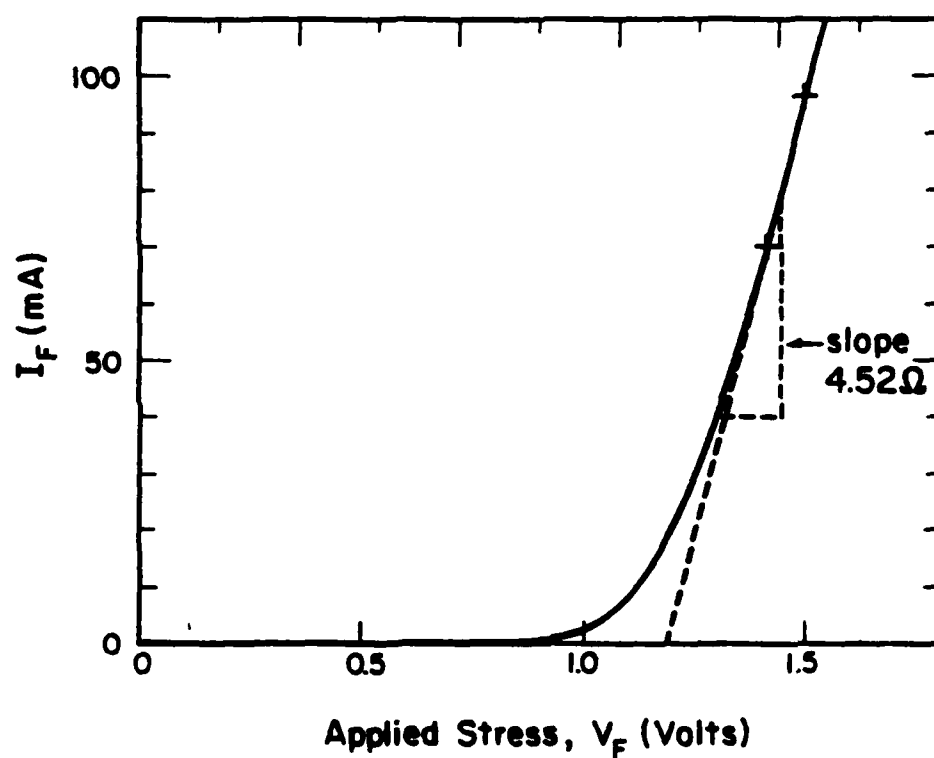
Figure 5.3: Measurement of the forward series resistance, r_s, of an M^2PL laser diode.

density obtained was about 200 A/cm². This is an order of magnitude decrease over our previous results. This value is in good agreement with other state-of-the-art values reported [86,87,88,89] for lasers of similar construction.

In the phase-locked arrays, because of the way the devices are constructed, the pumping current is not uniform over the entire structure. It is therefore more difficult to talk about threshold current densities. Specifically, for the M²PL lasers, the regions of low resistance over the ridge waveguides pass more current through them than the high resistance interguide regions. For these lasers, the threshold current (measured in units of amperes) replaces the current density. In multiple parallel-stripe devices, this measure is often quoted as the threshold per stripe.

The fact that lower threshold current densities are measured for devices fabricated from multiple quantum well structures is consistent with the photoluminescence results reported in Chapter 2. The physical basis of the reasons why this should be so were further discussed in Chapter 3. It was shown theoretically that low threshold current densities are to be expected for lasers fabricated from these structures.

The other measure of quality, the external differential quantum efficiency, is a reflection of the conversion efficiency of injected electron-hole pairs to photons. Since what is actually measured is affected by spontaneous emission, cavity and mirror losses, it is called the external efficiency. This is to distinguish it from the internal efficiency which we cannot measure. The internal efficiency is the fraction of injected electron-hole pairs converted into stimulated emission. The external efficiency does provide a good indication of this parameter. Quantitatively, this parameter is defined as

$$\eta_{ext} = \left(\frac{q\Delta P_{opt}}{\Delta I}\right) \tag{5.2}$$

where ΔP_{opt} is a change in optical intensity for a corresponding change in excitation current, ΔI. The change ΔI must be beyond the lasing threshold current, I_{th}.

Since the spontaneous emission intensity is clamped at threshold, the total emission intensity above threshold maybe represented as [90]

$$qP_{opt} = F_{sp}\eta_{sp}I_{th} + F_{st}\eta_i(I - I_{th}) \tag{5.3}$$

where F_{sp} and F_{st} are, respectively, the photon escape probabilities for spontaneous and stimulated emission. The efficiencies for the corresponding photon conversions are denoted by η_{sp} and η_i. This expression is intuitively obvious from Fig. 5.4. It then follows from Eq. (5.3) according to the definition of Eq. (5.2) that

$$\eta_{ext} = F_{st}\eta_i \tag{5.4}$$

The probability for stimulated photon escape, F_{st}, is the ratio of the externally measured optical power to the total optical power generated internally. This is given by

$$F_{st} = P_{out}/(P_{out} + P_{abs}) \tag{5.5}$$

where P_{out} is the output power at both facets and P_{abs} is the total optical power lost to other mechanisms such as free carrier absorption and diffraction at the optical cavity interfaces. The output power, P_{out}, is generally considered as a "loss" from the cavity. This is because the photons in P_{out} can no longer contribute to stimulating others in the cavity. This external loss term is expressed as $(1/L)\ln(1/R)$ [91,92]. The internal cavity losses

are lumped together and designated as α_i. Collecting these facts together and using Eq. (5.5) in Eq. (5.4) gives us the expression for the differential quantum efficiency:

$$\eta_{ext} = \frac{(1/L)\ln(1/R)}{\alpha_i + (1/L)\ln(1/R)} \tag{5.6}$$

where L and R are as defined previously in Chapter 3. From Eq. (5.6), it is clear how to vary the device parameters in order to get a high differential external quantum efficiency. For high external efficiencies, the internal loss term, α_i, must be minimized. This term can be minimized by making sure that there is little free carrier absorption of the photons. This is done by assuring a low background doping in the active layer. The diffractional losses at the hetero-interfaces are minimized if these regions are smooth. The cavity length L and the facet reflectivity R must be chosen judiciously because although long cavities and large reflectivities should lead to smaller $(1/L)\ln(1/R)$ and high η_{ext}, the total cavity losses will increase with length. The number of longitudinal modes also increases so that more of them have to compete for the available gain. This in turn may actually raise the threshold current density.

The typical external differential efficiency measured for the M^{2}PL lasers was about 0.24 Watts/Amperes per facet. These devices had room temperature threshold currents that ranged from about 300-480 mA for 7-element arrays. The guides are 3.0 μm wide with a center-to-center spacing of 7.0 μm. The average length of most devices tested is about 300 μm. Fig. 5.4 shows a typical light versus current (L-I) characteristic of an M^{2}PL laser. Two features of this figure are noteworthy. First, we notice that the characteristic is linear. This linearity is very important for devices of this class and we will discuss it further below. Secondly, we observe that the device
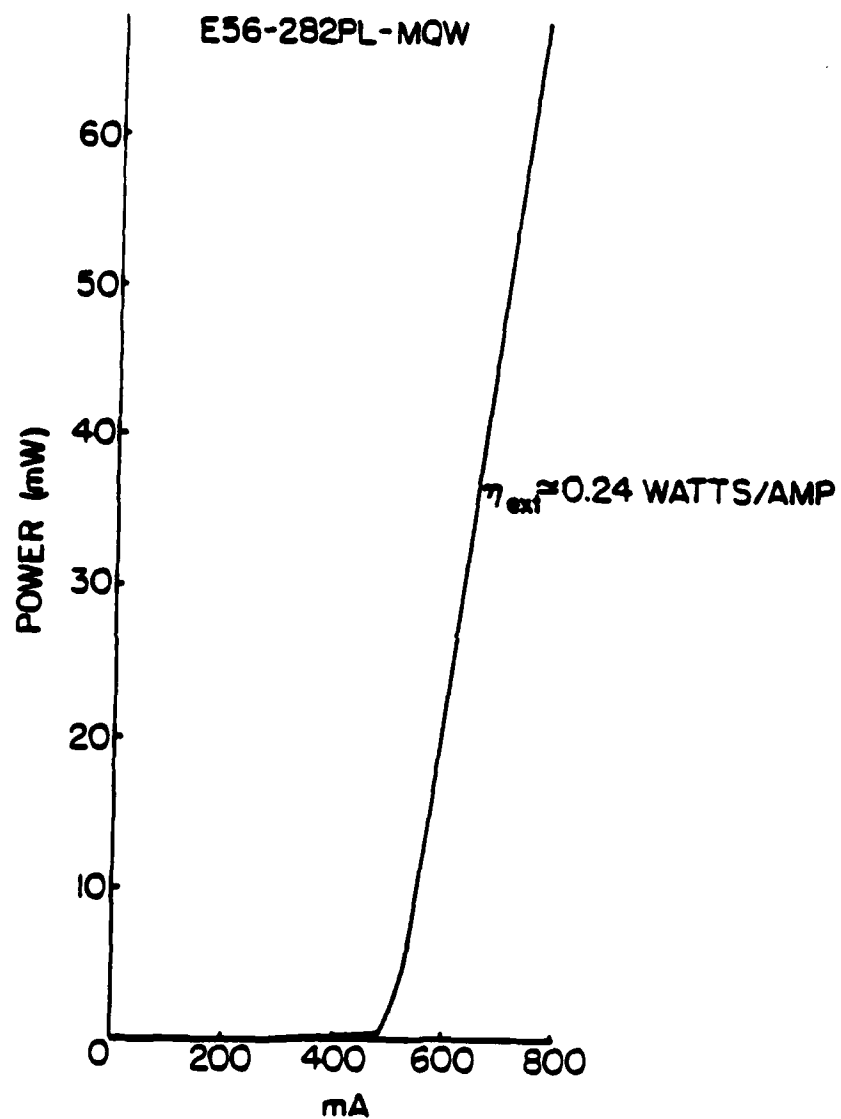
Figure 5.4: Light versus current (L-I) characteristic of a typical M^2PL laser device.

seems to have two threshold currents. This behavior was observed in all the devices tested. By monitoring the near-field pattern on an infra-red vidicon, it was possible to observe the onset of the lasing process. During the first threshold, it was noticed that some of the devices in the array were not as brightly lit as the others; on increasing the current further, the entire array was uniformly lit and this point corresponded to the second threshold. The other point to notice about Fig. 5.4 is that this device displays very little amplified spontaneous emission (or super-radiance), i.e. below threshold, there is little emission.

The stability and linearity of the L-I characteristic is of prime importance if the laser devices are to be used in fiber-optic communications where the light might need to be modulated. This stability can only be obtained from laser devices that have real index-guiding for the lateral modes. In lasers with non-linearities (kinks) in their L-I curves, it has been found that the non-linearities lead to mode profile deformation and even lateral shifts [94,95] which could lead to very unstable far-field patterns. Also, such undesirable features like relaxation oscillations [96] are enhanced in devices with non-linearities in their L-I curves.

In other studies on lasers where the lateral mode confinement is determined solely by the pumping current (i.e. gain), the light emerging from the devices is often found to have astigmatic properties (focusing to more than one point) [97].

Our devices did not exhibit any of the features discussed above. It is our belief that the strong index-guiding designed into the arrays contributed to the stable charactristics.

5.3   Emission Spectra

The spontaneous emission spectrum of a typical M^2PL laser below thresh-
old is shown in Fig. 5.5. This spectrum suggests the presence of several
longitudinal modes, each separated from the other by 2.5 Å. The mode
separation is given by the expression

$$\Delta\lambda = \frac{\lambda_o^2}{2n_{eff}L} \tag{5.7}$$

where λ_o is the free space lasing wavelength, n_{eff} is the effective index of
refraction and L is the cavity length as before. If desired, this expression
can be used to calculate the effective index of refraction, n_{eff}. All the other
parameters in Eq. (5.7) are readily measurable.

For a cavity length $L \sim 275$ μm, and the center wavelength of 0.864 μm
shown in the figure, the value of $n_{eff} \sim 5.43$. This value is reasonable and
it compares quite well with that extrapolated from the data of Marple [98]
given for GaAs at room temperature. The value estimated from Marple's
data is a little over 5.6. It should be recalled that the active layers of the
devices studied here are composed of multiple quantum well systems. The
effective index therefore is expected to be lower than that of pure GaAs.
Our estimate is therefore consistent with this fact.

The spectrum in Fig. 5.5 is typical of quantum well lasers. The Fabry-
Perot modes are superimposed on top of a well-defined and narrow sponta-
neous emission line. This line has a full-width at half-maximum of ~10 Å.
This width is to be contrasted with that of a normal double heterojunction
laser of about 200 Å or more. The superiority of the quantum well lasers
is clearly evident from these facts.

Using a technique developed by Hakki and Paoli [99], the spectral gain
of lasers can be experimentally determined from spectra similar to that in
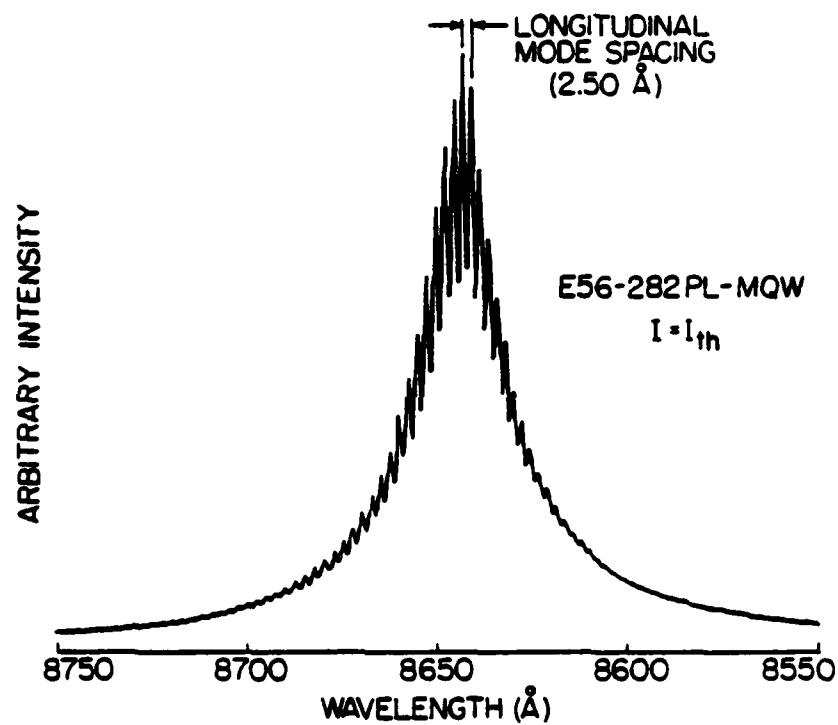
Figure 5.5: The spontaneous emission spectrum of a typical M²PL laser below lasing threshold.

Fig. 5.5. We have performed such an experiment. In our measurements, the desired wavelength resolution is attained by operating the 0.75 meter spectrometer used with slit widths of ≤ 30 μm.

Very simply, the gain is obtained by measuring the depth of the modulation caused by the Fabry-Perot resonances in the emission spectrum. The gain at any wavelegth is obtained by first averaging two successive peaks, $(I_i + I_{i+1})/2$, in the emission spectrum of Fig. 5.5 and then dividing by the intermediate valley, V_i. The modulation depth, r_λ, is therefore

$$r_\lambda = \frac{I_i + I_{i+1}}{2V_i} \tag{5.8}$$

The net gain is then obtained from the relation [100]

$$G_\lambda = \frac{1}{L} \ln \left[\frac{\sqrt{r_\lambda} + 1}{\sqrt{r_\lambda} - 1} \right] + \frac{1}{L} \ln R \tag{5.9}$$

where, as before, L is the cavity length and R the facet reflectivity.

From a spectrum very similar to the one shown here, we have calculated the gain spectrum of an M^2PL laser below threshold. This spectrum appears in Fig. 5.6. Our result indicates that the loss rapidly drops to a minimum at around 8640 Å from the short wavelength side of the spectrum. The loss spectrum narrows as this wavelength is approached. The loss (gain) spectra of quantum well lasers narrow much more dramatically than those of regular double heterostructure lasers as the lasing threshold is approached. This is because of the higher electronic density of states and the discrete nature of the transitions involved.

At the lasing threshold, the longitudinal mode competition for gain is won by two or three dominant modes. These modes, at the allowed wavelengths of oscillation, acquire all the gain that the medium is capable of delivering. The particular modes chosen depend on the length of the optical
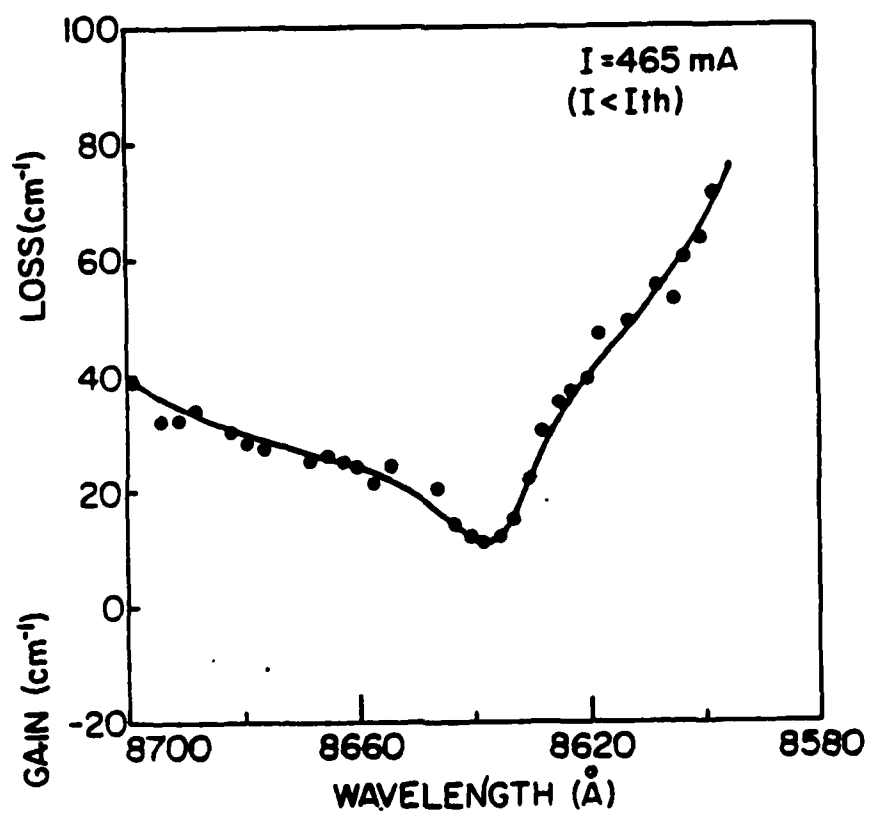
Figure 5.6: The gain (loss) spectrum of a quamtum well laser just below threshold.

cavity and the gain linewidth. In essence, the lasing modes are determined by a convolution of the Fabry-Perot etalon modes and the gain line function of the medium from which the laser is fabricated. From Eq. (5.7), we note that the separation of the Fabry-Perot modes can be made large by decreasing the cavity length, L. By doing this, the laser medium linewidth samples only a few Fabry-Perot modes, thus improving the chances of mode selectivity.

The lasing spectrum of an M^2PL laser is shown in Fig. 5.7. The spectrum is taken at $1.3I_{th}$. The active region of this device is composed of a multiple quantum well system. The general features of the spectrum bear some similarity to the spectrum obtained from a laser with a single quantum well. Such a spectrum is shown in Fig. 5.8. Both spectra exhibit two major peaks. These spectra are notably different from others reported in the literature [101] for phase-locked devices. Our spectra display clean, well-resolved 2 to 3 major longitudinal modes whereas those of Ref. [101] exhibit several longitudinal modes. The emission wavelength is predominantly centered around 864-864.6 nm, a value smaller than that corresponding to the intrinsic band gap of pure GaAs. Excluding band filling effects, this emission is attributed to transitions from the quantized energy levels in the quantum wells. The center wavelength is slightly different from that due to a photoluminescence transition from the $1e \rightarrow 1hh$ level found in Chapter 2, possibly because of the tilted band configuration in a laser device when it is forward biased.

Closer examination of the spectra reveals that in fact a family of 2 to 3 longitudinal modes exist in these lasers. An envelope curve can be drawn over each of the families. These mode families are attributed to oscillations occuring in non-axial modes in the laser cavity. In general, they are undesirable and a lot of research effort has gone into developing structures that
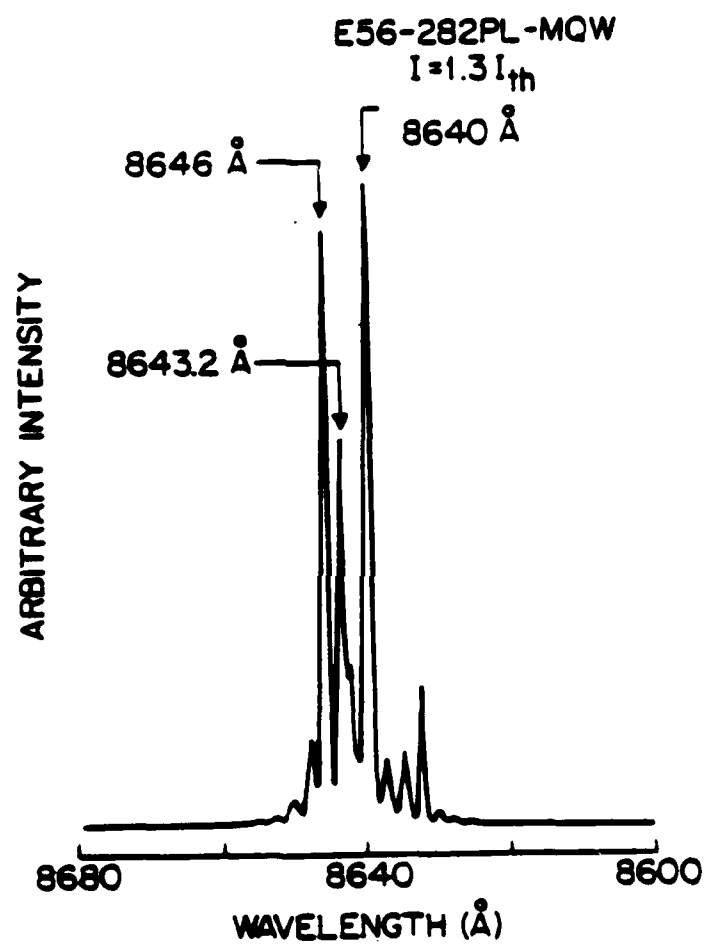
Figure 5.7: The lasing spectrum of a multiple quantum well laser device.
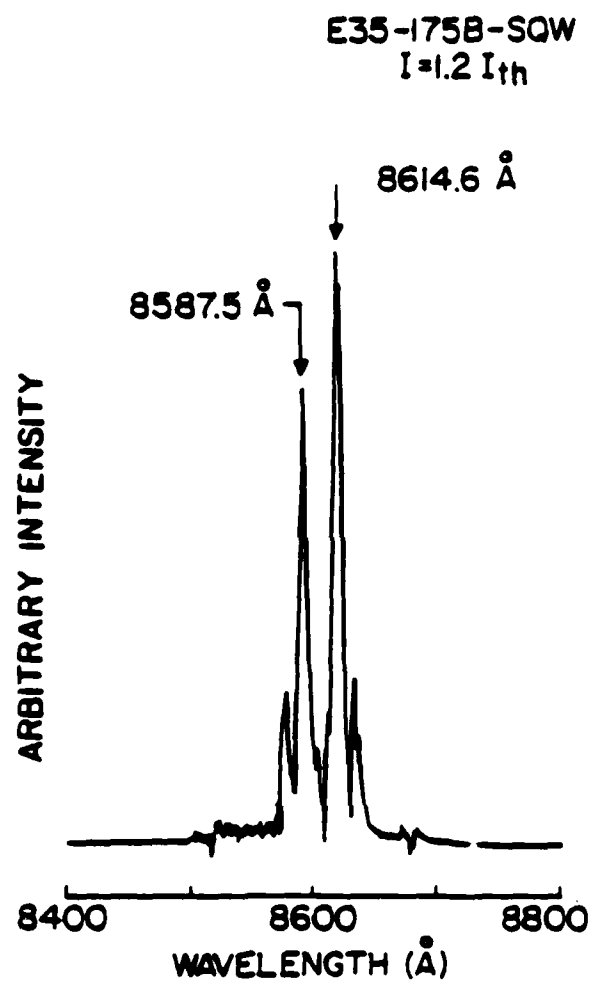
Figure 5.8: The lasing spectrum of a single quantum well laser device.

operate in a single longitudinal mode. Examples of such structures include the DFB laser structures [102,103] and the C^3 laser configuration [104].

The existence of multi-longitudinal modes in phase-locked laser arrays further complicates the problem of achieving single-lobed far-field emission patterns. Since the far-field pattern is essentially a Fourier transform of the near-field, this means that each longitudinal mode (wavelength) of oscillation will give its own unique transform with a different intensity. The result in the far-field pattern is a complicated emission lobe. We purse this point further in the next section.

5.4   Near- and Far-Field Radiation Patterns

The radiation characteristics of multiple element lasers are studied by examining the near- and far-field patterns. The near- and far-field regions of radiation are defined respectively, as the regions in space where the Fresnel and Fraunhofer diffraction regimes are in force [112]. Quantitatively, the demarkation line between the two regions is usually taken to be the line at the distance $z \simeq 2W^2/\lambda_o$, where W is the width of the total emitting aperture and λ_o is the free space wavelength of the radiated light. To be specific, this means that the near-field is between the emitting facet and the distance $z \leq 2W^2/\lambda_o$. The far-field is at any distance beyond $2W^2/\lambda_o$. The far-field diffraction regime is simpler to treat mathematically. This is because at distances many times the wavelength of propagation, the light waves can be ragarded as plane waves.

The technique we use to observe the near-field involves the use of an appropriate microscope objective to image the laser facet onto an infrared vidicon camera. The image of the emitting facet is then displayed on a TV monitor. We show in Fig. 5.9 the near-field image of an M^2PL

laser array just below the lasing threshold. One can clearly resolve and identify the individual lasing elements of this array. In this case, there are seven emitting spots corresponding to our standard 7-element array. The nonuniform transverse extent of the image is an artifact of the imaging optics.

The definition of the lasing facet into seven emitting elements as evidenced in this infrared vidicon image proves two very important points. First, despite the existence of the mode-mixing region where the light is unguided, the overall laser structure provides sufficient wave guidance in the waveguides to assure discrete, coupled element operation. Secondly, we have demonstrated that the Schottky barrier scheme (the details of which are covered in Appendix B) of current confinement to the guides works. By observing the infra-red vidicon image as the bias current of the device is increased, one can also monitor the onset of the lasing threshold. We have already alluded to this fact in an earlier section.

The experimental arrangement we use to measure the far-field radiation pattern is shown schematically in Fig. 5.10. The concept is self-explanatory for the most part. The distance between the laser facet and the light-collecting end of the optical fibre is at least 1 cm (the absolute minimum distance possible with our experimental set-up is 7.0 mm). This distance represents a compromise between the ease of optical alignement of the elements involved and the level of signal detected. In any case, the distance satisfies the far-field diffraction criterion. With a fiber core diameter of 50 μm, a resolution of 0.4° and better can be achieved.

We display in the next three illustations, the variety- of the far-field patterns exhibited by the M^{2}PL lasers. Fig. 5.11 shows the narrowest far-field pattern obtained for the M^{2}PL lasers. This pattern is obtained a little above threshold ($1.2I_{th}$). The overall pattern is an overlap of two unresolved

Figure 5.9: A near-field image of a phase-locked laser array below lasing threshold as observed with an infra-red vidicon camera.

peaks. Its width is ~ 2.1° wide at the half-maximum intensity point. This width is not diffraction-limited. By a diffraction-limited width we mean that the angular spread of the beam at the half-maximum intensity point is approximately given by the free space wavelength of propagation divided by the effective width of the emitting aperture. The theoretical diffraction-limited width for these devices is about 1.1°. For the theoretical calculation, we have taken the free space wavelength emitted by the array to be 0.86 μm and the effective width of the emitting aperture to be 45 μm. The effective width for this calculation is simply the total widths of the 7 waveguides and their interguide spacing.

We show, in Fig. 5.12, the evolution of the far-field pattern as a function of increasing bias current. The next illustration, Fig. 5.13, also shows similar characteristics for a different device. Both these figures manifest two singular properties of the M^{2}PL lasers. We observe that at low bias currents, the far-field patterns do not possess "clean" single lobes. In addition to the major lobe, each pattern has some minor structures to it. The second observation is that with increasing bias current, the pattern definitely evolves into a single lobe. Accompanied with this evolution, however, is a mechanism that tends to broaden the angular spread of the far-field intensity pattern.

In Chapter 4, we introduced the notion of *collective coherence* for laser arrays. In this section, we suggest that *partial* collective coherence may be responsible for the experimental observations discussed above. By this is meant an occurence where not all the array elements maintain the same relative phase amongst themselves. It is postulated that a few of them could have a slightly different phase from the others. This difference would be sufficiently small so that for the most part, the array is still phase-locked. It is then only a degree of the collective coherence that is in question. In
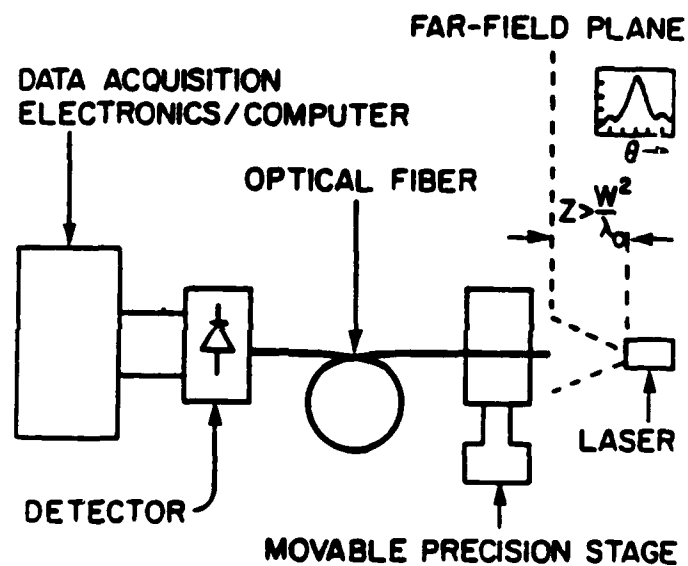
Figure 5.10: The experimental apparatus used for the measurement of the far-field radiation pattern.
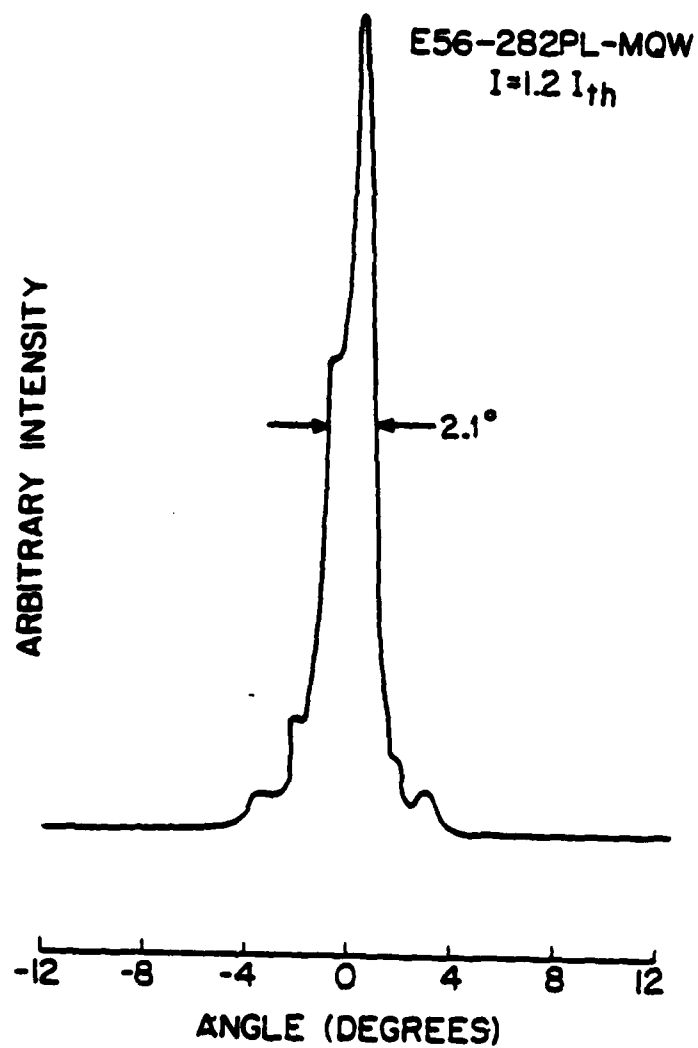
Figure 5.11: A far-field radiation pattern of a mixed-mode phase-locked laser array.

this case, the array is said to have partial collective coherence. When one has full collective coherence, the far-field pattern should look better than what shown in Fig. 5.11, that is to say, with only one narrow lobe.

As a consequence of the foregoing discussion, it is natural to wonder about the origin of the partial collective coherence. There are several considerations that could lead to this state of affairs. The two most likely ones are: perturbations in the longitudinal path of the propagating wave, and an incorrect length for the mode-mixing region. Both the perturbation and the incorrect length could cause a wave in a particular guide to acquire an incommensurate relative phase. Another consideration would also be a possible element-to-element variation of the field amplitudes. The implications of such a variation are discussed in the analytic model developed in the next section.

For all the M^2PL laser arrays characterized, most of them showed far-field intensity patterns similar to those illustrated in Fig. 5.12 and 5.13. In some instances, the amplitudes of the side structures on the envelope of the major lobe were somewhat more pronounced than what is shown here. In no case, however, was the distinct two-lobed pattern [106] characteristic of the usual parallel-array guides observed. The two-lobed far-field pattern has been attributed to an array operating with a π radian phase-shift between its neighboring elements. This interpretation has recently been given credence by the coupled-mode theory [107,108]. We point out that this theory is a passive waveguide theory for weakly coupled guides. It predicts a multiplicity of allowed modes of operation and makes no provision for determining which of the possible modes will actually be excited. The appeal in this theory lies in the relative ease with which closed-form solutions can be obtained. The approximations (of weak coupling) that have to be made in deriving the basic equations might not be valid for the M^2PL
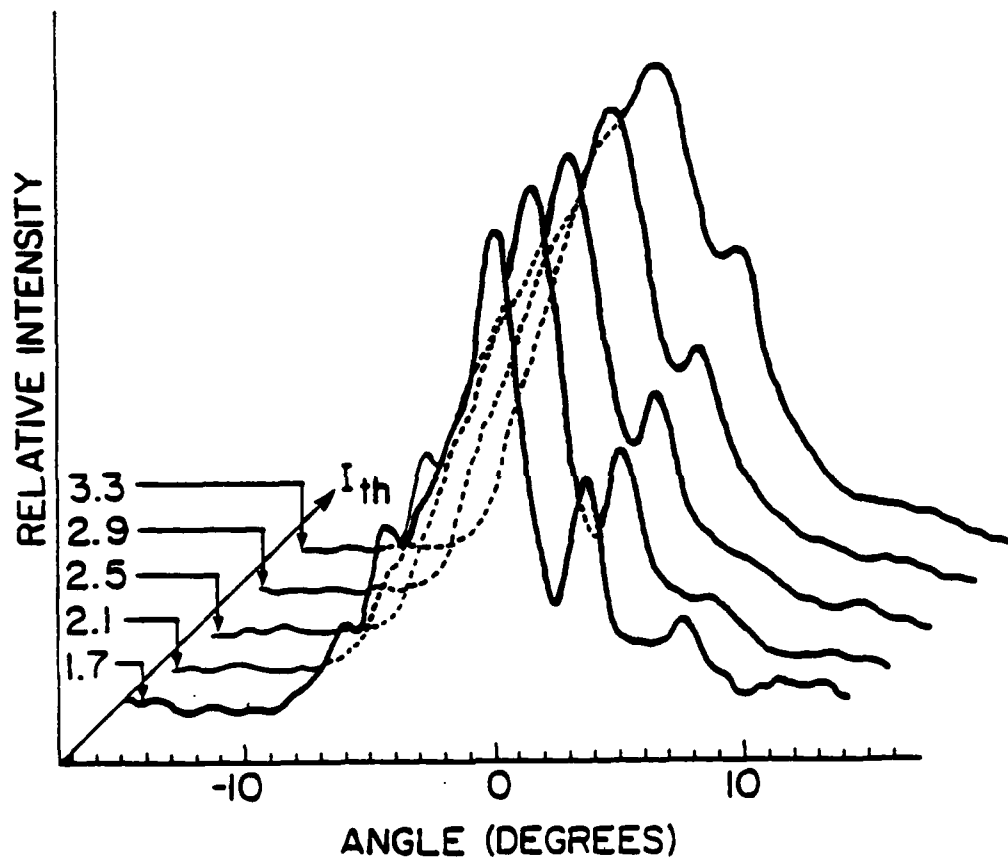
Figure 5.12: Evolution of the far-field pattern of a mixed-mode phase-locked laser array as a function of pumping current.
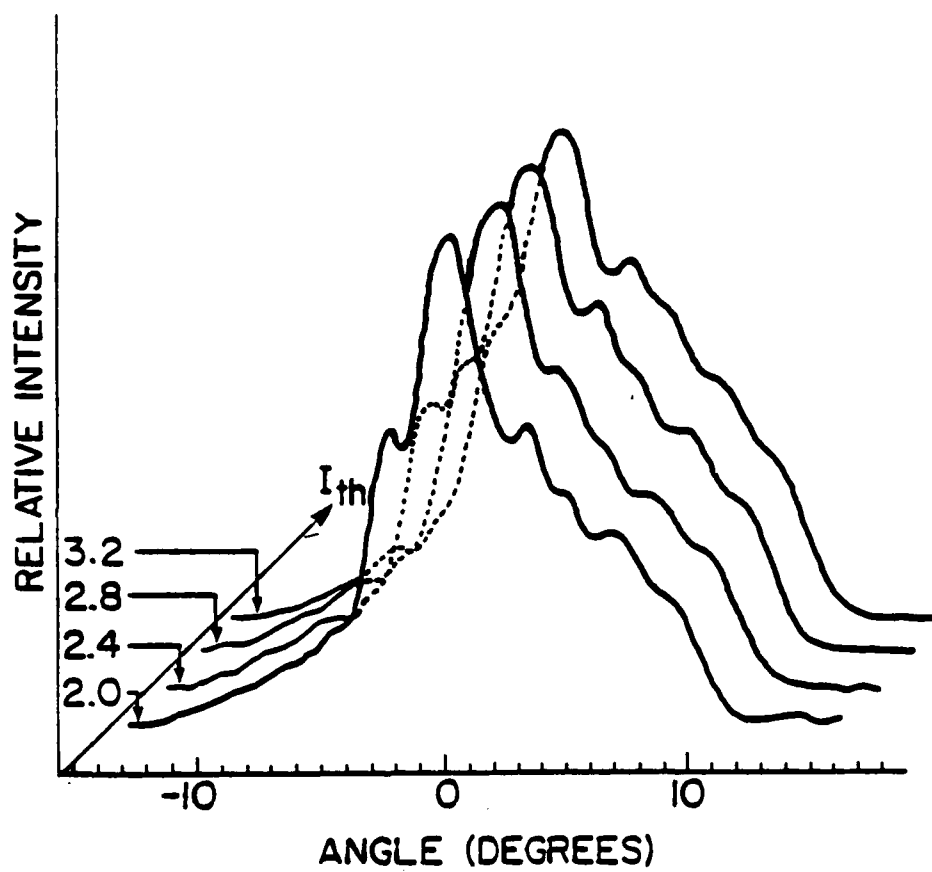
Figure 5.13: Evolution the far-field pattern as a function of pumping current for another device.

lasers because of the relatively strong coupling in these devices.

5.5 An Empirical Model of the Far-Field

In Chapter 4 we discussed the conditions for phase-locking in both evanes-cently-coupled laser arrays and in the diffraction-coupled M^2PL laser arrays. For the most part, ideal conditions were assumed. It was assumed, for example, that all the array elements emitted with uniform field amplitudes and with the same relative phase. The inevitable theoretical conclusion reached with such a premise is that for N phase-locked laser elements, the far-field intensity pattern is directed into a "clean", narrow, single lobe beam. The experimental results presented and discussed in the last section, however, do not support this theoretical premise.

In this section we seek to develop a model which explains our exper-imental measurements of the far-field patterns. The assumptions used in this model are abstracted from experimental observations of both the near- and far-field patterns. In the observations of the near-field patterns with an infra-red vidicon camera, it was often found that there was an intensity variation from element-to-element across the array in some of the devices. This fact has been mentioned in an earlier section of this chapter. For de-vices that showed significant intensity non-uniformity across the array in their near-fields, it was found that the far-fields were complicated and and often exhibited several peaks. This observation then supports a hypothesis that the non-uniform intensity distribution contributes to the multi-lobed far-field patterns.

In the model to be developed here, we shall assume that: (1) each array element *is* an extended source and not a point source, (2) the field distribution across an element peaks at the center and tapers to zero at

the edges, (3) the peak field amplitude may vary from element to element, (4) the field in each element has a phase which may vary across the spatial extend of the element and (5) the element-to-element phase variations do not have to be the same.

With the foregoing considerations, the field distribution across the aperture of a single element, $E_l(x)$, may be expressed as

$$E_l(x) = E_{0l} f_l(x) e^{-j\varphi_l(x)} \qquad (5.10)$$

where E_{0l} is the peak amplitude, $f_l(x)$ is the spatial dependence of the field distribution and $\varphi_l(x)$ is the phase as a function of space. For an array of N elements, the total near-field distribution is given by

$$E(x) = \sum_{l=1}^{N} [E_l(x) * u_0(x - l\tilde{s})] \qquad (5.11)$$

where $u_0(x - l\tilde{s})$ is the impulse (delta) function and $\tilde{s}$ is the inter-element center-to-center spacing. Eq. (5.11) expresses the convolution of the single element field with an impulse function. This is a mathematical way of stating the fact that the field distribution is periodic across the entire array facet. Before proceeding, we define a spatial frequency $u = k_o \sin \theta$. This parameter is related to the parameter δ defined in Chapter 4 as $\delta = k_o \tilde{s} \sin \theta$. This relationship is expressed as $\delta = \tilde{s}u$.

The far-field pattern is related to the near-field by the Fourier transform integral. From the fundamental properties of Fourier transforms in linear system theory [109,110], we can transform the near-field in Eq. (5.11) into the far-field. This operation yields

$$E(u) = \sum_{l} e^{-ju l \tilde{s}} E_l(u) \qquad (5.12)$$

where

$$E_l(u) = \int_{-\infty}^{+\infty} E_l(x) e^{jux} dx \qquad (5.13)$$

For simplicity, we shall assume that the near-field distribution of a single element of the array is Gaussian with a linear phase variation. Thus

$$E_l(x) = E_{0l} e^{-(x/w_{0l})^2} e^{-j\varphi_{0l}x} \qquad (5.14)$$

where w_{0l} is the Gaussian beam radius and φ_{0l} is the phase per unit length in the l-th element. This assumption is consistent with experimental observations and measurements of the near- and far-field patterns of single stripe lasers [111]. Substituting Eq. (5.14) into Eq. (5.13), we obtain the Fourier transform of the near-field for the l-th element:

$$E_l(u) = E_{0l} w_{0l} \sqrt{\pi} e^{-(u-\varphi_{0l})^2 (w_{0l}/2)^2} \qquad (5.15)$$

This distibution is the far-field pattern of the l-th element. The far-field intensity pattern of the entire array of N elements is given by

$$I(u) = |E(u)|^2 \qquad (5.16)$$

Substituting Eq. (5.15) into Eq. (5.12) and using it in Eq. (5.16) we get

$$I(u) = \sum_l I_{0l} + 2 \sum_{l<m} \sum_m \sqrt{I_{0l} I_{0m}} \cos \vartheta_{lm} \qquad (5.17)$$

where

$$I_{0l} = \left[(E_{0l} w_{0l} \sqrt{\pi}) e^{-(u-\varphi_{0l})^2 (w_{0l}/2)^2} \right]^2 \qquad (5.18)$$

$$I_{0m} = \left[(E_{0m} w_{0m} \sqrt{\pi}) e^{-(u-\varphi_{0m})^2 (w_{0m}/2)^2} \right]^2 \qquad (5.19)$$

and

$$\vartheta_{lm} = (m - l)u\tilde{s} - (\varphi_{0l} + \varphi_{0m})\tilde{s} \qquad (5.20)$$

Eq. (5.17) is the general formal expression for the far-field intensity pattern of an array.[1] This equation has a multitude of free parameters. In order to get some insight into how the far-field pattern varies with field amplitude and phase, we specialize the expression into the case of only two phase-locked laser elements. For this case the expression simplifies to

$$I(u) = I_{00} + I_{01} + 2\sqrt{I_{00}I_{01}} \cos\left[u\tilde{s} - (\varphi_{00} + \varphi_{01})\tilde{s}\right] \qquad (5.21)$$

where

$$I_{00} = \left[E_{00}w_{00}\sqrt{\pi}e^{-(u-\varphi_{00})^2(w_{00}/2)^2}\right]^2 \qquad (5.22)$$

and

$$I_{01} = \left[E_{01}w_{01}\sqrt{\pi}e^{-(u-\varphi_{01})^2(w_{01}/2)^2}\right]^2 \qquad (5.23)$$

Eq. (5.21) is simple enough that the effect of varying the amplitude or the phase of one or both of the laser elements can be studied graphically by plotting the resulting intensity as a function of the observation angle. Recall that $u = k_o \sin\theta$ and $k_o = 2\pi/\lambda_o$, where λ_o is the wavelength of propagation in free space.

A computer program which handles the changes possible in the amplitude and phase in the two laser elements has been developed. For the Gaussian field distributions, each field amplitude has a corresponding beam waist, $2w_{0l}$. In Fig. 5.14, we illustrate the far-field intensity pattern of two lasers that are slightly off the in-phase condition for phase-locking. The

---

[1] We have ingored some multiplicative factors which should be included in this expression. These factors, however, do not change the general features of the far-field pattern. See Ref.[112] for details.
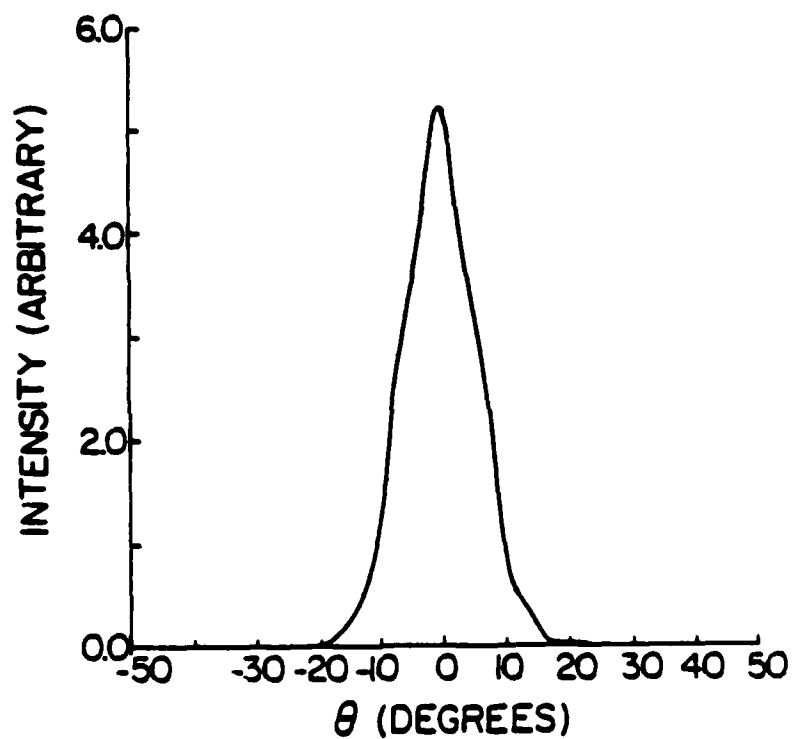
Figure 5.14: A theoretical simulation of the effect of a non-commensurate variable phase on the far-field radiation pattern of two nominally phase-locked laser devices. The two devices are initially slightly off the in-phase locking condition.

next illustration, Fig. 5.15, shows the effect of changing the amplitude (and the corresponding beam waist) of one of the lasers and also violating the phase-locking condition. The illustrations we have presented here were intentionally made to simulate the far-field patterns we observed in our experimental results. It is possible to simulate any desired pattern using the code derived from Eq. (5.21). The substructures exhibited by the experimental result of Fig. 5.12 are remarkably reproduced by our simulations using the model developed here (cf. Fig. 5.12 and Fig. 5.15). This fact is strong evidence for the validity of the model.

We have also studied, analytically, the effects of large phase deviations from the phase-locking condition. We find that in general, the larger the deviation, the more pronounced the side peaks are on the intensity pattern. One can also scan the pattern away from the array center by appropriately selecting the phases. This is a property well known to radar designers. In fact, the techniques of intentional amplitude and phase variations are well established in that field [113]. Fenner and Kingsley [114] have previously used the argument of variable amplitudes to explain the far-field intensity patterns from filamentary emission in GaAs broad area lasers.

This analysis suggests that the peak amplitudes of the lasers in an array *can* indeed vary from element to element. This is not a desirable feature for phase-locked operation. It is therefore important to design the array elements such that the same constant peak amplitude is maintained by each member. Adverse conditions that could lead to the element-to-element field amplitude variation include: non-uniform electrial pumping of the guides and perturbations in the laser facets. These situations can be avoided by careful attention to the fabrication process. The amplitude variations of the fields in each element could also arise from the different longitudinal modes emitted by the element. Each oscillation mode would lead to a different
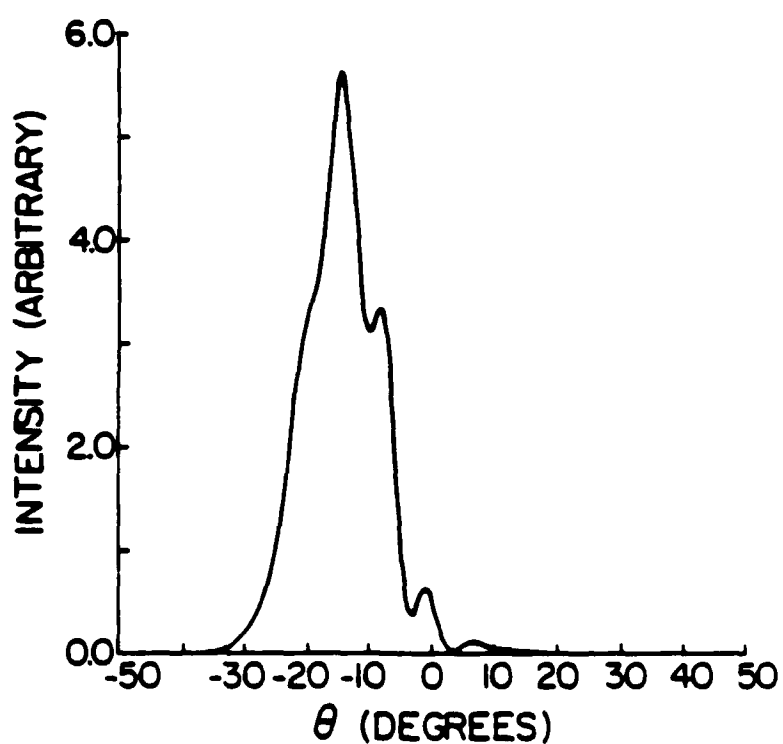
Figure 5.15: The effects of unequal amplitudes on the far-field radiation pattern of two lasers that are initially slightly off the in-phase locking condition. This illustration is generated from the model calculation.

intensity and if the modes are uniformly distributed across the the array, the effective amplitudes would also vary. This is a much more difficult problem to solve. Techniques to restrict the longitudinal oscillations to a single mode (frequency) would have to be developed for the array geometry.

The conclusion of this section is that, contrary to previous assumptions, the amplitudes of most (if not all) array elements can vary and that they are just as important as the phases in determining the overall array pattern. Any theoretical model developed for realistic phase-locked laser arrays must therefore address the issues raised by the experimental observations which led to the empirical model used in interpreting the results presented here.

Chapter 6

Conclusion

6.1 Summary of Results

This thesis has presented the experimental study of quantum well het-
erostructures in the III-V compound semiconductor system of (Al,Ga)As/-
GaAs. This study was conducted with a view to applying these structures
in heterostructure lasers; specifically, phase-locked laser arrays.

It was demonstrated, experimentally, that under the appropriate crys-
tal growth conditions (by the technique of molecular beam epitaxy), single
and multiple quantum well structures grown with superlattice buffer layers
exhibit better optical properties than those grown without these buffers.
Photoluminescence emission spectra of these samples showed well-resolved
structure due to radiative recombination from the first confined electron
state in the conduction sub-band to the first confined heavy hole state in
the valence sub-band ($1e \rightarrow 1hh$). The electron to light hole ($1e \rightarrow 1lh$)
transition was also clearly resolvable. The high photoluminescent efficiency
and the narrow spectral spread at room temperature are evidence of high
quality material. Further evidence was provided by the broad area lasers
fabricated from the quantum well heterostructures. These lasers exhib-

143

ited low threshold current densities. The lowest value measured was ~200 A/cm². This value compares very well with the state-of-the-art values reported in the literature for lasers of similar construction. Theoretical calculations of the gain and threshold current densities predict the low values measured experimentally. The calculations are based on a simple k-selection model.

The single most important contribution of this thesis was the development of the mixed-mode phase-locking (M²PL) laser structure. This novel structure is a member of a class of diffraction-coupled phase-locking structures. Phase-locking is achieved through coupling by diffraction in a region where the electromagnetic waves are unguided. The light propagates in parallel-element waveguides on either side of the mode-mixing region. The length of the mode-mixing region is pre-determined for the condition of in-phase locking amongst adjacent waveguides. It is then defined accurately by lithography.

The new structure consistently exhibited a far-field pattern which is directed into a single major lobe. The device showed no evidence for the dual-lobed far-field pattern seen, for example, in evanescently-coupled arrays. The development of a structure favoring emission in a single-lobed far-field pattern was a major objective of this effort and the results presented here demonstrate the validity of the M²PL design concept toward this end.

An empirical model which explains our observations of the far-field patterns has been developed. The success of this model depends on making assumptions with experimental basis.

6.2   Possible Future Work

A very interesting and useful future project would be to develop a single mode (frequency) M^2PL laser by perhaps incorporating a grating in the active layer. The grating structure could be similar to that used in the distributed feedback lasers. Of course this would raise the issue of the effects of the grating on the quantum well microstructures. Techniques on how best to incorporate it without affecting the pristine crystalline order required for the quantum size effect would have to be developed. An alternative would be to use standard double heterostructures for the lasers.

This thesis introduced the concept of "collective coherence" as applied to the whole phase-locked array of lasers. It would be very useful if this concept could be quantified so that one would speak of a "degree of collective coherence" as a measure of quality for these devices.

Experimentally, a series of structures with a systematic variation in the mode-mixing lengths need to be studied to determine the most optimal length which would give a diffraction-limited far-field beam. While conducting this study, one could also use the M^2PL laser guides as ordinary passive waveguides to measure the coupling coefficients. This measurement would give a crude estimate of the coupling lengths in this structure since it would be performed under passive conditions. Such estimates would provide data to guide further theoretical investigations.

Another interesting experiment to perform on these devices would be to injection-lock them. The effects of the injection-locking wavelength on the far-field pattern could yield potentially useful information for the theoretical studies of these devices specially if the far-field patterns are spectrally resolved to determine the modal contributions to the overall pattern. The spectrally resolved far-field measurements could also be done in their own

right without the injection-locking.

Appendix A

Confinement Factor

The transverse field component of the waveguide formed by the graded index region of the laser structure (see Figs. 3.1 and 3.2) satisfies the one-dimensional scalar wave equation

$$\left[\frac{d^2}{dy^2} + k_o^2 \epsilon(y)\right] E(y) = 0 \tag{A.1}$$

where

$$\epsilon(y) = n^2(y) = \epsilon_o[1 - (y/y_o)^2] \tag{A.2}$$

$\epsilon(y)$ is the dielectric constant which is the square of the index of refraction. The normalized fundamental field solution of this equation is a Gaussian which we take to be

$$E_o(y) = (1/w_o)^{1/2}(1/2\pi)^{1/4}e^{-(y/2w_o)^2} \tag{A.3}$$

The electric field, as written above, is normalized such that the total integrated power flow in the active region along the y-direction is 1 Watt. The parameter w_0 is the Gaussian beam radius given by $w_0 = (\lambda y_o/\pi n_o)^{1/2}$. y_o is the confocal parameter and can be estimated from the actual index (dielectric) profile used in the graded waveguide region. We use Eq. (A.2)

to calculate y_o and then compute the Gaussian beam radius. For the thicknesses of the active layers and the waveguide regions we deal with here, w_o is on the order of the total thickness of the transverse waveguide.

The computation of the confinement factor involves the derivation of the relations that follow. Basically, we seek to calculate the field intensity, I_0, which is the integral of the square of the field given in Eq. (A.3). The fraction of the field intensity, Γ, which propagates in the active region of the quantum well is the quantity of interest.

$$I_0 = \int_0^{L_w} E_0^2(y)dy = \frac{1}{w_0}\left(\frac{1}{2\pi}\right)^{1/2}\int_0^{L_w} e^{-(y/\sqrt{2}w_n)^2}dy = \frac{1}{w_0}(\frac{1}{2\pi})^{1/2}J_0(y)$$
(A.4)

where

$$J_0(y) = \int_o^{L_w} e^{-(y/\sqrt{2}w_n)^2}dy$$
(A.5)

and L_w is the thickness of the quantum well.

After converting to polar coordinates, we get

$$J_0^2 = \int_0^{\pi/2} d\theta \int_0^{\sqrt{2}L_w} e^{-(1/\sqrt{2}w_n)^2 r^2}r\,dr$$
(A.6)

So

$$I_0 \simeq \frac{L_w}{2w_0}$$
(A.7)

And finally, the confinement factor, Γ, is given by

$$\Gamma = \frac{\int_{-L_w/2}^{L_w/2} E_0^2(y)dy}{\int_{-\infty}^{+\infty} E_0^2(y)dy} \simeq \frac{L_w}{2w_0}$$
(A.8)

Appendix B

A Technological Appendix

This appendix, which in some respect, is the backbone of the thesis, discusses the process of crystal synthesis by the technique of molecular beam epitaxy. The components that make up the system are described and their use explained. We then next describe sample preparation before growth and the growth process itself. The last half of the appendix describes the technology of fabricating lasers out of the mbe-grown crystals. This technology is what has been developed for the facilities available for this kind of work at MIT.

B.1 The Molecular Beam Epitaxy Process

In recent years, the crystal growth technique of molecular beam epitaxy has emerged as a leading method of preparing thin, high purity semiconductor layers of extremely uniform composition. The process itself is akin to previous vacuum evaporation methods. It owes its name, however, to the fact that crystal growth is achieved in an ultra-high vacuum enviroment through the chemical reaction of multiple molecular beams of differing flux densities with a heated monocrystalline substrate.

149

The general topic of molecular beam epitaxy (MBE) of compound semi-conductors is very broad [115,116]. We will therefore confine ourselves here only to those aspects of the process that relate directly to the growth of the (Al,Ga)As/GaAs system. The general features of the method for this semiconductor are very similar to those of the other III-V compound semi-conductors. The MBE process in its most generic form for the growth of (Al,Ga)As is illustrated in Fig. B.1. The components shown in the illustration are enclosed in an ultra-high vacuum system. Inside each furnace is a crucible which contains the constituent chemical element (in solid form) of the desired film. The temperature of each furnace can be controlled to give a vapor pressure of the material inside its crucible that is sufficiently high to generate molecular beams by free evaporation. The furnaces are so arranged that the central portion of each molecular beam strikes the surface of the substrate. Epitaxial growth is achieved on the substrate by choosing the appropriate substrate and source material temperatures. By interposing shutters between the substrate and each furnace, control over the growth process can be achieved.

The growth kinetics of compound III-V semiconductors are complex and it is not at once obvious that a means of growing stochiometric material exists. However, fundamental studies of the adsorption-desorption process by Arthur [117] demonstrated that stochiometric growth of the III-V compound semiconductors can be achieved by a control of the group III element as long as there is an excess of the group V species in the growth enviroment. The growth rate is therefore determined by the arrival rate of the group III element. By appropriately controlling the temperature, the arrival rate of these atoms can be slowed down considerably to achieve extremely low growth rates which are necessary for monolayer resolution.
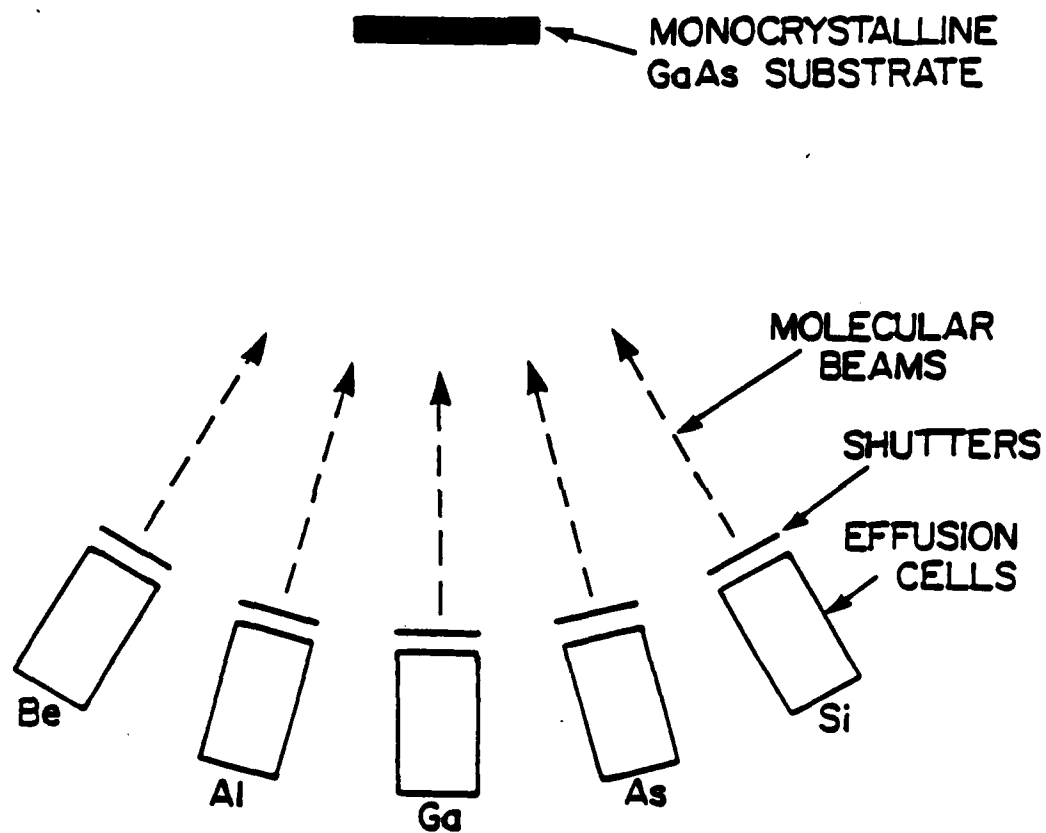
Figure B.1: A schematic illustration of the molecular beam epitaxy process.

B.1.1 The MBE System

The practical implementation of the MBE process is considerably more complex than Fig. B.1 would lead one to believe. Fig. B.2 shows the system at MIT and is composed of various components which we describe below. The ultra-high vacuum system is comprised of two main chambers. The first chamber is the load-lock exchange chamber. This houses the Auger analytical gun and the relevant optics that go with it. The Auger is primarily used to study techniques for obtaining oxygen- and carbon-free substrate surface prior to epitaxy. The load-lock is also used for degassing the substrates before introduction into the epitaxy chamber. The load-lock exchange chamber is continuously pumped with a titanium sublimation pump and an an ion pump after it has been roughed down by a mechanical and a sorption pump. The second chamber is the epitaxy chamber. This chamber is bigger and has most of components necessary for epitaxy. The minimum of components required here include:

- A system of pumps to evacuate the chamber.

- Multiple furnaces (with crucibles inside them).

- Furnace shutters.

- Furnace baffles for liquid nitrogen.

- A flux gauge.

- A heated substrate holder.

- Epitaxy control instrumentation.

- A HEED gun for substrate surface studies.
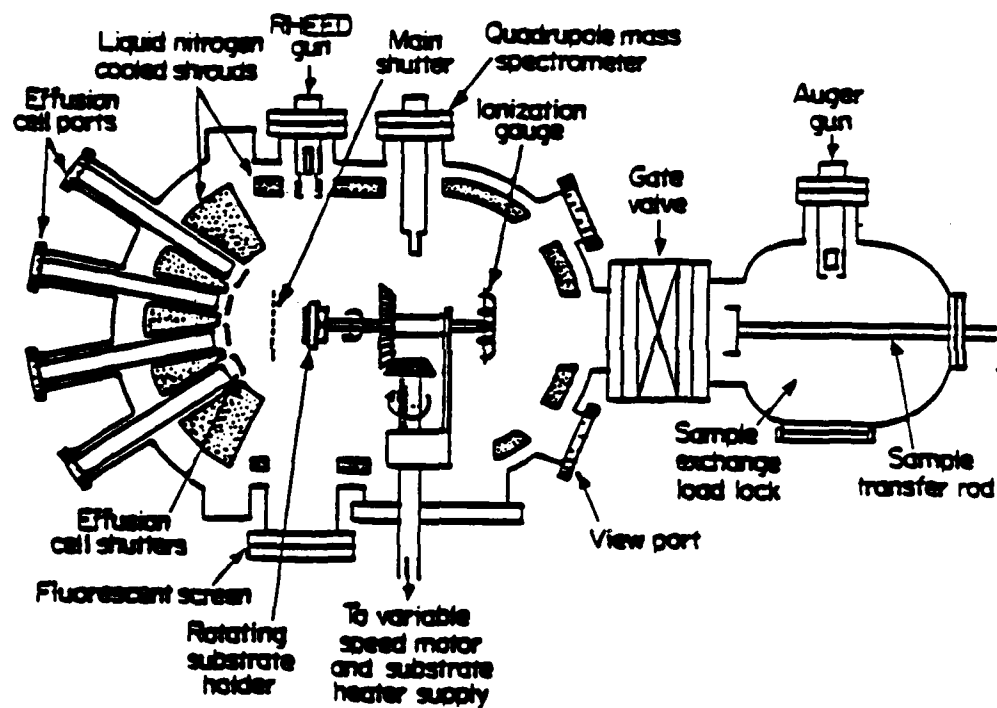
Figure B.2: An illustration of the MBE system at MIT used in this work (after Instruments SA/ Riber MBE Division).

- An infra-red optical pyrometer for substrate temperature monitoring.

- A mass quadrupole spectrometer.

In the next few sections, we outline the necessity of having these components in the growth chamber.

B.1.2 The Ultra-high Vacuum System

The need for the ultra-high vacuum system stems from the low growth rates typical of the MBE process and also because in general, the grown films are required to have negligible unintentional impurity levels. The base pressures routinely achieved in the system at MIT are in the low 10^{-10} to mid 10^{-11} Torr range (this was true at the time of writing but things have since gotten worse). These pressures increase somewhat during deposition to the 10^{-6}-10^{-5} Torr range. Under these conditions, the excellent wafers produced by the MBE process also owe their purity to the fact that the unwanted residual gas species have very low sticking coefficients. The design of an MBE system also focuses on minimizing total background pressure, thus eliminating unwanted gas species with high sticking coefficients.

After the system has been baked out at 250° C (including the source materials) for an extended period of time (8-24 hours) to accelerate outgassing, pumping is achieved by a combination of pumps. The rough pumping prior to the baking is done by a mechanical vane pump aided by liquid nitrogen cooled sorption pumps. To attain ultra-high vacuum conditions, a titanium sublimation pump in conjunction with a sputter ion pump and a closed-cycle helium cryo-pump are employed. To maintain the ultra-high vacuum conditions, the growth chamber is very seldom open to the atmosphere. The sample transfer is done through a load-lock which makes it unneces-

sary to ever open up the growth chamber to the atmosphere, except during source reloading and system repair.

B.1.3   The Furnaces, Shutters and Baffles

During evaporation, the intensity of the molecular beams arriving at the substrate is determined by the vapor pressures of the source materials and to a lesser extent, by the geometry of the crucible and the line-of-sight distance from it to the substrate. If the crucible is of a Knudsen type [118,119] with a diameter of $2r$, the flux density incident on the substrate i.e. the number of atoms (molecules) arriving per unit area per unit time is given by

$$F = \frac{\pi r^2 P(T) A(\theta) N}{\sqrt{2\pi MRT}} \tag{B.1}$$

where $P(T)$ is the pressure in the crucible, πr^2 is the area of the crucible aperture, $A(\theta)$ represents the angular distribution of the flux for different angles measured from the crucible axis, N is Avogadro's number, M is the element molecular weight, R is the universal gas constant and T is the temperature in degrees Kelvin. For a line-of-sight distribution $\theta = 0$ ($\Rightarrow A(\theta) = 1$), and if the distance from the aperture to the substrate is l, after substitution of the known numerical values for the other constants, Eq. (B.1) becomes

$$\Gamma = 1.11 \times 10^{22} \frac{\pi r^2 P(T)}{l^2 \sqrt{MT}} \tag{B.2}$$

where Γ represents the number of atoms (molecules) arriving at the substrate per second per unit area. The relationship between the pressure and the temperature has been found empirically to obey the rule

$$\log P(T) = \frac{A}{T} + B \log T - C \qquad (B.3)$$

where A, B and C are constants specific for a given element. Using the data of Honig and Kramer [120], we find that for Ga

$$P(T) = 10^{\{-\frac{11021.2}{T} + 7 \log T - 15.42\}} \qquad (B.4)$$

For the Riber system we have at MIT, $l = 12$ cm, $2r = 2.5$ cm. The typical Ga temperature we use is about 945° C (or 1218 K). This value gives a pressure of $P = 1.35 \times 10^{-3}$ Torr. The corresponding molecular flux arriving at the substrate as given by Eq. (B.2) is 1.75×10^{15} Ga atoms cm^{-2} sec^{-1}. From our actual growth rate measurements, this arrival rate corresponds to a growth rate of $\sim 1\mu m/hr$ of GaAs for a substrate temperature of $< 640°$ C.

The furnaces in our MBE system are resistively heated with direct current power supplies. Each furnace is mounted on its own vacuum flange which contains the heater and a tungsten-rhenium alloy thermocouple which makes a physical contact with the crucible. The crucibles are made of pyrolytic boron nitride (PBN).

There are multiple radiation shields designed into each furnace to improve the temperature uniformity and the thermal efficiency of the heaters. These shields also serve the dual role of preventing the heating and subsequent outgassing of the reactor system walls. Other measures taken to prevent chemical cross-contamination and to minimize thermal radiation heating of the system walls include baffling and cryopanelling. During operation, the baffle enclosures are continuously cooled with liquid nitrogen. This has the additional desirable effect of reducing the residual partial pressures of any deleterious gases in the growth chamber.

B.1.4 Epitaxy Control Instrumentation

For reproducible growth, it is important to be able to control the substrate temperature accurately; this control must also be exercised over the molecular beam fluxes. The instrumentation that is generally used involves a thermocouple feedback signal to a rate-proportional controller. The controller decides, depending on the feedback signal, when to increase or decrease the power to either the substrate heater or the furnace of the crucible. For the substrate heater, stability of better than $\pm 1°$ can be routinely obtained.

Control of the molecular beam fluxes is a little bit more complicated. The molecular beam flux emergent from any given crucible tends to depend on how much solid source is left in the crucible. This makes long term reproducibility quite impossible. What is generally done, therefore, is to measure the flux with a nude ion gauge rotated into the substrate position before epitaxy. The value thus measured, is reproducible for several growths before a new re-calibration is necessary. The ion gauge measurement of the flux applies only to the group III and V elemental sources. The dopant sources have such low vapor pressures that the ion gauge is not sensitive enough to register them. Although the control of the molecular beam fluxes is definitely difficult, it is not impossible and excellent lattice-matched epitaxy of InP-based epi-layers can still be grown. The stringent requirements of the flux values required for the InP-based layers just mean that flux measurements have to be carried out before each growth to set the right values for lattice-matching to the InP substrate.

The temperature-related stability of the Ga (or for that matter any group III element) molecular beam flux achievable by the rate-proportional controller can be estimated from Eq. (B.4) as

$$\frac{\Delta P(T)/\Delta T}{P(T)} = 2.3 \left\{ \frac{11021.9}{T^2} + \frac{3.04}{T} \right\} \qquad \text{(B.5)}$$

So for the Ga cell operating at 945°C (1218 K)

$$\frac{\Delta P}{P} = 0.024 \Delta T \qquad \text{(B.6)}$$

Therefore a 1° variation in the temperature will lead to a 2.4% variation in molecular beam flux. Since a temperature stability of less than a degree is achievable, flux stability of better than $\pm 1\%$ is attainable. This in turn translates into excellent control over the composition of films deposited by the MBE process.

B.1.5 The Substrate Holder

In order for the thermal molecular fluxes impinging on the substrate. to be adsorbed and chemically react with it to form an epitaxial layer, the substrate has to be held at the right temperature. This is done by a heated substrate holder. The holder is made of a molybdenum block which has a high thermal conductivity. The block is heated electrically from the back with a flat tantalum sheet. This assures a temperature uniformity across the substrate which is good for reproducibility. The temperature of the block is monitored by a thermocouple mounted in a hole at the back of the block. The substrate is held on the block by indium which is molten at the growth temperature and the substrate is therefore held on by the surface tension effect. During growth, the substrate surface temperatrure can be monitored by use of an infra-red optical pyrometer. The emissivity setting of the pyrometer must be adjusted correctly for the particular window used. This measurement is approximate and is only used as a guideline (don't ever swear by it or the gurus will be mad at you).

B.1.6 The Quadrupole Mass Spectrometer

In modern MBE systems, the mass spectrometer is not an absolutely necessary piece of equipment. If present, however, it can be conveniently used as an element-specific leak detector. Its other use is detection of residual vacuum gases which are inherent to the system and those that are associated with the effusion cell furnaces and the substrate heater. The readings taken by a mass spectrometer are only relative since they depend on so many instrument parameters.

In our work at MIT, the mass spectrometer is only used during the first few days after a system bake-out. The bake-outs are generally carried out after the system vacuum has been broken for source re-charging. During this period, we use it to monitor the level of CO, CO_2 and H_2O and any other residual impurity elements in the system. When the relative levels of these gases have decreased to an acceptable background, then the system is ready for epitaxy.

B.1.7 The High Energy Electron Diffractometer

The high energy electron diffractometer (HEED) is the most useful *in situ* analysis tool available in the MBE ultra-high vacuum enviroment. The method of surface analysis in the context of MBE systems was pioneered by Cho [123]. The arrangement he used and it is the standard today, involves a glancing angle ($\sim 2°$) reflection of electrons. A beam of high energy (3-10 keV) electrons is reflected off a substrate at a glancing angle. The reflected beam then impinges on a phosphor screen where the surface diffraction pattern is observed. This geometry allows the molecular beams to still be able to arrive at the substrate surface unobstructed while simultaneously, the surface diffraction pattern is analyzed.

The diffraction pattern observed before and during epitaxy depends (for the III-V substrates) on the substrate surface orientation and on the azimuth at which the electrons are incident. It also depends on the existing surface conditions; this ultimately means that the substrate temperature is important. During the pre-epitaxy stage, the substrates are generally covered with a native oxide. Before growth can be initiated, this oxide has to be cleaned off. For GaAs and InP substrates, this is done by gradually heating the substrates to slightly above the temperature at which epitaxy is initiated. As the oxide is cleaned off, the HEED pattern undergoes a series of transformations which correspond to the oxide desorption process. In order to prevent evaporation and disintegration of the substrate, an As_2 or As_4 overpressure must be maintained over the substrate.

In Fig. B.3 we show HEED patterns with the electron beam along the [110] azimuth from an InP(100) surface. The initial thermal cleaning, done under As_4 overpressure, produces a spotty diffraction pattern, indicating that the substrate is not clean yet. With additional heating, the pattern becomes sharper and fairly well-defined. Finally, when the substrate is clean, i.e. when all the oxide is desorbed, the pattern becomes elongated and additional lines appear between the original diffraction features. This pattern is generally refered to as the $C(2 \times 4)$ surface reconstruction and it is As-stabilized. When the electron beam is along the [$\overline{1}10$] azimuth, a different pattern is observed. For orientations intermediate between the [110] and the [$\overline{1}10$] azimuths, complicated diffraction patterns are observed.

The HEED gun can be left on during the deposition process if it is desired to monitor the evolution of the monolayer growth process. Recently, oscillations of the signal collected from the HEED screen by a light pipe and detected by a photomultiplier tube have been observed [124,125]. These oscillations have been attributed to the process of a monolayer growth. At

the beginning or the end of monolayer coverage, the oscillation is at its peak, and it is at a minimum when just about half a monolayer has been grown [126]. These oscillations have provided another technique for calibrating the growth rates in real time.

The usefulness of the HEED techniques cannot be denied. We have found, however, that during the growth of epi-layers for optical studies, it is best to minimize the time during which the HEED gun is left on. Extended periods of the HEED operation tend to degrade the optical quality of the layers. Our experience in this regard corroborates Cho's findings [127] that the gun may actually introduce contaminants into the enviroment. It is also believed that too high an electron beam current could polymerize any residual hydrocarbon gases; this would result in carbon contamination of subsequent epitaxial layers.

B.1.8   Growth Mechanism

It is generally accepted that crystal growth by molecular beam epitaxy does *not* take place in a thermodynamic equilibrium. The conditions prevailing during the process are such that reactants and products are each at their own temperatures and application of theoretical thermodynamic principles becomes unwieldy. No quantitative models exist for the MBE process. The currently accepted qualitative model was formulated by Foxon *et al.* [128] and it is based on transient response studies conducted by Arthur [117] on the surface chemical processes involved during the growth of GaAs. The importance of Arthur's work lies on the demonstration that the growth of III-V compound films from beams of the elements is kinetically controlled by adsorption of the group V element, while the growth rate is controlled by the arrival rate of the group III element.

As a vehicle for discussing the growth of III-V compounds by molecular
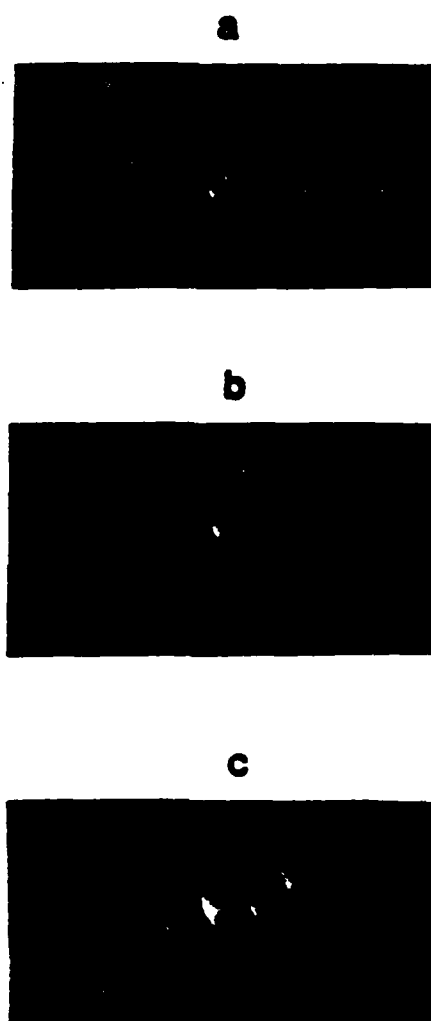
RHEED PATTERNS

a

b

c

Figure B.3: The   in situ oxide desorption process as monitored by HEED diffraction patterns along the [110] azimuth from an InP (100) surface.

beam epitaxy, we use the binary compound of GaAs. During the growth process, the Ga and As populations on the substrate surface depend on both the substrate temperature and the relative fluxes of Ga and As reaching the surface. The Ga is supplied as a monomer by evaporation of the liquid and it has a close to unity sticking coefficient on a GaAs surface over the range of *normal* temperatures used during growth. At high substrate temperatures ($>$ 650°C), such as are required for layers grown for optical studies or optical devices, the Ga has a sticking coefficient of $\sim$ 0.8 or slightly less. The As is usually supplied as a dimer, As_2; or as a tetramer, As_4, from the solid. When the GaAs is grown from Ga and As_2, a first-order dissociative chemisorption reaction occurs. The dimer splits into free As atoms which are adsorbed by the Ga atoms. The sticking coefficient of As_2 is proportional to the arrival rate of the Ga atoms. Any excess As_2 is re-evaporated and therefore stochiometric GaAs is grown. When the GaAs is grown from Ga and As_4, pairs of As_4 molecules react on next-neighbor Ga atoms resulting in a second-order process. That is to say, for any two As_4 molecules, four As atoms are incorporated into the GaAs lattice and another four desorb as an As_4 molecule. The desorption rate of As_4 depends on the adsorption rate at low As coverages. The maximum sticking coefficient of the As_4 tetramer is 0.5. The two different mechanisms of the growth processes involved can influence the properties of the films differently for otherwise identical conditions. It has been found empirically, for example, that GaAs layers grown from Ga and As_2 species have superior optical properties than those grown from Ga and As_4 species for substrate temperatures below 640° [129]. This problem can, however, be remedied by raising the substrate temperature to values above 640°C ($<$ 710°C). At these elevated temperatures, the As_4 dissociates into As_2 so that the favored first-order chemisorption reaction occurs. The disadvantage of the

high substrate temperatures is that the Ga begins to re-evaporate and the growth rate decreases.

With the exception of actual growth details, these then are the models that explain the process of molecular beam epitaxy. Some of the necessary details include considerations like the optimum group V to group III flux ratios needed for particular substrate temperatures. In special cases like during the growth of lattice-matched InP-based epi-layers, the flux ratios of the constituent group III elements needed must be carefully measured and determined for a particular composition. The other important consideration of course is the substrate temperature.

B.1.9   Incorporation of Intentional Dopants

In order to be able to fabricate devices from the epitaxial layers grown by MBE, it is necessary to incorporate impurities which will render the layers either p- or n-type. Normally, intrinsic MBE-grown epitaxial layers are p-type. It has been inferred from low temperature photoluminescence [130] studies that the unintentional dopant is carbon. It is not clear yet whate the origin of the carbon is. But it is thought to be a result of some reaction of the residual carbon monoxide or dioxide. In this respect, it becomes important to reduce the density of any residual carbon-containing species in the chamber.

The intentional impurities that have been used as dopants successfully in the MBE growth process have sticking coefficients that are very close to unity. these dopants include: Si, Ge, Sn, Mn, Ge and Te [115]. The dopants we use in our system are Si and Be. The silicon dopant tends to be an amphoteric impurity in GaAs. However, in MBE-grown layers the Si-donor behavior dominates the compensation process and n-type carrier concentrations of from 10^{16} to 10^{18} cm^{-3} can be routinely obtained. The

Si flux required for the doping process is obtained by a direct sublimation of the solid Si source. The density of Si atoms required for this process is relatively low compared to the densities of Ga and As. The Si flux required is therefore in the low 10^{11} atoms cm^{-2}. This number is so low that the sensitivity of the ion gauge is not high enough to detect it.

For p-type doping, beryllium is used. Like silicon, the sticking coefficient of Be is also unity during the growth of GaAs or (Al,Ga)As. Extremely high doping densities have been reported [131] for suitably adjusted growth conditions. In our laboratory, we can routinely obtain intentional acceptor concentrations in the range of 10^{16} to 6×10^{19} cm^{-3} without deleterious side-effects to the crystal surface morphology.

B.2 Crystal Growth

The process of growing high quality crystals by molecular beam epitaxy is, at the moment, more of an art than a science. The properties of the final layers grown depend on the initial substrate cleaning procedure, the substrate temperature used and the group V to group III element flux ratios. This holds true if the concentration of the residual background gases is negligibly low and the vacuum is ultra-high.

B.2.1 Substrate Preparation

There are many substrate preparation procedures in existence; each is unique to a particular laboratory or individual. We describe here the procedure used at MIT for the preparation of GaAs substrates. The same procedure can be used with a slight modification for InP substrates.

The substrates are usually obtained with one side already chemically polished from the manufacturer. Initially, the substrate is boiled in trichloroethy-

lene for five to ten minutes, it is then rinsed twice in warm acetone and then in methanol. The cleaning in organic solvents is intended to remove any organic contaminants. Before the next sequence of steps which involves cleaning in inorganic solutions, the substrate is rinsed in deionized water. The native oxide covering the substrate surface is removed by etching in HCl for four minutes. This is followed by a quick rinse in deionized water after which the substrate is decanted in concentrated H_2SO_4. A few microns are then etched off the substrate in a solution of $H_2SO_4:H_2O_2:H_2O$ (4:1:1) at room temperature. The actual etching is done for four minutes. The substrate is again rinsed in deionized water for four minutes and then etched in HCl for the same amount of time. Finally, it is rinsed in deionized water to passivate it and blow-dried with filtered nitrogen gas. The last step is to mount the substrate on a preheated molybdenum sample holder with indium solder (this technique is rapidly becoming obsolete and then load it immediately into the MBE system.

B.2.2 The Growth Process

Usually after the substrates have been loaded into the load-lock/preparation chamber, the system is allowed to pump overnight to a base pressure of $\sim 1 \times 10^{-9}$ Torr in the load-lock chamber and $\sim 1 \times 10^{-10}$ Torr in the growth chamber. Before transferring a substrate into the growth chamber, it is outgassed in the load-lock chamber for 30 minutes at 300° C. During this time, the growth chamber cryo-panel is cooled with liquid nitrogen and the sources in the effusion cells are brought up to the desired temperatures.

When the substrate is in the growth chamber, the passivating oxide maybe thermally desorbed under As_2/As_4 overpressure. For GaAs, this desorption occurs between 580°-610° C. The process is monitored by the HEED as explained earlier in Section B.1.7. Epitaxy is immediately initi-

ated once all the oxide is desorbed. In general, 0.5-1.0 μm of GaAs buffer layer is grown first at a low substrate temperature ($< 640°C$). The GaAs buffer layer is followed by a superlattice buffer (SLB) layer. This structure is composed of alternating layers of GaAs/(Al,Ga)As. We find that samples which incorporate the SLB layers have excellent op ical properties. An earlier treatment of SLB layers has already been given in Chapter 2. For the samples grown for this study, subsequent layers were grown at 710°C. Samples grown at this temperature exhibit very high photoluminescence efficiencies. The typical group V to group III element flux ratios used ranged from 8 to 15. These ratios guarantee an As-stabilized surface at the particular substrate temperature chosen.

B.3   Sample Characterization

The details of the techniques of characterization used will not be covered here since they constitute minor (albeit essential) side issues in the context of this thesis. The main techniques used incuded: Hall measurements for the carrier concentration determination, photoluminescence for the radiative efficiency, double crystal x-rays analysis for the mole fraction determination in the (Al,Ga)As layers, SEM for growth rate calibration, thickness determination and surface morphology analysis.

B.4   Laser Fabrication

This section, although relegated to the appendix, should not be regarded as the least important. In many respects, it is the backbone of the thesis. It is intended to answer some of the questions most frequently asked by new-comers into the field of semiconductor lasers, especially those who are

not content to just learn the theory of how these devices work but are also interested in the technology. The procedures we describe here are not necessarily the most optimal but they are the best-suited for the facilities available at MIT at the time this work was done. The steps described below are for the fabrication of lasers that have some lithographic features on them. Broad area lasers maybe fabricated in a similar fashion but with the lithographic steps omitted.

B.4.1 Post-Epitaxy Sample Cleaning

After a sample has been removed from the molybdenum block used to hold it during the MBE growth, the indium solder must be removed from its back. For GaAs, the wafer is glued backside up onto a microscope glass slide with black wax (Apezione Wax) pre-melted on a hot plate. It is then diped into a 1:10 solution of DI-H_2O:HCl at room temperature. When·all the indium has has dissolved, the wafer is rinsed in deionized water and melted off the glass slide. It is then cleaned in warm trichloroethylene, acetone and methanol. Finally, it is rinsed in iso-propyl alcohol and blow dried with pre-filtered nitrogen gas.

If the wafer had been an InP-based semiconductor, then the indium solder cannot be removed in the manner described above because HCl etches InP. The indium must be removed by etching in a solution made of 70 gm of $HgCl_2$ (mercury chloride) and 200 ml of $HCON(CH_3)_2$ (dimethyl formamide).

Before lithography, the wafer must be lapped down on a lapping jig to about 15-18 mils. This is important because the uneven back side must be made smooth and parallel to the front epitaxial layer side.

B.4.2 Photolithography

Before the photoresist is spun on, the wafer must be cleaned again. This time, it is cleaned in buffered HF for two minutes and rinsed in deionized water. It is then blow-dried with pre-filtered nitrogen gas. Now the photolithographic procedures can be started. The mask aligner is a high precision Suss (trade name) aligner. We list the steps below.

1. Dehydrate the wafer at 200° C for 45 seconds.

2. Spin on C-20 primer (manufactured by Kodak) at 6000 rpm for 30 seconds.

3. Spin on photoresist number 3000-26 (manufactured by Kodak) at 6000 rpm for 30 seconds.

4. Softbake (pre-bake) the wafer with the photoresit on it at 90° C for 25 minutes.

5. Align the mask features desired and expose. This step is very critical. Experiments must be done to determine the best exposure time. The exprsure time depends on the lamp energy, lamp life, photoresit type and the soft-baking time.

6. After the exposure, the features maybe developed in developer number 305 (manufactured by Kodak).

7. Assuming the development process is satisfactory, the wafer must be hard-baked now for 30 minutes at 130° C

The final step in the photolithographic procedures is to gently etch ("descum") the wafer in a very low power oxygen plasma. This etching

removes any resist not removed by the 305 developer. Care should be taken not to remove the resist where it is desired as a mask.

B.4.3 Wet Chemical Etching

The ridge waveguide structures on the lasers are chemically etched with the photoresist acting as a mask. The chemical solution used for the etching is a mixture of H_2SO_4:H_2O_2:H_2O (1:8:8) at room temperature. Its etching rate must be determined for the particular (Al,Ga)As composition to be etched. Before etching, the wafer must be rinsed in buffered HF and deionzed water. This is crucial because if the native oxide covering the wafer is not removed, the etching will proceed nonuniformly.

After the etching, the masking photoresist is removed by plasma-etching in oxygen plasma.

B.4.4 Contact Metallization

The p-contact metallization for the devices made in this study consists of titanium, platinum and gold. The reason for the use of these refractory metals is that Schottky barrier contacts can be made at the regions where ohmic contacts are not desired. We will explain the mechanism of this process in a later section.

The preparatory step before metallization is the removal of any oxides on the wafer surface by cleaning in buffered HF and rinsing in deionized water. After blow-drying in filtered nitrogen gas, the wafer is immediately loaded into the E-beam (electron beam) evaporator. The base pressure of the evaporator should be $< 3 \times 10^{-7}$ Torr before the liquid nitrogen trap is filled. Pressures lower than this can be achieved when the trap is cold. The metals evaporated are: 400 Å of Ti, 200 Å of Pt and 3500 Å of Au.

The first layer of Ti deposited adheres well to the semiconductor. It is used as an adhesive ("glue") for the other metals. It also forms a good Schottky barrier to the lightly-doped (Al,Ga)As layer between the ridges. The Pt layer forms a diffusion barrier [132] to prevent the Ti-Au reaction from occuring [133]. The combination of the three metals together forms a good ohmic contact to the heavily-doped GaAs layer. The thicknesses deposited represent a compromise between the ease with which the wafer can be cleaved into individual laser devices and the degree of difficulty in bonding a gold wire to the top Au metal.

B.4.5 The Ohmic and Rectifying Properties of the p-Contact

The metallization on the p-type side of the laser structure performs the dual roles of facilitating the easy flow of current through the ridge waveguides and minimizing its flow between the guides. We describe below the unique properties that make this possible.

The properties of the metal-semiconductor junction depend on the Schottky effect [134,135]. This effect is used to explain what happens when a metal is brought into intimate contact with a semiconductor. The ohmic or rectifying nature of the contact depends on the work functions ϕ_m and ϕ, of the metal and the semiconductor, respectively.

The ohmic and rectifying properties of the p-contact are used for the lateral current confinement in the laser arrays. Lateral current confinement can also be achieved in a variety of ways which involve the use of complicated equipment and procedures [136,137]

B.4.6 The p-Ohmic Contact on the Ridges

The top p-type semiconductor layer onto which the metallization is deposited is a low band gap GaAs layer which is degenerately (highly) doped. For this particular situation, the first contact metal, the Ti, is chosen because its work function ϕ_m, is larger than the GaAs work function, ϕ_s. Fig. B.4 illustrates the situation before and after contact has been made between the metal and the semiconductor. The other parameters defined in the figure are: the energy separation between the vacuum level, χ_s, and the semiconductor conduction band level. This energy is often called the electron affinity. $E_s = E_g + \chi_s$, is the depth of the semiconductor valence band from the vacuum level.

Before contact, the semiconductor Fermi level is above the metal Fermi level by an amount $\phi_m - \phi_s$. After contact, there is a transfer of charge (electrons) from the semiconductor to the metal until equilibrium is established such that positive charge is left on the semiconductor surface and negative charge is formed on the metal side. At this point, the Fermi levels line up. Holes in the semiconductor can readily cross over to the metal and be neutralized by the high concentration of electrons existing there. For a positive voltage applied at the metal, holes formed there can move onto the metal very easily. This contact is therefore ohmic.

B.4.7 Rectifying p-Contact Between the Ridges

Between the ridges is exposed a large band gap, low-doped, p-type (Al,Ga)As layer. In this situation, because of the large band gap, the semiconductor work function ϕ_s, is larger than the Ti metal work fuction, ϕ_m. Before contact, if we assume that all the acceptors are ionized, then the Fermi level of the semiconductor is below that of the metal by an amount $\phi_s - \phi_m$. As
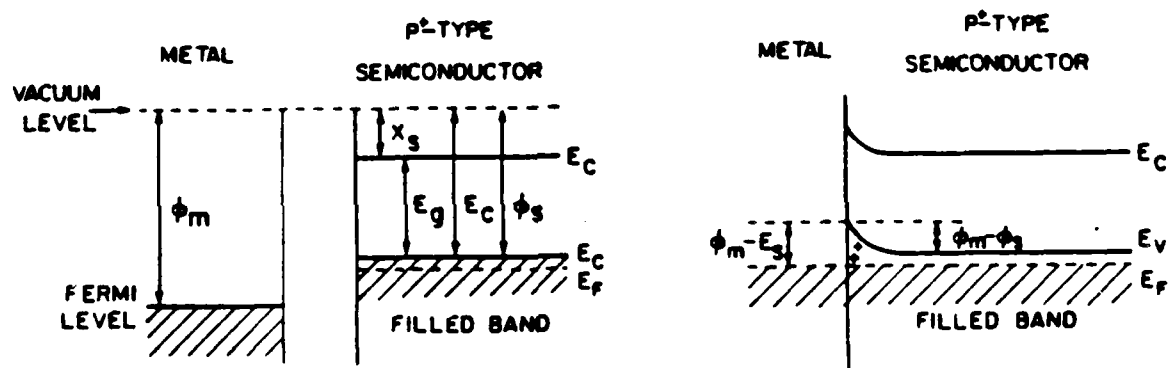
Figure B.4: Illustrastion of the formation of a p-ohmic contact at a metal-semiconductor interface.

shown in Fig. B.5, electrons flow from the metal to the semiconductor until equilibrium is established. When the Fermi levels line up at equilibrium, there is established a potential barrier for hole motion from the semiconductor to the metal of height $\phi_s - \phi_m$. This barrier can be lowered or raised by application of an appropriate voltage across the metal-semiconductor junction. Application of a negative voltage at the metal corresponds to positive potential at the semiconductor. This means that the barrier, $(\phi_s - \phi_m)$, to the flow of holes from the semiconductor is lowered to $(\phi_s - \phi_m - V_F)$ so that holes can flow easily from the semiconductor to the metal. A positive applied voltage at the metal, however, corresponds to a negative potential at the semiconductor. This raises the hole barrier at the semiconductor to $(\phi_s - \phi_m + V_R)$. With this barrier raised, very few holes, if any, can flow across the junction to the metal. Therefore depending on the polarity of the applied voltage, the metal-semiconductor contact acts as a diode (rectifier) allowing hole current to flow readily in only one direction and not in the other. The barrier to the flow of any holes from the metal to the semiconductor is fixed to the value of $E_s - \phi_m = E_g(x) + \chi_s - \phi_m$. We can make this value as large as we desire by varying the band gap of the (Al,Ga)As layer. It is therefore obvious now that for a positive voltage applied to the metal contact (as in the case of a forward biased laser diode), the metal-semiconductor contact at the Ti-(Al,Ga)As surface acts as a reverse-biased diode.

B.4.8   n-Contact Metallization

The n-contact metallization is done in a regular thermal evaporator. The major preparatory step before this evaporation involves lapping the wafer down from the backside to a thickness of about 4 mils ($\sim 100\mu$m). This step is necessary so that it is easy to cleave the wafer into individual dis-
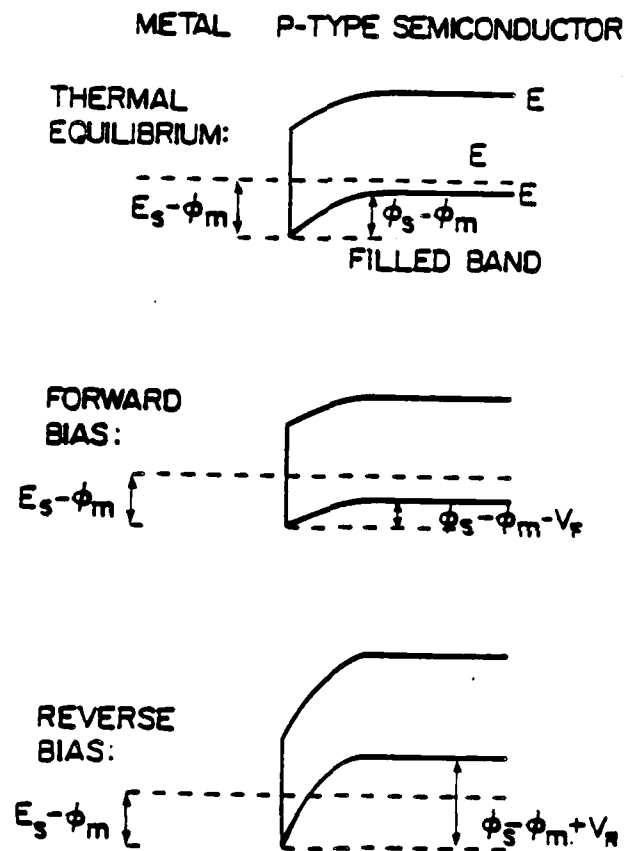
Figure B.5: The formation of a p-rectifying (Schottky) contact at a metal-semiconductor interface.

crete devices later. The lapping is performed on a lapping jig with Al_3O_2 (aluminum oxide) grit of varying sizes. Since the wafer is so thin at this point, *extreme care and patience* must be exercised in order not to break it.

When the wafer has been lapped down to the 4 mils, it is cleaned in deionized water, etched in bromo-methanol slightly, rinsed in methanol and iso-propyl alcohol and loaded into the evaporator immediately. After a pump down to base pressures better than 5×10^{-7} Torr, the following metals are deposited: first, 800 Å of Au-Ge then 120 Å of Ni and finally 1800 Å of Au. The Au-Ge increases the conductivity of the substrate; the Ni acts as an adhesive and the three layers together form a good n-type ohmic contact to the substrate.

Before further processing, the wafer is sintered to improve the ohmic contacts. The sintering is done in a furnace with a *forming* gas atmosphere where the wafer can be placed with n-side down on a carbon strip heater. The sample is sintered for 30-40 seconds at 400°C.

B.4.9   Laser Mirror Formation and Chip Separation

In order to make the laser facet mirrors, the wafer must first be mounted on a thin, stainless steel shim stock ($\sim$ 5 mils thick) with some wax. The shim stock (with the wafer on it) is then mounted, under a microscope, onto an apparatus (a home-made gizmo) that has X, Y and Z micro-positioners on it. The apparatus has a precison surgeon's blade affixed to it. Using the blade and the micro-positioners, a series of short scratches parallel to the <110> cleavage direction are made on the edge of the wafer. These scratches are spaced by $\sim$ 250 − 300 μm. They will form the cavity lengths of the lasers. The shim stock sheet is then bent around a cylindrical object, e.g. a beaker or a measuring cylinder. The scratches on the wafer should propagate along the [110] cleavage planes. These cleavage planes

form the mirror facets of the lasers. The $250 - 300$ μm wide laser bars must now be saw-cut or scribed into individual discrete devices. This is done by mounting the bars onto a silicon wafer with wax and then scribing (sawing) at 200-250 μm intervals. The laser devices are cleaved in one direction and scribed (sawed) along the other so that during operation, only one set of cavity modes is excited to lasing thresholds. This set is the longitudinal one which is a result of the electromagnetic waves traveling back and forth between the parallel mirrors. The transverse set is *suppressed* because there are no mirrors in this direction.

The individual laser devices can now be cleaned in warm trichloroethylene, acetone, methanol and iso-propyl alcohol. The last step in the fabrication process is the testing of the devices for the quality of their current-voltage (I-V) characteristics before mounting and bonding for optical characterization.

B.5   Mounting and Bonding

The individual laser devices must be tested for the quality of their current-voltage (I-V) characteristics before mounting onto the final device package. Only those devices that exhibit sharp forward turn-on and reverse break-down voltages are selected for mounting. The packages onto which the devices are mounted must be gold-plated. In our case they were made of OFC-grade copper plated with at least 5 μm of gold.

To mount the devices onto the package preform, we use a two component silver filled epoxy (manufactured by Epoxy Technology, Inc. in Billerica, MA). The epoxy is very *carefully* spread on an area no bigger than the surface area of the device to be mounted. The thickness of the epoxy should be less than 15 μm ($<$ 0.5 mil). This is necessary in order to avoid any

excess epoxy from creeping up to the device facets (mirrors). The whole process is carried out under a microscope (of course). Once the device is placed on the area where the epoxy is, the preform is carefully put on top of a hot plate at 150° C. The preform and the device are cured for 30 minutes.

At the end of the curing cycle, the device is ready for bonding. The bonding process is done on a standard microelectronic bonder. The special precautions that must be observed for lasers include: (1) making sure that the top device metallization has at least 3000 Å of gold, (2) the bonder is set for a minimum bonding pressure (otherwise one is likely to punch through to the active layer) and (3) as far as possible, to carry out the whole process patiently and slowly!

The packaged and bonded device must now be cleaned in detergent and deionized water in order to lift off any dirt from the facets. The I-V characteristics are re-checked to make sure they did not change. After this step, the device is ready for further optical characterization.

Bibliography

[1] D. E. Ackley, IEEE J. Quant. Electronic., **QE-18**, 1910 (1982).

[2] D. R. Scifres, W. Streifer and R. D. Burnham, IEEE J. Quant. Electronic., **QE-15**, 917 (1979).

[3] H. F. Lockwood, H. Kressel, H. S. Somers and F. Z. Hawrylo, Appl. Phys. Lett., **17**, 499 (1970).

[4] H. Kressel, H. F. Lockwood and F. Z. Hawrylo, J. Appl. Phys., **43**, 561 (1972).

[5] H. Kressel and J. K. Butler, *Semiconductor Lasers and Heterostructure LEDs.*, Academic Press, pp 455-464 (1977).

[6] J. Ripper and T. L. Paoli, Appl. Phys. Lett., **17**, 371 (1970).

[7] D. R. Scifres, W. Streifer and R. D. Burnham, Appl. Phys. Lett., **33**, 616 (1978).

[8] D. Botez and D. Ackley, IEEE Circuits and Devices Magazine, **2**, 8 (1986), and the References therein.

[9] L. L. Chang and K. Ploog (eds.), *Molecular Beam Epitaxy*, NATO Advanced Science Institute Series, M. Nijhoff Publishers, Dordrecht (1985).

[10] G. Dresselhaus, *Ph. D. Thesis*, University of California, Berkeley, CA., September, 1955.

[11] J. H. Luttinger and W. Kohn, Phys. Rev., **97**, 869 (1955).

[12] F. Bloch, Z. Physik, **52**, 555 (1928).

[13] J. E. Zucker, A. Pinczuk, D. S. Chemla, A. C. Gossard and W. Wiegmann, Phys. Rev., **B29**, 7065 (1984).

[14] R. Dingle, W. Wiegmann and C. H. Henry, Phys. Rev., **33**, 827 (1974).

[15] W. Jones and N. H. March, *Theoretical Solid State Physics, Vol. 1*, Wiley-Interscience, N. Y., p27 (1973).

[16] R. Loudon, *Quantum Theory of Light*, Claredon Press, Oxford, (1983).

[17] R. L. White, *Basic Quantum Mechanics*, McGraw-Hill, N.Y., p233 (1966).

[18] H. C. Casey and M. B. Panish, *Heterostructure Lasers*, Part A, Academic Press, N. Y. (1978).

[19] L. L. Chang, G. A. Sai-Halasz and L. Esaki, J. Vac. Sci. Technol., **19**, 589 (1981).

[20] D. A. B. Miller, D. Chemla, D. J. Eilenberger and P. Smith, Appl. Phys. Lett., **41**, 679 (1982).

[21] D. S. Chemla and D. A. B. Miller, J. Opt. Soc. Am. **B2**, 1155 (1985).

[22] D. S. Chemla, Physics Today, **38**, 965 (1981).

[23] C. Weisbuch, R. Dingle, A. C. Gossard and W. Wiegmann, J. Vac. Sci. Technol., **17**, 1128 (1980).

[24] N. Holonyak, W. D. Laidig and B. A Vojak, Phys. Rev. Lett., **45**, 1703 (1980).

[25] L. Goldstein, Y. Horikoshi, S. Tarucha and H. Okamoto, Jpn. J. Appl. Phys., **22**, 1489 (1983).

[26] J. Singh, K. Bajaj and S. Chaudhuri, Appl. Phys. Lett., **44**, 805 (1984).

[27] H. Iwamura, H, Kobayashi and H. Okamoto, Jpn. J. Appl. Phys., **23**, L795 (1984).

[28] D. Reynolds, K. K. Bajaj and C. W. Litton, Appl. Phys. Lett., **46**, 51 (1985).

[29] W. Masselink. P. Pearah, J. Klem, C. Peng and H. Morkoç, Phys. Rev., **B32**, 8027 (1985).

[30] T. Ohta, K. Kobayashi and H. Nakashima, Jpn. J. Appl. Phys., **25**, 59 (1986).

[31] M. Naganuma, J. Song and Y. Kim, J. Appl. Phys., **60**, 1740 (1986).

[32] R. F. Kazarinov and G. V. Tsarenkov, Soviet Physics, Semiconductors, **10**(2), 178 (1976).

[33] M. Yamada, S. Ogita, M. Yamagishi, K. Tabata and N. Nakaya, Appl. Phys. Lett., **45**, 324 (1984).

[34] R. Chin, N.Holonyak, B. A. Vojak, K. Hess, R. D. DuPuis and P. D. Dapkus, Appl. Phys. Lett., **36**, 19 (1980).

[35] N. Dutta, J. Appl. Phys. **53**, 7211 (1982).

[36] D. Kasamset, C. S. Hong, N. B. Patel and P. D. Dapkus, IEEE J. Quant. Electronic., **QE-19**, 1025 (1983).

[37] A. Sugimura, IEEE J. Quant. Electronic., **QE-20**, 336 (1984).

[38] H. C. Casey and F. Stern, J. Appl. Phys., **47**, 631 (1976).

[39] M. Asada, A. Kameyama and Y. Suematsu, IEEE J. Quant. Electronic., **QE-20**, 745 (1985).

[40] G. Dresselhaus, Ph. D. Thesis, University of California, Berkeley, CA, Sept. 1955.

[41] E. O. Kane, *Semiconductors and Semimetals*, edited by R. K. Willardson and A. C. Beer, **1**, 75 (1966).

[42] E. O. Kane, J. Phys. Chem. Solids, **1**, 249 (1957).

[43] H. Kobayashi, H. Iwamura, T. Saku and K. Otsuka, Electronics Lett., **19**, 166 (1983).

[44] G. Lasher and F. Stern, Phys. Rev., **133**, A553 (1964).

[45] M. G. A. Bernard and G. Duraffourg, Phys. Stat. Solidi, **1**, 699 (1961).

[46] S. D. Hersee, B. de Cremoux and J. P. Duchemin, Appl. Phys. Lett., **44**, 476 (1984).

[47] H. C. Casey and M. B. Panish, *Heterostructure Lasers*, Part A, p 182 Academic Press, N. Y. (1978).

[48] N. Dutta, R. L. Hartman and W. T. Tsang, IEEE J. Quant. Electronic., **QE-19**, 1243 (1983).

[49] W. T. Tsang and J. A. Ditzenberger, Appl. Phys. Lett., **39**, 193 (1981).

[50] S. Hersee, M. Baldy, P. Assenat, B. de Cremoux and J. P. Duchemin, Electronics Lett., **18**, 870 (1982).

[51] W. Heisenberg, *Physics and Beyond*, Harper and Row, 1972.

[52] P. G. Eliseev and N. N. Shuikin, Soviet J. Quant. Electronic., **3**, 181 (1973).

[53] M. Yamada and Y. Suematsu, J. Appl. Phys., **52**, 2653 (1981).

[54] Y. Nishimura and Y. Nishimura, IEEE J. Quant. Eletronic., **QE-9**, 1011 (1973).

[55] B. Zee, IEEE J. Quant. Electronic., **QE-14**, 727 (1978).

[56] M. Yamada, H. Ishiguro and H. Nagato, Japan J. Appl. Phys., **19**, 135 (1980).

[57] W. T. Tsang, Appl. Phys. Lett., **39**, 786 (1981).

[58] S. Yamakoshi, T. Sanada, O. Wada, T. Fujii and T. Sakurai, Proc. 4th Int. Conf. Integrated Optics & Opt. Fiber Comm., Paper 27B3-1, June, 1983, Tokyo, Japan.

[59] H. Kogelnik and V. Ramaswamy, Appl. Optics, **13**, 1857 (1974).

[60] A. Yariv, IEEE J. Quant. Electron., **QE-9**, 919 (1974).

[61] D. R. Scifres, W. Streifer and R. Burnham, IEEE J. Quant. Electron., **QE-15**, 917 (1979).

[62] D. E. Ackley, IEEE J. Quant. Electron., **QE-18**, 1910 (1982).

[63] D. E. Ackley, Appl. Phys. Lett., **42**, 152 (1983).

[64] D. R. Scifres, W. Streifer, R. D. Burnham, T. L . Paoli and C. Lindström, Appl. Phys. Lett., **42**, 495 (1983).

[65] J. Katz, E. Kapon, C. Lindsey, S. Margalit and A. Yariv, Elect. Lett , **19** 660 (1983).

[66] J. E. Epler, N. Holonyak, R. D. Burnham, T. L. Paoli and W. Streifer, Appl. Phys. Lett., **57**, 1489 (1985).

[67] H. Temkin, R. A. Logan, J. P. van der Ziel, C. L. Reynolds and S. M. Tharaldsen, Appl. Phys. Lett., **46**, 465 (1985).

[68] E. Kapon, L. T. Lu, Z. Rav-Noy, M. Yi, S. Margalit and A. Yariv, Appl. Phys. Lett., **46**, 136 (1985).

[69] E. Kapon, Z. Rav-Noy, T. Lu, M. Yi, S. Margalit and A. Yariv, Appl. Phys. Lett., **45**, 1159 (1984).

[70] D. E. Ackley and R. W. H. Engelman, Appl. Phys. Lett., **39**, 27 (1981).

[71] D. R. Scifres, R. D. Burnham and W. Streifer, Appl. Phys. Lett. **41**, 118 (1982).

[72] J. P. van der Ziel, R. Mikulyak, H. Temkin, R. Logan and R. D. Dupuis, IEEE J. Quant. Electron., **QE-20**, 1259 (1984).

[73] D. Botez and J. C. Conolly, 41st Annual Device Research Conf., Univ. Vermont, Vt., Paper IVB-1, June 20-22 (1983) .

[74] Y. Twu, A. Diens S. Wang, J. R. Whinnery, Appl. Phys. Lett., **45**, 709 (1984).

[75] D. F. Welch, D. Scifres, P. Cross and H. Kung, Appl. Phys. Lett., **47**, 1134 (1985).

[76] J. Katz, S. Margalit and A. Yariv, Appl. Phys. Lett., **42** 554 (1983).

[77] S. Wang, J. Z. Wilcox, M. Jansen and J. Yang, Appl. Phys. Lett., **48**, 1770 (1986).

[78] D. R. Scifres, W. Streifer and R. D. Burnham, Appl. Phys. Lett., **33**, 616 (1978).

[79] D. F. Welch, P. S. Cross, D. R. Scifres, W. Streifer and R. D. Burnham, 44th Annual Device Research Conf., UMass, Amherst, Ma., Paper VA-2, June 23-25 (1986).

[80] D. D. Cook and F. R. Nash, Journ. Appl. Phys., **46**, 1660 (1975).

[81] L. I. Schiff, *Quantum Mechanics*, McGraw-Hill, (1968).

[82] G. D. Boyd and H. Kogelnik, Bell sys. Tech. J., **41** 1347 (1962).

[83] H. Kogelnik, Appl. Opt., **4**, 1562 (1965).

[84] H. Kogelnik and T. Li, Appl. Opt., **5**, 1550 (1966).

[85] S. M. Sze and G. Gibbons, Appl. Phys. Lett., **8**, 111 (1966).

[86] W. T. Tsang, Appl. Phys. Lett., **40**, 217 (1982).

[87] S. D. Hersee, M. Baldy, P. Assenat, B. de Cremoux and J. P. Duchemin, Electron. Lett., **18**, 870 (1982).

[88] D. Kasamset, C. S. Hong, N. B. Patel and P. D. Dapkus, Appl. Phys. Lett., **41**, 912 (1982).

[89] T. Fujii, S. Yamakoshi, K. Nambu, O. Wada and S. Hiyamizu, J. Vac Sci. and Technol., **2**, 259 (1984).

[90] G. Cheroff, F. Stern and S. Triebwasser, Appl. Phys. Lett., **2**, 173 (1963).

[91] J. R. Biard, W. N. Carr and B. S. Reed, Trans. AIME **230**, 286 (1964).

[92] H. C. Casey and M. B. Panish, *Heterostructure Lasers:* Part A, Academic Press, (1978).

[93] A. Yariv, *Introduction to Optical Electronics*, 1976, Chapter 6.

[94] T. L. Paoli, IEEE J. Quantum Electron., **QE-12**, 770 (1976).

[95] R. Lang, IEEE J. Quantum Electron., **QE-15**, 718 (1979).

[96] K. Kobayashi, R. Lang, H. Yonezu, Y. Matsumoto, T. Shinohara, I. Sakuma, T. Suzuki and I. Hayashi, IEEE J. Quantum Electron., **QE-13**, 659 (1977).

[97] P. M. Asbeck, D. A. Cammack and J. J. Daniele, Appl. Phys. Lett., **33**, 504 (1978).

[98] D. T. F. Marple, J. Appl. Phys., **35**, 1241 (1964).

[99] B. W. Hakki and T. L. Paoli, J. Appl. Phys., **44**, 4113 (1973).

[100] B. W. Hakki and T. L. Paoli, J. Appl. Phys., **46**, 1299 (1975).

[101] D. F. Welch, D. Scifres, P. Cross and H. Kung, Appl. Phys. Lett., **47**, 1134 (1985).

[102] H. C. Casey, S. Somekh and M. Ilegems, Appl. Phys. Lett., **27**, 142 (1975).

[103] K. Aiki, M. Nakamura and J. Umeda, Appl. Phys. Lett., **27**, 145 (1975).

[104] W. T. Tsang, N. A. Olsson and R. A. Logan, Appl. Phys. Lett., **42**, 650 (1983).

[105] M. Born and E. Wolf, *Principles of Optics*, 1984, Chapter 8.

[106] D. Botez and D. E. Ackley, IEEE Circuits and Devices Magazine, **2**, 8 (1986).

[107] J. K. Butler, D. E. Ackley and D. Botez, Appl. Phys. Lett., **44**, 293 (1984).

[108] E. Kapon. J. Katz and A. Yariv, Optics Lett., **10**, 125 (1984).

[109] C. L. and J. W. Liu, *Linear Systems Analysis*. McGraw-Hill, Inc., N. Y. (1975).

[110] A. Papoulis, *Systems and Transforms with Applications in Optics*, McGraw-Hill, Inc., N. Y. (1968).

[111] D. D. Cook and F. R. Nash, J. Appl. Phys., **46**, 1660 (1975).

[112] M. Born and E. Wolf, *Principles of Optics*. 6th Edition, Pergamon Press, N. Y. pg 380 (1980).

[113] S. Silver, *Microwave Antenna Theory and Design*, McGraw-Hill, Inc., N. Y. Chap. 6 and 9 (1949).

[114] G. E. Fenner and J. D. Kingsley, J. Appl. Phys., *34*, 3204 (1963).

[115] A. Y. Cho, Progress in Solid State Chem.,**10**, 157, (1975).

[116] L. L. Chang and K. Ploog (eds.),*Molecular Beam Epitaxy*, NATO Advanced Science Institute Series, M. Nijhoff Publishers, Dordrecht (1985).

[117] J. R. Arthur, J. Appl. Phys., **39**, 4032 (1968).

[118] M. Knudsen, Ann. Physik, **48**, 113 (1915).

[119] B. B. Dayton, 1956 Vacuum Symposium Transactions, Committe on Vacuum Techniques, Boston, 5, (1956).

[120] R. E. Honig and D. A. Kramer, RCA Review, **30**, 285 (1969).

[121] H. Shelton and A. Y. Cho, J. Appl. Phys., **37**, 3544 (1966).

[122] A. Y. Cho and C. D. Hendricks, J. Appl. Phys., **40**, 3339 (1969).

[123] A. Y. Cho, J. Appl. Phys., **41**, (1970).

[124] J. J. Harris, B. A. Joyce and P. J. Dobson, Surf. Sci., **103**, L.90 (1981).

[125] C. E. C. Wood, Surf. Sci., **108**, L.441 (1981).

[126] J. H. Neave, B. A. Joyce, P. J. Dobson and N. Norton, Appl. Phys. **A31**, 1 (1983).

[127] A. Y. Cho, Thin Solid Films, **100**, 291 (1983).

[128] C. T. Foxon, B. A. Joyce, Surf. Sci. **64**, 293 (1977).

[129] H. Kunzel and K. Ploog, Appl. Phys. Lett. **37**, 416 (1980).

[130] A. R. Calawa, Appl. Phys. Lett., **33**, 1022 (1978)
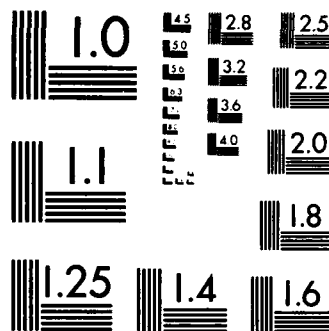
MICROCOPY RESOLUTION TEST CHART

NATIONAL BUREAU OF STANDARDS-1963-A

[131] J. L. Lievin and F. Alexandre, Elec. Lett., **21**, 413 (1985).

[132] A. K. Sinha, T. E. Smith and T. T. Sheng, Thin Solid Films, **22**, 1 (1974).

[133] A. T. English, K. L. Tai and P. A. Turner, J. Appl. Phys., **45**, 3757 (1974).

[134] S. M. Sze, *Physics of Semiconductor Devices*, John Wiley and Sons, N. Y. 363 (1969).

[135] B. L. Sharma, *Semiconductors and Semimetals*, R. K. Willardson and A. C. Beer (eds.), Academic Press, Vol **15**, 15 (1981).

[136] Y. Twu, A. Dienes, S. Wang and J. R. Whinnery, Appl. Phys. Lett., **45**, 709 (1984).

[137] D. Welch, D. Scifres, P. Cross, H. Kung, Appl. Phys. Lett., **47**, 1134 (1985).

END

12 - 87

DTIC